SUPERCONDUCTING, STRUCTURAL, AND MAGNETIC PROPERTIES OF LITHIUM AND LITHIUM-RICH COMPOUNDS

by

Anne Marie Schaeffer Richards

A dissertation submitted to the faculty of
The University of Utah
in partial fulfillment of the requirements for the degree of

Doctor of Philosophy

in

Physics

Department of Physics and Astronomy

The University of Utah

May 2016

The University of Utah Graduate School

STATEMENT OF DISSERTATION APPROVAL

The dissertation of **Anne Marie Schaeffer Richards**

has been approved by the following supervisory committee members:

Stephan LeBohec	, Chair	**11/24/2015** Date Approved
Jordan Gerton	, Member	**11/24/2015** Date Approved
Eugene Mishchenko	, Member	**11/24/2015** Date Approved
Lowell Miyagi	, Member	**11/24/2015** Date Approved
Clayton Williams	, Member	**11/24/2015** Date Approved

and by **Carleton DeTar** , Chair/Dean of

the Department/College/School of **Physics and Astronomy**

and by David B. Kieda, Dean of The Graduate School.

ABSTRACT

Lithium is generally considered to be a simple metal, given its simple electronic structure with one valence electron. It is considered to follow a nearly free electron model and have a nearly spherical Fermi surface. However, away from ambient conditions, the behavior of lithium becomes much less simple. Under high pressures, lithium undergoes a series of symmetry breaking phase transitions, even a metal to insulator transition; at low temperatures, lithium also undergoes a temperature-driven martensitic transformation. In this work, these deviations from simple models in lithium are investigated, both at ambient pressure and under high pressures, from the relative high temperature phenomenon of melting, to low temperature measurements of superconductivity.

CONTENTS

LIST OF FIGURES

LIST OF TABLES

ACKNOWLEDGMENTS

I would like to acknowledge the mentorship of Professor Shanti Deemyad. All experimental skills and scientific expertise were learned under the guidance of Professor Deemyad. All of the experiments presented in this dissertation were either carried out in the Deemyad Lab at the University of Utah or at User Facilities with access granted as a result of Professor Deemyad's approved research proposals.

This dissertation would not have been possible without the help from Professors LeBohec and Mischenko in allowing my defense to go forward. Also, the support from Vice President of Faculty Amy Wildermuth and Dean of Students Lori McDonald were instrumental to the presentation of this work.

Professor Raikh provided insightful feedback regarding this work as well as the presentation of the thesis defense.

Also, this work benefited as a result of the help and support from the Physics and Astronomy GSAC.

Chapter 3: The authors would like to acknowledge the generous donation of some of the major equipment used in this study by Linda and Robert Grow from UPRI Co. The authors would like to thank Dr. Eugene Mishchenko for insightful discussions on the topic of melting and reviewing this manuscript, Matthew DeLong for providing technical and intellectual support in design of the experiment, and the University of Utah UROP fund for partial financial support.

Chapter 5: Authors are grateful for experimental assistance from R. McLaughlin, D. Sun, H. Malissa, Z. Jiang, F. Doval, and A. Friedman. This work is supported by NSF-DMR grant num. 1351986. JKB acknowledges the financial support from the University of Utah UROP fund.

Chapter 8: The authors thank Dr. Richard Hennig for insightful discussions on electronic properties of $BaLi_4$. Experimental support by S.R. Temple, J. Jue, Z. Xu, and J. Bishop in sample preparation and low temperature studies and analysis of XRD spectrum by M. Sygnatowicz in Materials Characterizations Lab of University of Utah, Material Science Department is acknowledged. One of the authors, W. Talmadge, would like to acknowledge

the financial support from University of Utah UROP program. Initial sample synthesis was done with great help from the late W. Wingert.

CHAPTER 1

INTRODUCTION

This work is mainly concerned with the properties of low Z materials under extreme conditions, in particular, lithium and lithium-rich materials. This dissertation serves to give some theoretical background of alkali metals, lithium in particular, and to describe experimental studies.

There are three main parts: an introduction and overview of the experimental techniques used, Chapters 1 and 2; results and/or discussions of experimental work, Chapters 3 through 8; and a summary of findings, Chapter 9.

1.1 Alkali Metals

The alkali metals are characterized by one valence electron (s-electron) and tightly bound core electrons. Intuitively, this simple electronic structure should lead to simple behaviour. Indeed, under ambient conditions, the alkali metals behave in manners described well by the nearly free electron model. However, with the application of high pressures, the alkali metals display nonintuitive trends: lithium, sodium, potassium, and rubidium all display maximums and subsequent minimums [65, 70, 100, 110, 155, 130] in their melting curves as a function of pressure (the measured melting temperatures at differing pressures), as well as a series of symmetry-breaking structural phase transitions, going from the highly symmetric bcc to much lower symmetry phases [132, 75, 65, 130, 4]. Lithium and sodium also undergo a martensitic phase transformation at low temperature from bcc to hR3 at ambient pressure [13]. Lithium is the lightest of the alkalis that is a metal under ambient conditions. Though hydrogen has the same electronic configuration of the other elements in the alkali group, it is yet to be confirmed as metallic in laboratory conditions [189, 109, 129, 49]. However, the emergence of a metallic phase (even a nearly room temperature superconducting phase) is predicted to occur under extreme pressures [190, 5, 18, 115] and the strong magnetic field of Jupiter indicates that hydrogen is conductive at least within the core ($\sim$ 40 million

atmospheres). Due to the difficulty in reaching metallization pressures of hydrogen, the would-be lightest alkali metal, this work is focused on the next lightest alkali, lithium.

1.2 Lithium

Lithium is not only the lightest metal under ambient conditions, but it is also the lightest known superconductor [177, 42, 160, 172]. While under ambient pressure, the superconducting critical temperature (T_c) is rather low at ≈ 100 μK, with the application of extreme pressure, T_c increases to above 3.5 K near 15 GPa, and then begins to increase sharply at about 20 GPa, reaching a maximum near 30 GPa [42, 160, 172, 152]. This trend in the superconductivity of lithium is most likely related to the series of structural phase transitions that it undergoes as a function of pressure [70, 75]. Lithium has also been predicted and observed to undergo a metal to insulator transition (near 75 GPa) [119, 132].

1.3 Quantum Solids

A quantum solid is a material that is dominated by zero point energy ($\epsilon = \frac{1}{2}\hbar\omega$) and is intrinsically restless. A visualization of a quantum solid would be to imagine a solid with lattice spacing r. The lattice ions form a periodic structure, they are confined by fixed boundaries. If these lattice ions have a wave function with the width of the de Broglie wavelength, $\lambda = \frac{\hbar}{\sqrt{2m\epsilon}}$, comparable to r, $\lambda \gtrsim 0.1r$, corrections to the energy due to quantum mechanic effects must be considered. Since the thermal de Broglie wavelength, $\lambda = \frac{\hbar}{\sqrt{2mk_BT}}$, is inversely proportional to temperature, T, lowering the temperature appears to increase the width of the de Broglie wavelength. Thus at low temperatures, we may expect the wavefunctions of the lattice ions to spread in this manner, leading to significant ground state or zero point motion in the solid.

A useful parameter to qualify the extent of dominance of quantum effects on a system is the de Boer parameter (Λ). The de Boer parameter is the ratio of the de Broglie wavelength and the minimum distance separating atoms in a crystal, $\Lambda = \frac{\lambda}{r_{min}} = \frac{\hbar}{r_{min}\sqrt{2m\epsilon}}$. The de Boer parameter shows the amount of delocalization of a system compared to its size [43]. The higher the de Boer parameter, the higher the 'quantumness' of the system. This appears very similar to the Lindemann criterion of melting, discussed in section 1.5. Writing the de Boer parameter in terms of the potential energy $\frac{1}{r^i}$ yields:

$$\Lambda = \frac{\hbar r^{\frac{i}{2}-1}}{\sqrt{2m}} \tag{1.1}$$

which is very reminiscent of the criterion for quantum melting, further explored in section 1.5.1.

An example of such a material is ^{4}He, which does not even solidify under ambient pressure [113, 197]. Other low Z elements, such as lithium, may display quantum solid behaviour. There is even a small but measurable difference in the lattice constants of lithium isotopes, showing that the lattice constant of the ^{6}Li, the lowest mass isotope, is larger than that of natural lithium ($\sim$ 92 % ^{7}Li), indicating an expanded lattice for the lower mass isotope [35]. Lithium is an intriguing candidate for quantum solidity. Unlike solid ^{3}He, H_2 or D_2, which would be characterized by van der Waals interactions, $\propto \frac{1}{r^6}$, a quantum solid lithium (at least at pressures $<\sim$70 GPa) would be in a metallic phase. Whilst insulators form interatomic bonds characterised by a short-range potential, $\propto \frac{1}{r^6}$, metals are characterised by long-range Coulomb interactions, $\propto \frac{1}{r}$. (The full term for Coulomb potential is $V(r) = \frac{e^2}{r}e^{-k_D r}$, with $e^{-k_D r}$, k_D is the inverse of the Debye length, describing Debye electron screening. This term shows that the electric field of the positively charged ions in an electron gas diminishes more rapidly than $\frac{1}{r}$ as the electron gas tends to gather around the positive charge. As the main difference between metals and insulators in this work is concerned with the comparative range of the potentials, Coulomb potential is estimated to be $\propto \frac{1}{r}$ as in [170].) This type of metallic quantum solid opens the possibility of a material that could exhibit an increase in quantum solid characteristics, and even perhaps quantum melting, with the application of pressure [170](see section 1.5.1 and Chapter 3).

1.3.1 Nearly Free Electron Model

The alkali metals are generally considered to be simple metals, following a nearly free electron model. According to this model, the conduction electrons are considered to be free in the lattice. The conduction electrons in a periodic potential behave as unbound electrons. This is described by the Bloch Theorem, in which the wave function of the free electron experiences periodic potential wells determined by the lattice:

$$\psi_k(r) = e^{ik\cdot r} \longrightarrow \psi_k(r) = e^{ik\cdot r}u_k(r) \tag{1.2}$$

where $u_k(r)$ is a function with the periodicity of the crystal lattice.

In this model, the lattice is assumed to be static. It is assumed that the energy contribution of the motion of lattice ions does not significantly contribute to the overall energy of the system. This means that this model could only be valid at zero temperature, given the always present motion of the lattice ions from thermal energy, $\propto k_B T$. However, considering a solid even at zero temperature, there is still the contribution from zero-point energy. In the case of a quantum solid, the zero-point energy dominates the total energy of the system.

1.4 Extreme Conditions

Ambient conditions are quite unusual when considering the universe as a whole. Complex life on the surface on the earth exists in a remarkably narrow range of pressures and temperatures. Even when considering 'extremophiles', the range of the pressures and temperatures, $\sim 2\times10^4$ Pa ($\sim$ 0.2 bar) to $\sim 10^8$ Pa ($\sim$1000 bar) and $\sim$ 250 K to $\sim$ 400 K; whereas elsewhere in the universe, pressure and temperature range from vacuum $\sim 10^{-17}$ Pa to $\sim 10^{34}$ Pa inside a neutron star, and temperatures from 3 K to 10^{12} K. What we may think of as extreme, in many ways, can be the more typical state of a material. Though extreme conditions are difficult and generally expensive to achieve, it is important to explore such extreme conditions in a laboratory setting. Only viewing a material in our narrow range of ambient conditions does not allow sufficient range on any thermodynamic axis to properly gauge the behaviour of that material. Studying materials in extreme conditions allows for further characterization of said material, and for more accurate predications of its behaviour.

1.4.1 Pressure

Pressure is the thermodynamic variable with the largest range in the universe. Even in laboratory conditions, the range of achievable pressures is impressive, from $\sim 10^{-7}$ Pa ($\sim 10^{-12}$ bar) in a vacuum to $\sim 7\times\ 10^{11}\ Pa$ or $\sim$ 700 GPa ($\sim 7\times\ 10^6$ bar) static pressure and $>10^{12}$ Pa or 1 TPa (10^7 bar) dynamic pressure. This makes pressure one of the most important accessible thermodynamic variables and invaluable for the characterization of materials. In this work, only static pressure techniques were applied. Static pressure generally consists of two types, hydrostatic and nonhydrostatic. Hydrostatic pressures are achieved by using a liquid pressure transmitting medium, allowing the pressure to be isotropic across the sample, transmitted equally from all directions. In practice however, all pressure transmitting media solidify under sufficient pressure. Materials become stiffer as they are compressed, and different materials have varying hydrostatic limits under pressure (the pressures at which they become solid) [92, 3]. Hydrostatic and nonhydrostatic pressures may be applied in several types of pressure cells. In this work, pressure was applied in a Diamond Anvil Cell (DAC) or Paris-Edinburgh (PE) Press (see Chapter 2, sections 2.1.1 and 2.1.2). In the present work, generally either a solid pressure medium or no pressure medium was used (liquid argon was used in the visual observations detailed in Chapter 3; however, such hydrostatic measurements in this work are the minority).

1.4.2 Temperature

A wide range of temperatures is accessible under laboratory conditions and even inside a DAC. High power lasers can be focused through the diamond onto the sample or even a portion of the sample, and temperatures >1000 K can be achieved. Conversely, a DAC can be made to fit inside a cryostat or dilution refrigerator and <100 mK temperatures can be reached. For the characterization of materials, temperature, like pressure, is a very useful thermodynamic variable. Temperature governs many important aspects of a given material; the superconducting T_c, the melting temperature, T_m, and in the case of lithium, there is the temperature-driven martensitic transition at $M_s \approx 80$ K at ambient pressure [14, 13, 167, 151]. Used together, simultaneously, temperature and pressure allow one to map many interesting regions of the phase diagram: the superconducting phase diagram, the structural phase diagram, and melting curve to list a few.

1.5 High Pressure Melting

Melting is the transition of a material from a solid phase to a liquid phase as a function of either temperature or pressure. A useful concept for melting is the Lindemann Criterion, in which melting is described as the vibrational motion of the lattice ions exceeding a certain proportion of the lattice spacing (≈ 10 %) [106]. If we consider a solid with a lattice with an interatomic distance of r, the rms (root mean squared) amplitude of atomic vibration, $\langle dr_{rms}^2 \rangle^{\frac{1}{2}}$, and a constant fraction, δ, (generally assumed to be ≈ 0.1), the melting according to the Lindemann Criterion occurs when:

$$\frac{\langle dr_{rms}^2 \rangle^{\frac{1}{2}}}{r} = \delta \tag{1.3}$$

This criterion was inspired by the observation of the relation between the thermal expansion coefficient, α, and melting temperature, T_m:

$$\alpha T_m = \varepsilon \tag{1.4}$$

in which ε is a constant. Intuitively, if we imagine the application of pressure as decreasing the interatomic spacing, r, then $\langle dr_{rms}^2 \rangle^{\frac{1}{2}}$ must decrease proportionally in order to preserve the ratio. However, the interaction potential of the lattice ions also depends upon the interatomic distance r. In the case of a van der Waals type solid, the interaction potential is $\propto \frac{1}{r^6}$, so when r is reduced with the application of pressure, the potential energy increases, resulting in more energy required to affect $\langle dr_{rms}^2 \rangle^{\frac{1}{2}}$. In short, as the interatomic spacing decreases, the amount of energy necessary to displace the lattice ions through vibrations increases. This results in an increase of T_m as a function of pressure. This is true even

in the case of metals, in which the interaction potential is of the form $\propto \frac{1}{r}$. The intuitive expectation is that materials become more classical with the application of high pressure.

A thermodynamics approach to melting allows us to see effects of pressure upon the melting temperatures (T_m) of materials (in terms of classical mechanics). Starting with the relation of T_m and pressure (P) from the Clausius-Clayperon relationship [32] which appears in many standard thermodynamic textbooks:

$$\frac{1}{T_m}\frac{dT_m}{dP} = \frac{\Delta V}{L} \tag{1.5}$$

where ΔV is the change in volume and L is latent heat of melting, both are in terms of unit mass. However, from [69, 169] it appears that the entropy of melting, the change in disorder from the first-order phase transition:

$$\Delta S = \frac{L}{T_m} \tag{1.6}$$

is independent of pressure. We can introduce the Grüneisen parameter,

$$\gamma = \frac{\alpha K}{\rho C_v} \tag{1.7}$$

in which α is the thermal expansion coefficient, K is the bulk modulus, either isothermal or adiabatic depending upon the path, ρ is density, and C_v is the specific heat at constant volume. We can insert the Grüneisen parameter into the Clauius-Clayperon relation [168]:

$$\begin{aligned}
&\gamma = \frac{\alpha K}{\rho C_v} \\
&\left(\frac{\partial P}{\partial T}\right)_V = \alpha K = \gamma \rho C_V \\
&dP = \int dT \gamma \rho C_v \approx \gamma \rho \left(\frac{\Delta E}{m}\right) \\
&\frac{\Delta E}{m} = 2L \longrightarrow dP = 2\gamma \rho C_v \\
&dP = K\left(\frac{\Delta V}{V}\right) \rightarrow dP = K \Delta V \rho \dashrightarrow \text{for unit cell volume change} \\
&\frac{1}{T_m}\frac{dT_m}{dP} = \frac{\Delta V}{L} = \frac{2\gamma}{K}
\end{aligned} \tag{1.8}$$

Here, we can see that the slope of the melting curve as a function of pressure is inversely proportional to the incompressibility (bulk modulus K), showing that the expectation is that the slope $\frac{T_m}{dP}$ is positive as the material is compressed.

However, this relation is based upon the assumption that the material does not undergo any reordering as it is compressed, that there are no pressure induced structural phase transitions. In section 1.1, it is noted that the alkali metals, lithium, sodium, potassium,

and rubidium all have a maximum in their melting curves. This type of anomalous melting curve [169], occurs when the liquid phase is more dense than the solid phase. Since these materials do show symmetry-breaking phase transitions with the application of pressure, the maxima in the melting curves can be understood as a classical effect, and it is expected that if the material is compressed to a sufficiently close-packed structure, the equation 1.8 will be valid [168]. If a material undergoes a phase transition to a structure with relatively low symmetry, then it is possible for a liquid to be more efficiently packed than a solid. At a constant temperature, the result is a pressure-induced melting transition; meaning the slope of $\frac{dT_m}{dP}$ becomes negative, leading to a maximum in the melting curve as a function of pressure. Chapter 3 explores the melting curve of lithium under high pressures in more detail and results of experiment are presented therein.

1.5.1 Quantum Melting

Although it is understood that the maxima (and even subsequent minima) in the melting curves of the alkali metals correspond to the series of symmetry-breaking phase transitions in these materials, i.e., there is a classical explanation; the concept of quantum melting is an intriguing possibility for low Z metals, such as lithium (or even possibly dense hydrogen). This is the possibility that purely quantum effects can serve to expand the lattice even as pressure is applied to compress it [170]. We start with restating the Lindemann criterion 1.9:

$$\frac{\langle dr_{rms}^2 \rangle^{\frac{1}{2}}}{r} = \delta \tag{1.9}$$

If we rewrite the Heisenberg uncertainty principle:

$$\begin{aligned} &\Delta r \Delta p \geq \hbar \\ &p = \sqrt{2m\epsilon} \\ &\epsilon \propto \frac{1}{r^n} \\ &\Delta r = \langle dr_{rms}^2 \rangle^{\frac{1}{2}} \end{aligned} \tag{1.10}$$

resulting in the relation:

$$\Delta r \Delta p \geq \hbar \longrightarrow \langle dr_{rms}^2 \rangle^{\frac{1}{2}} \left(\frac{1}{r^n}\right)^{\frac{1}{2}} \propto constant \tag{1.11}$$

This comes from replacing the momentum term p in the uncertainty principle with energy, and equating that energy with the potential in the lattice (since it is at equilibrium). Finally

for simplicity, we use a proportionality to a constant. We can then rearrange this into the familiar format of equation 1.9:

$$\frac{\langle dr_{rms}^2 \rangle^{\frac{1}{2}}}{r} \propto r^{\frac{n}{2}-1} \tag{1.12}$$

From this equation (1.12), we can see that if $n = 1$, as is the case for a metal with Coulomb type interactions ($\frac{1}{r}$), as the interatomic distance r decreases, the fraction $\frac{\langle dr_{rms}^2 \rangle^{\frac{1}{2}}}{r}$ increases. Meaning the δ in equation 1.9 increases, possibly to a value over the critical fraction to cause the lattice to melt.

Whilst the results presented in Chapter 3 do not provide sufficient evidence to conclude that the minimum in the melting curve of lithium is due to quantum melting, it remains an open question to investigate whether the phenomenon may occur at higher densities.

1.6 Superconductivity

Superconductivity as a physical phenomenon is important to this body of work, as it is a low temperature phase transition as well as a quantum mechanical effect. When searching for the possibilities of quantum solid behaviour in metallic, dense lithium, studies of the behaviour of the superconducting phase as a function pressure may provide insights into the physics governing this material. This is one of the main motivations for the investigation into the superconducting phase of dense lithium and its isotope effects (see Chapter 5 for experimental results). Superconductivity was first reported in mercury in 1911 by H.K. Onnes [136]. It was first thought that the electrical resistivity of a metal would decrease as a function of temperature continuously down to zero temperature. However, Onnes' laboratory measured the resistivity of mercury as a function of temperature down to liquid helium temperatures, and they observed an abrupt drop in the resistivity near 4.2 K. Soon after, it was found that not only was there a critical temperature (T_c), above which superconductivity could not exist, but there was also a relatively weak critical magnetic field (H_{cm}) that could also destroy the superconducting state. The T_c and H_{cm} of conventional BCS or type I superconductors can be described by the empirical formula [157]:

$$H_{cm}(T) = H_{cm}(0)\left[1 - \left(\frac{T}{T_c}\right)^2\right] \tag{1.13}$$

After the initial report, many other metals were found to demonstrate the same abrupt drop in electrical resistivity. This was assumed to be ideal conductance ($\rho = 0$) for ~ 22 years. In 1933, Meissner and Ochsenfeld reported that materials in the superconducting state also demonstrated zero internal magnetic field regardless of the material's history [124], known now as the Meissner-Ochsenfeld effect. This showed that superconductivity

was not simply ideal conductance, but rather a phase transition (characterized by electrical resistivity $\rho = 0$ and magnetic field $B = 0$), allowing for a thermodynamic approach to the study of the superconducting phase. After 1935, superconductivity was also described quite well in terms of electrodynamics by the London theory [108]. This approach treated a superconductor as having 2 types of electrons, superconducting and nonsuperconducting. However, a description of the behaviour of the superconducting electrons themselves was lacking (both in London theory and in the later Ginzburg-Landau theory [97]).

It was not until 1957 that a microscopic theory of the phenomenon had been proposed by Bardeen, Cooper, and Schrieffer (BCS theory) [9]. A key feature of the BCS theory comes from the idea of bound pairs of electrons from [34]. One starts by considering a normal metal in the ground state. In momentum space (or k space) all the states for the noninteracting electrons are occupied inside the Fermi Sphere (see section 1.8), and the states outside the Fermi sphere are not occupied. If an extra pair of electrons with equal momentum but with opposite sign, one spin up ($+k \uparrow$) and one spin down ($-k \downarrow$) are introduced near to the Fermi surface, these electrons become attracted to each other by means of phonon interaction. One electron deforms the lattice, which in turn affects the other electron, allowing them to form a pair even though they repel each other. One consequence of this type of phonon-mediated BCS type superconductivity is that there exists an isotope effect for T_c. The lighter isotope of a given superconducting element (either in elemental form or as a part of a compound) has a well-described shift to a higher T_c (see equation 1.14). The mass of the lattice ions alone has a distinct and predictable effect on the T_c. This is strong evidence for the effect of phonons on superconductivity. The two attracted electrons become bound as a Cooper Pair, the total spin of the paired electrons is zero, meaning they now no longer obey Fermi Statistics and now obey Bose-Einstein Statistics. Now, at $T<T_c$, the Cooper Pairs are all able to exist in the lowest energy level, as in Bose-Einstein condensation. In the Bose-Einstein condensate, all the particles have the same wave-function and are in a superfluid state. This makes it impossible for particles to be scattered separately by impurities or defects in the lattice from the remainder of the condensate without destroying the superconducting state itself. The energy it would take to scatter the particles separately would have to exceed the energy needed to break the Cooper pairs, thus destroying the supconducting state. According to BCS theory, the T_c can be expressed as:

$$T_c = 1.14 \left(\frac{\hbar \omega_D}{k_B} \right) e^{\frac{-1}{N(E_F) V_{eff}}} \tag{1.14}$$

in which ω_D is the Debye frequency, ($\omega_D = \sqrt{\frac{k}{m}}$), $N(E_F)$ is the density of states at the

Fermi level, and V_{eff} is the attractive potential between electrons [121]. From this equation 1.14, the isotope effect is apparent:

$$T_c = 1.14\left(\frac{\hbar k}{mk_B}\right)e^{\frac{-1}{N(E_F)V_{eff}}}$$
$$T_c \propto m^{-\alpha}, \alpha = \frac{1}{2} \tag{1.15}$$

Lighter isotopes are expected to show a proportionally higher $T_c's$ than the heavier isotopes ($light_c^T = \sqrt{\frac{M_{heavy}}{M_{light}}} heavy_c^T$). The results from Chapter 5 show the test of this relation under compression.

1.7 Crystal Structure

The structure of solids is one of the most important features of a material, not only affecting the macroscopic appearance of a material but also governing many physical properties. For a material to be considered a crystal, it must have a periodic repetition of a base unit cell in three dimensions. Lithium and indeed the remainder of the alkali metals discussed thus far have been assumed to be crystals, and the presence of the symmetry-breaking phase transitions has been referenced (see section 1.1). In light of the importance of this symmetry-breaking phase transitions in lithium to the melting curve and phase transitions in general to the superconducting phase diagram, a discussion of the basic principles of crystal symmetry is warranted.

Structures of crystals are defined in terms of the symmetry present in the solid and dates to the 18th and 19th centuries. These crystal symmetries were first determined by analytical geometry, before the development of diffraction techniques necessary to experimental observe the structures of crystals [59]. There are 4 possible symmetries in a three-dimensional model: translational, rotational, reflection, and inversion. All crystals by definition have translational symmetry; there must be a base unit cell that can be repeated overall space; in other words, the definition of a crystal is a periodic structure. This restriction in turn leads to some limitations in other symmetry elements that are possible for crystals. For example, a shape that has five-fold rotational symmetry (such as star fish with five legs) cannot exist in a crystal since five-legged base unit cell cannot be repeated over all space without gaps. Although such symmetry does exist in nature (e.g., star fish, flower petals), it is not crystalline; such solids with five-fold symmetry are aperiodic and referred to as quasi-crystals [139, 159, 186].

For each symmetry element, we can consider an associated symmetry operation; examples are shown in Figure 1.1. We can consider a translational symmetry operation acting

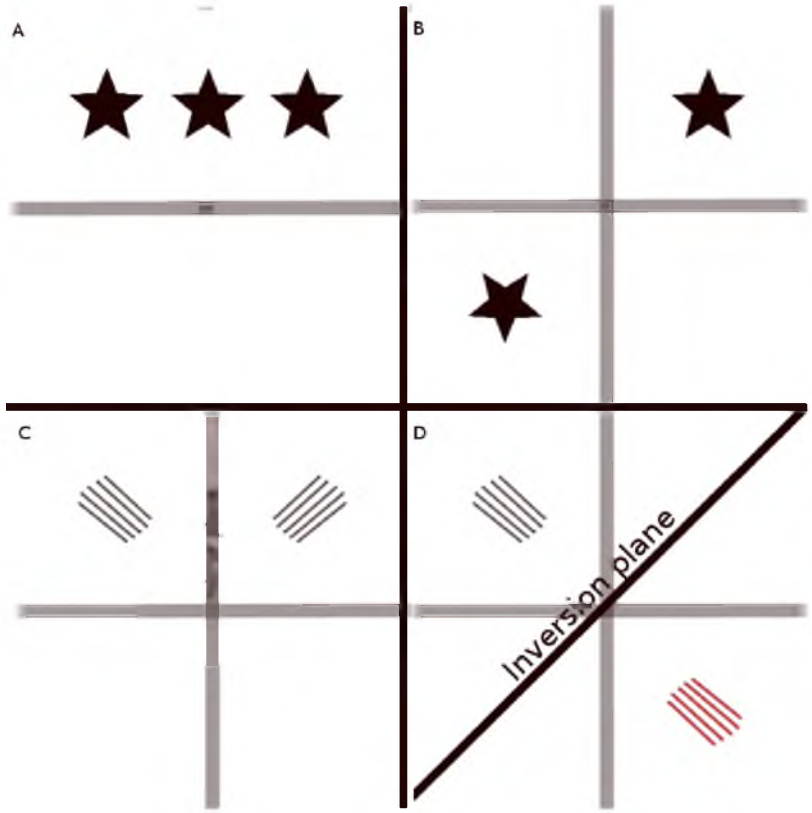

Figure 1.1. An example of different symmetry operations. Panel A shows translational symmetry in one dimension, a motif copied at a certain distance away. Panel B shows 2-fold rotational symmetry. The center of rotation is the origin of the two-dimensional coordinate system drawn in the panel. Panel C shows a reflection operation. The mirror plane is drawn along the vertical axis. Panel D shows an inversion operation. The inversion plane, for convenience, is drawn diagonally across the panel. The opposite side of the motif is drawn in red to illustrate the operation. The underside of the motif in the top left quadrant of the panel is red, after the inversion operation, the underside of the motif is now face up.

upon a basis, or to be more general, a motif, to copy the motif at some vector, T_1, away from the original. For example, if a motif is at the origin of a three-dimensional Cartesian coordinate system and a translation operation is carried out in the x-direction, the result is a motif at x = 0, T_1, $2T_1$, etc. A rotational operation simply rotates the motif about a center of rotation. This is limited by the necessity of translational symmetry, meaning only some rotations are allowed: 1-fold, 2-fold, 3-fold, 4-fold, and 6-fold rotational symmetries. For example, 1-fold rotational symmetry centered about the origin of a coordinate system for a motif at a position of x=1, y=1, z=0 rotates the motif by 2π in x and y and the result is a copy of the motif at the exact same position as the original. As another example, 2-fold rotational symmetry on the original motif at x=1, y=1, z=0 would result in a copy of the

motif at x=-1, y=-1, z=0. For a reflection operation, we can consider drawing a mirror plane a distance d from the motif, then a reflection of the motif on the other side of the mirror plane at a distance of d. The result is two motifs of opposite handedness or chirality a distance of $2d$ from each other. If a motif were at position x=1, y=1, z=1, and a mirror plane were drawn on the x-axis, the result would be a motif with opposite relative chirality at position x=-1, y=1, z=1. An inversion symmetry operation is only possible in at least three dimensions; it is very similar to reflection, however, it simply takes into account the three-dimensional shape of the motif. An example would be a three-dimensional motif of a pyramid with the apex pointing out of the page; the result of an inversion operation with the center of inversion in the center of the motif would be a motif with the apex pointing into the page. It is interesting to note that in a two-dimensional space, inversion is not distinguishable from reflection, and only 3 symmetries are possible. Following this trend, in a four-dimensional space, there are five possible symmetries, and so on. At times, when considering other such factors as magnetism, electron spin can be treated as another dimension and another symmetry operation may be added. However, in this work, only three-dimensional solids are considered.

There are also symmetry operations which involve the combination of two symmetry operations: glide planes and screw-axes. A glide plane is a reflection in a plane followed by a translation parallel to that plane. A nice example of this is footprints; starting with a left foot print at x=-1, y=0, then a reflection of that foot print makes a right foot print at x=1 but the y position is y=$\frac{1}{2}$ instead of y=0. A screw-axis is a rotation about a center followed by a translation.

These symmetry operations are related to one other in some very specific manners, which can be explained in terms of group theory. The four symmetry properties from a finite group and demonstrate the four properties of a group: Closure, Associativity, Identity, and Inversion. Closure ($G_1 \star G_2 = G_3$) requires that any combination of two elements result in a third element. It should be noted that $\star$ represents a generic binary operation. For example, if we start with a motif x=1, y=1, z=0, and apply 2-fold rotation, then apply a mirror plane on the y-axis, the result is the same as if we drew a mirror plane on the x-axis. The application of two symmetry operations has the same result as the application of a third. Associativity of symmetry operations requires that the grouping of the symmetry operations can be changed and not affect the result, $((G_1 \star G_2) \star G_3 = G_1 \star (G_2 \star G_3))$. Referring to the previous example, we could apply two of the symmetry operations on a motif; draw the mirror plane on the x-axis first, then draw another mirror plane on the y-axis. We can

then applying a 2-fold rotational operation on the resultant motif to return to the original motif. We can also take the original motif, draw a mirror plane on the y-axis, then apply a 2-fold rotational operation. We then draw a mirror plane on the x-axis and apply it to the resultant motif to return to the original motif. Identity ($E \star G_1 = G_1 \star E = G_1$) requires that there be a symmetry operation that serves as unity. The 1-fold rotational operation serves this purpose. Inversion ($G_1^{-1} \star G_1 = G_1 \star G_1^{-1} = E$) requires that each symmetry operation has an inverse. Each nonrotational or translational symmetry operation serves as its own inverse. For rotational and translational symmetry, the direction of rotation and translation is reversed for the inverse.

This finite number of crystal symmetries means these elements can only interact with each other forming a limited number of symmetry groups, shown in Tables 1.1 and 1.2. It is the combination of these symmetry elements in a group that define the crystallographic axes, lattice parameters a,b,c (which are measurable distances between lattice sites), and angles between the lattice parameters α, β, γ. All possible groups have been divided into 7 crystal systems, within which are 14 Bravais lattices. The Bravais lattices are generated from the combination the seven crystal systems with the seven types of lattices centering

Table 1.1. Crystal Systems.

Crystal System	Symmetry	Lattice parameters	Bravais Lattices
Triclinic	no axes other than 1-fold rotation or inversion, no mirror plane	$a \neq b \neq c; \alpha \neq \beta \neq \gamma \neq 90°$	Primitive
Monoclinic	Unique 2-fold and (or) single mirror plane	$a \neq b \neq c; \alpha = \gamma = 90°, \beta \neq 90°$	Primitive, Base-Centered (C)
Orthorhombic	3 mutually perpendicular 2-fold axes, rotation or inversion	$a \neq b \neq c; \alpha = \beta = \gamma = 90°$	Primitive, Base-Centered (C), Body-Centered, Face-Centered
Trigonal	Unique 3-fold axis, rotation or inversion	$a = b = c; \alpha = \beta = \gamma \neq 90°$	Primitive
Tetragonal	Unique 4-fold axis, rotation or inversion	$a = b, a \neq c; \alpha = \beta = \gamma = 90°$	Primitive, Body-Centered
Hexagonal	Unique 6-fold axis, rotation or inversion	$a = b, a \neq c; \alpha = \beta = 90°, \gamma = 120°$	Primitive
Cubic	4 3−fold axes, rotation or inversion along 4 body diagonals of a cube	$a = b = c; \alpha = \beta = \gamma = 90°$	Primitive, Body-Centered, Face-Centered

Table 1.2. Lattice Centering.

Lattice Centering Type	
Primitive (P)	lattice sites on each corner of the unit cell
Body-Centered (I)	lattice sites on each corner of the unit cell plus one in the center
Face-Centered (F)	lattice sites on each corner of the unit cell plus lattice site in center of each face of the unit cell
Base-Centered (3 types: A,B, or C)	lattice site on each corner of the unit cell plus one additional lattice site on the face of each pair of parallel faces
Rhombohedral (R)	lattice site only on the corners of the unit cell where $a = b = c$ and $\alpha = \beta = \gamma \neq 90°$

which are outlined in Table 1.2. Using this understanding of symmetry and the constraint of periodicity for a crystal, the number of possible space groups for a crystal is limited to 230 distinct types.

Metals tend to have very simple crystal structures, with the alkali metals at ambient pressure all in a body centered cubic phase, bcc. All the alkali metals undergo phase transitions to a face centered cubic phase, fcc, with the application of pressure. In the case of lithium (and to a more limited extent, Na and K), there is also a temperature-driven martensitic phase transformation to a hexagonal symmetry with a basis of 3 atoms, hR3 (space group 166) [13]. A martensitic phase transformation is a type of diffusion-less phase transformation that forms from crystal planes slipping along faults. Details of the phase transitions of the bcc, fcc, and hR3 phases of lithium are described in detail in Chapter 6. At higher pressures, the akali metals all undergo phase transitions to crystal structures with lower symmetries than the cubic phases bcc and fcc. This change in the structure also causes other changes in the physical properties of the crystals; in the case of Na and Li, there is even a change from the metallic phase to an insulator phase [111, 119, 132].

1.8 Fermi Surface

The location and topology of the Fermi surface describes the low temperature properties of metals. This is due to the fact that the current that flows through a metal is due to the changes in the occupancy of states near the Fermi surface [91]. The Fermi surface is the direct result of the Pauli exclusion principle, which only allows two electrons (one spin up, $\uparrow$, one spin down, $\downarrow$) per orbital. The Fermi surface is the abstract boundary in momentum space (k-space) which separates the filled orbitals from the unfilled orbitals at absolute

zero. This boundary constructs a surface of constant energy in the k-space known as the Fermi-energy, ϵ_F.

A free electron Fermi surface is perfectly spherical with a radius k_F, the Fermi vector, which is determined from valence electron concentration. We can define the Fermi energy by finding the solution for the energy levels from the Schrödinger equation [91]:

$$\begin{aligned} &-\frac{\hbar^2}{2m}\left(\frac{\partial^2}{\partial x^2}+\frac{\partial^2}{\partial y^2}+\frac{\partial^2}{\partial z^2}\right)\psi_k(r)+\psi_k V(r)=\epsilon_k\psi_k(r) \\ &V(r)\longrightarrow 0 \end{aligned} \tag{1.16}$$

if we consider an electron in a cube with sides of length L, and boundary condition, $\psi_k(x,y,z)=0$ at $x,y,z=0,L$ 1.16 has the solution:

$$\psi_n(x,y,z)=A\sin\left(\frac{\pi n_x x}{L}\right)\sin\left(\frac{\pi n_y y}{L}\right)\sin\left(\frac{\pi n z_z}{L}\right) \tag{1.17}$$

For a three-dimensional box, the wavefunction is a standing wave, confined to space of length L. For a solid with a lattice, however, the wavefunction is required to be periodic in all three dimensions. Considering a cubic lattice with a lattice constant of length a, we require that the wavefunction, in all dimensions, have a period a:

$$\psi_{\vec{k}}(\vec{r})=e^{i\vec{k}\cdot\vec{r}}\psi_n(x,y,z)=\psi_n(x+a,y,z)=\psi_n(x,y+a,z)=\psi_n(x,y,z+a) \tag{1.18}$$

The wavevectors are defined as $k_x,k_y,k_z=\pm\frac{2n\pi}{a},n=0,1,2,3....$ Then, solving for the energy, we have:

$$\epsilon_{\vec{k}}=\frac{\hbar^2}{2m}(\vec{k}^2) \tag{1.19}$$

Now consider n_F to be the topmost filled energy level in a free electron gas (n_F is the number of filled orbitals), and represented by points inside a sphere in momentum space. This volume of this sphere is defined by the Fermi vector k_F. The volume (in real space is a^3) can be expressed in terms of the Fermi vector:

$$|\vec{k}_F|=\left(\frac{3\pi^2 n_F}{a^3}\right)^{\frac{1}{3}} \tag{1.20}$$

and the constant energy at the surface of that sphere is the Fermi energy ϵ_F:

$$\epsilon_F=\frac{\hbar^2}{2m}|\vec{k}_F^2|=\frac{\hbar^2}{2m}\left(\frac{3\pi^2 n_F}{a^3}\right)^{\frac{2}{3}} \tag{1.21}$$

The total volume of the Fermi surface, the overall size, depends only upon electron concentration [91]. Since lithium, like all alkali metals, has only one valence electron, it has

a low electron concentration and the calcultaed volume enclosed by the Fermi surface is significantly smaller than the volume of the first Brillouin Zone (BZ).

The actual shape of the Fermi surface in real metals can be much more complex than the surface of a sphere. Even in the alkali metals, the shape is only nearly spherical. The shape is distorted by interactions with the lattice. In the case of the alkali metals (at least in the bcc phase), the Fermi surface is far enough from the boundaries of the first BZ, since the alkali metals have one conduction electron and a low electronic density of states, and thus have minimal lattice interaction and distortion [91, 102]. In the case of metals in which the Fermi Surface is close to the boundaries of the BZ, or it crosses the first BZ, the shape of the Fermi surface becomes very far from a sphere. The Fermi surface is generally presented in the reduced zone scheme, much like band structure, in which all bands are shown folded in on the first BZ; see Figure 1.2.

Constructions of the Fermi surface can be made with measurements of quantum oscillations in resistance (Shuninkov de Haas Effect [161]) or magnetic moment (de Haas van Alphen Effect [161], see section 2.5). These measurements are often accompanied by detailed information regarding the crystal structure of the metal (generally obtained through x-ray or neutron crystallography) and the band structure. However, some general qualitative rules outlined by Kittel [91] can be followed to estimate the shape of the Fermi surface: The interaction of the electron with the lattice creates energy gaps in the zone boundaries of the periodic lattice. In all cases (unless time-reversal symmetry is violated), the Fermi surface

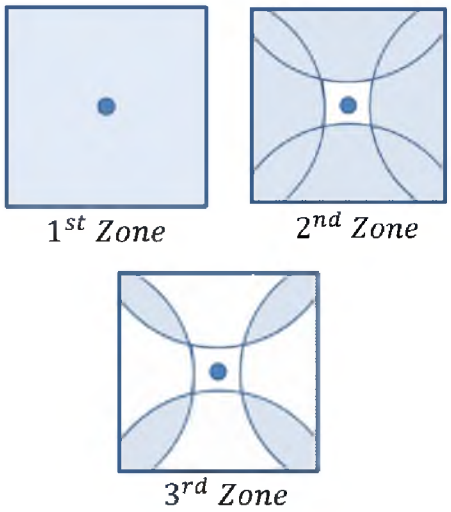

Figure 1.2. An example of the reduced zone scheme presenting a Fermi surface.

perpendicularly intersects in the zone boundaries from the condition $\frac{dE}{d\vec{k}} = \frac{\hbar^2}{m}(\vec{k} - \frac{1}{2}\vec{G})$, where $\vec{G}$ represents the reciprocal lattice vector. The lattice potential serves to "round" any sharp corners of the Fermi surface. Applying these constraints to the shape of the Fermi surface and producing them in the reduced zone scheme can lead to many exotic shapes [91].

CHAPTER 2

EXPERIMENTAL TECHNIQUES

This chapter presents the experimental techniques used to obtain the results presented in Chapters 3, 4, 5, 6, and 8. These include the techniques for reaching high pressures, high or low temperatures, as well as measuring physical properties such as resistivity and magnetic susceptibility.

2.1 Pressure

In section 1.4.1, the pressure as a thermodynamic variable is explained in detail. This section is concerned with practical application of pressure. In this work, these pressures were achieved most commonly in a Diamond Anvil Cell (DAC) (pressures ranging from 0 to $\approx$ 65 GPa), also using a Paris-Edinburgh (PE) Press (0 to $\approx$ 7 GPa).

2.1.1 Diamond Anvil Cell

In a DAC, high pressure is applied by squeezing the sample between two diamond tips (culets). Typical sizes of the culets in this work range from 200 to 500 μm in diameter; different cuts of diamonds are shown in Figure 2.1. The small size of the culet and the hardness of the diamond are the two main factors that allow for very high pressures. There are many different designs of DACs; the common elements are shown in Figure 2.2. Two designs used in this work are plate DACs and piston cylinder DACs shown in Figures 2.3, 2.4, and 2.5. The basic designs of these DACs have mostly the same components: two diamonds, positioned opposite of each other with the culets facing each other; the diamonds are placed on seats (generally something hard such as tungsten carbide); one or both seats may be positionable by means of lateral screws that hold the seat in the body of the DAC; one seat may also be attached to a rocker, held in the body of the DAC with screws, the positioning of which allows for relative tilt adjustment. The elegantly simple idea of applying very high pressures between two diamonds is complicated by the degree of precision required to machine and manufacture bodies of DACs capable of securing the seats and diamonds

Figure 2.1. Two different cuts of diamonds commercially available from Almax-easylab. On the left is a conventional cut of diamond and seat, on the right is a Boehler cut seat and seat designed to fit the cut [17]. Images are courtesy of Alamx-easylab.

in a stable yet adjustable manner (the ability of the DAC to be adjusted is necessary for the alignment of the culets, since if the culets are not aligned with respect to each other, pressure will not be possible).

Before any measurement is possible, the two opposing diamonds must first be aligned with some precision to guarantee that the two culets are as parallel as possible. The amount of alignment possible depends upon the design of the DAC. Some DACs allow only lateral alignment, others have means of adjusting the relative tilt. The technique used in this work is as follows: First the diamonds are epoxied on the seats (typically, these are made of tungsten carbide, for its hardness). The interface of the diamonds and seats must be completely cleaned prior to the application of epoxy, otherwise the subsequent alignment may be affected. After the diamonds and seats are completely clean, the diamonds are aligned relative to each the seat according to Figure 2.1 such that the culet of each diamond and the opening in each seat form concentric circles. When using Boehler cut diamonds [17], see the right side of Figure 2.1, this step is much easier. Each diamond is then pressed tightly against the seat and minimal amounts of epoxy are applied, generally in three small dots spaced evenly around the diamond. After the epoxy has set enough to prevent the diamonds from falling out of the seats, the DAC can be preliminarily aligned. After aligning the lateral and the tilt (to some extent) if possible, a flattened piece of metal (generally a 250 μm stainless foil) is placed between the diamonds, and epoxy is applied to the remainder diamond-seat interface. Enough pressure is applied to slightly deform the metal, making imprints of the diamond culets in the metal. The epoxy is then allowed to cure with the pressure applied. This helps to align the tilt, and in the cases where the DAC does not have a tilt adjustment, it may be the only way to align the tilt. After the epoxy has cured, the alignment may be completed. All alignments pertain to the relevant position of the culets to each other. Looking from the back of a diamond through the culet, one should see the two culets as concentric circles, if the diamonds are brought close enough to barely

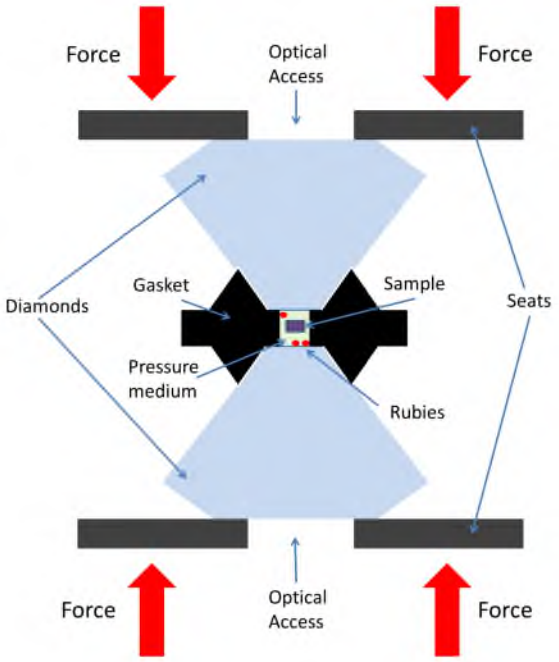

Figure 2.2. Cross section diagram of a DAC. This figure was inspired by the diagram presented in http://pubs.rsc.org/en/content/articlelanding/2013.

touch each other, the culets ought to lay on top of each other. The amount of the tilt misalignment between the culets can be seen by means of interference fringes between the two diamond surfaces. Depending of the style of DAC, the tilt can be adjusted to have very few interference fringes (such as two or three colors, or a partial fringe) or even one solid color. The tilt can also be limited by the size of the culet, with smaller culets having more ease of alignment.

If the diamonds are not aligned, then when pressure is applied to the sample, the diamonds will be in danger of breaking. If the tilt is far off and the diamonds touch, even with very little pressure, they can break each other.

Another flattened metal foil (which is now the 'gasket') is then placed between the diamonds and an indent is made. This deforms the gasket, making an impression of the diamonds in the metal. The indentation process allows one to drill a small hole ($\sim \frac{1}{2}$ to $\frac{1}{3}$ the culet size) in the center of culet indent, it also precompresses the gasket material so that the sample chamber hole will be stable (it will be harder and less liable to collapse as excess material flows into the hole when pressed, nor expand as the material flows away from the culets, and when centered properly, it ought not drift far from the center). If too much pressure is applied, the gasket will fail by becoming too thin, then the diamonds will

Figure 2.3. A plate DAC from Almax-easylab; inside a home-made oven it is capable of reaching temperatures of $\approx$ 600 K. Pressure inside the DAC is applied by tightening the three inner screw simultaneously by means of a customized gear box. The diamond seat fits into the bottom plate secured by three set screws, which allow for lateral adjustment of the bottom diamond. The top seat is pressed into top plate and not mobile. The three outside screws can be adjusted to align the tilt of the top diamond. This DAC allows for accurate alignment of diamonds and is capable of pressures of $\sim$ 50 GPa with 500 μm diameter culet diamonds and higher pressures with smaller culets. It has little change in pressure ($\pm$2 GPa) with the application of low temperature ($\sim$4 K) to moderately high temperature ($\sim$ 500 K). Picture courtesy of Alamx-easylab.

punch through the gasket, touch each other, and break. Also, if there is misalignment of the diamonds, the gasket hole will drift. The danger to the diamonds is if the hole drifts off of the edge of the culet. At this point, the diamonds would be pushed through the hole, touch each other, and break.

2.1.2 Paris-Edinburgh Press

Experiments performed at Oak Ridge National Laboratory used a Paris-Edinburgh (PE) Press to apply pressures from ambient pressure to $\approx$ 7 GPa. A PE Press consists of two opposing pistons which can be driven together by means of hydraulics (chambers can be filled with oil to displace the pistons, thus pushing them together), shown in Figure 2.6. Anvils typically made of a hard material are placed on the opposing pistons. For these experiments, the anvils were made of cubic boron nitride. The anvils are designed with an indentation that fits a gasket (in this case, a single toroidal gasket was used). The two

Figure 2.4. Another style of plate DAC; this is a miniature model manufactured by HPDO (hpdo.com). The pressure is applied by means of the three pressure screws. The posts attached to the bottom plate fit snugly into the top plate and preserve the diamond alignment as pressure is applied by gently tightening each screw separately. Both seats are attached to the plate by means of set screws, allowing for lateral adjustments. The only mechanism to adjust the tilt is by properly epoxying the diamonds; see section 2.1.1.

anvils, much like in the case of the DAC, must be aligned in order to assure that the two gasket indentations are directly oppose each other. Also as in the case of a DAC, if the anvils are misaligned, then the entire pressure apparatus, would not only fail to provide pressure to the sample but could also fail catastrophically.

2.1.3 Pressure Measurement

The pressure can be measured using various pressure markers, ruby fluorescence being one of the most common. Another means of measuring pressure is using a known equation of state (eos) of the material, the change in unit cell volume as a function of pressure.

2.1.3.1 Ruby Fluorescence

In this work, ruby (Al_2O_3:Cr, alumina with chromium doping) fluorescence was the main source of pressure measurements, typically under nonhydrostatic conditions using the standard calibration [114, 45, 54, 195, 28]. Ruby fluoresces when excited by laser as shown in Figure 2.7. The wavelength of this excitation has a pressure dependence. To calibrate the ruby pressure, the fluorescence of the ruby is measured along with a pressure marker that has a well-defined eos (equation of state). The pressure can be determined from measurements of the pressure marker's unit cell (the compression of the unit cell with increasing pressure) and the wavelength of the ruby's fluorescence is recorded at each pressure. The dependence

Figure 2.5. A piston cylinder style DAC designed for resistive heating, capable of reaching temperatures of ≈ 1000 K. Pressure is applied by means of four pressure screws which engage the piston via through-holes in the cylinder, or through the use of a steel membrane which attached to the cylinder directly and applied pressure when inflated with gas. This figure shows the Helios DAC, which is designed for high temperature. Many measurements in the works were also taken using the Diacell Bragg DAC. The styles and alignment of the two are very similar. The bottom seat is secured to the cylinder with four set screws, allowing for lateral adjustment. The top seat is affixed to the cylinder by means of three set screws on a rocker, which allows for very fast and accurate tilt adjustment. Both DACs provide pressures >100 GPa using 200 μm diameter culet; pressures of $\sim$ 50 GPa are routinely achieved. The pressure drift with temperature in the piston-cylinder type DAC is generally not great $\pm$2 GPa, except in the case when the helium membrane is employed when cooling to low temperatures. In this case, the pressure tends to increase by very noticeable amounts of >5 GPa. Picture courtesy of Alamx-easylab.

of the ruby fluorescence as a function of pressure has the form:

$$P = \frac{A}{B}\left[\left(\frac{\lambda}{\lambda_0}\right)^B - 1\right] \tag{2.1}$$

where A and B are constants, λ_0 is the ruby fluorescence wavelength (m) measured at ambient pressure, λ is the ruby fluorescence wavelength under pressure, and the constant A has units of pressure (GPa). The values of the constants depend upon the specific calibration being employed. For the works in this dissertation, the nonhydrostatic pressures were determined from the calibration of Mao and Bell, later extended by Mao et al. [116, 114], in which $A = 1904$ GPa and $B = 7.665$; the authors did not report error bars. This was later refined by Dorogokupets and Oganov, with $A = 1871$ GPa and $B = 10.06$; no specific error bars are presented [45]. The calibrations performed by Mao et al. were performed using Ar as a pressure medium. Even though this is the ruby calibration typically used for

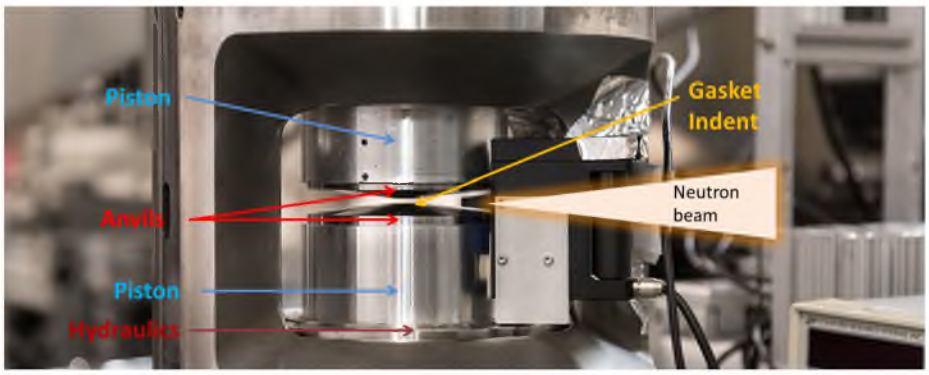

Figure 2.6. Diagram of PE Press. In the configuration shown, the two detectors would be parallel to the page in front and behind the page. Image is the PE Press from SNAP at ORNL: https://neutrons.ornl.gov/snap/sample.

nonhydrostatic measurements, the conditions of the electrical resistance measurements in the following chapters were far more nonhydrostatic than the conditions of the calibration. This leads to a greater systemic error in the pressure measurements. For the AC magnetic susceptibility or XRD measurements, in which a pressure medium can be used, a different calibration was used. For hydrostatic measurements, the calibration of Chijioke et al. was used, $A = 1879 \pm 6.7$ GPa and $B = 10.71 \pm 0.14$ [28].

The typical spectrum of ruby fluorescence appears as a doublet with distinct R1 and R2 peaks. For pressure determination, the R1 peak is measured. However, under nonhydrostatic pressure conditions, the shape of the doublet can change noticeably. As described by [23], the shape of the doublet can change depending upon the type of strain experienced by the ruby crystals (trigonal hR30, R-3c). Broadening of the ruby peaks measured under pressure is often attributed to be a sign of nonhydrostatic conditions [141]; however, it has since been shown to be mostly the result of "nonuniform strain" on the ruby crystals themselves [23]. When strained along the a-axis, the distance between the R1 and R2 ruby peaks increases with increasing pressure; the distance decreases with increasing pressure if the ruby experiences strain along the c-axis [23].

For the data presented in this work, the nonhydrostatic rubies showed a distinct broadening and smearing of the R1 and R2 peaks with increasing pressure. The majority of electrical measurements presented in subsequent chapters relied upon alumina as a layer of electrical insulation between the lithium samples and the metal gasket. Alumina (Al_2O_3) is a hard and relatively incompressible material [123, 83]. With a bulk modulus of $K_0 \approx 254$ GPa [83], alumina inside the sample chamber will result in highly nonhydrostatic conditions and

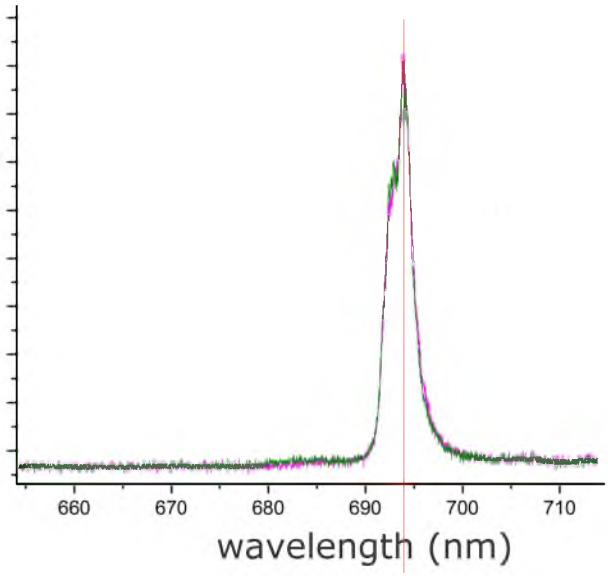

Figure 2.7. This is a typical nonhydrostatic ruby under moderate pressure. The y-axis represents the intensity of the spectrum in arbitrary units. The doublet has already begun to merge, and with increasing pressure, the doublet will continue to broaden and merge as the nonhydrostaticity increases. Finding the middle of the peak in such a situation does not take into account the broadened doublet. The pressure is determined by recording the value of the middle of the peak and the value of two-thirds to the higher wavelength, where the R1 peak would be visible under hydrostatic conditions.

anisotropic pressure. Alumina is used in these experiments due to the paucity of materials that are nonreactive with lithium.

In this work, the width of R1 and R2 spectra lines tends to increase with pressure; this indicates that the rubies, embedded in the alumina, appear to experience such nonuniform strains as described in [23]. Also, the distance between the R1 and R2 peaks in the nonhydrostatic pressures presented in this work decrease with increasing pressure. This is a consistent trend present throughout different samples and experimental runs. It is unlikely that such a majority of ruby pressure markers would be loaded in a manner that they would experience strain along the c-axis; however, most of the nonhydrostatic measurements were made with alumina insulation inside the sample chamber. The method of producing the alumina insulation is described in section 2.3. This method involves forming a sheet of alumina by pressurizing 0.05 μm^3 particle alumina (γ-Al_2O_3) powder in the sample chamber prior to loading of the sample. γ alumina differs from bulk (α) alumina in its structure

and compressibility (K_0 = 144 ± 21 GPa (using a first-order Bridgeman Equation to fit the Equation of State)) [25, 60]. Ruby powder was used in the pressure measurements as well as ruby spheres; however, the spectrum from the particular ruby spheres used was often too weak of a signal to be reliable. Thus, ruby powder was more common for the pressure determination. It is plausible that the alumina powder pressurizes into a sheet with a preferred orientation (the c-axis perpendicular to the diamond culets), causing the distinct decrease in the R1 and R2 distance with increasing pressure. Considering this effect, pressure determinations will benefit from using the R2 peak, as the R1 peak appears underestimate the pressure of the sample [23].

The ruby fluorescence also has a measured temperature dependence; the wavelength of the fluorescence decreases as a function of temperature as measured against pressure markers with known eos as well as thermal expansion coefficients [54, 195]. Thus, the temperature at which the ruby fluorescence is measured must also be recorded. Also, the R2 line disappears at low temperatures, leaving a sharper single R1 line. For low temperatures (<10 K), a different calibration is necessary [54, 195]:

$$P = A_0 \ln\left(\frac{\lambda}{\lambda_0}\right) \tag{2.2}$$

the constant A_0 has units of GPa, and A_0 = 1762 ±13 GPa.

2.1.3.2 Equation of State

The eos of lithium or NaCl, [40, 75], were also used in Chapter 6 of this work to measure the pressure inside the cell. The equation of state describes the variation of a solid's volume as a function of pressure and temperature. Measurements of X-ray or neutron diffraction give the spacings (d) of the lattice planes, which in turn give the unit cell volume. Measuring the equation of state of a material requires determination of the unit cell at different pressures. This allows for the determination of the bulk modulus and its derivative:

$$\begin{aligned} K &= -V\frac{\partial P}{\partial V} \\ K' &= -\frac{\partial K}{\partial P} \end{aligned} \tag{2.3}$$

This parameter describes how much the material resists compression. A lower value for K indicates a more compressible material, a material which will display a rather steep decrease in volume as a function of pressure. The equation of state of many materials, including NaCl and Li, have been previously measured [182, 40, 75, 74]. Thus, using these data as a calibration, we are able to measure the unit cell volume of the Li or NaCl and

determine the pressure of the sample. For more sensitive pressure markers, compressible materials with small bulk moduli are preferred.

There are several functions which can be used to fit the volume versus pressure or temperature data [1]. In the results presented in Chapter 6, the Vinet fit was used to fit the data for lithium, as this particular fit is derived from a general interatomic potential and is appropriate for simple solids [1, 181, 33] and was also used in previous works [74]. The Vinet fit:

$$P = 3K_0 \frac{1 - \left(\frac{V}{V_0}\right)^{\frac{1}{3}}}{\left(\frac{V}{V_0}\right)^{\frac{2}{3}}} e^{\frac{3}{2}(K'-1)(1-\left(\frac{V}{V_0}\right)^{\frac{1}{3}})} \tag{2.4}$$

where the subscript 0 denotes the values at zero pressure (or ambient pressure). An example of the Vinet fit used for lithium can be seen in Chapter 6.

2.2 Temperature

In this work, low temperature and moderately high temperature techniques were employed.

2.2.1 Low Temperature

At low temperatures, the energy becomes less and less dominated by k_BT, allowing more subtle energies, such as zero point motion, to become detectable.

2.2.1.1 Cryostat

Low temperatures, <2 K, for table top experiments at the University of Utah were achieved by means of cooling inside a liquid ^{4}He continuous flow cryostat (Janis Research Co. Model SVT-200-5), and a cryogen-free closed cycle cryostat (Janis Research Co. Model SHI-950-15).

A continuous flow cryostat typically consists of several different sections or layers. The innermost section is the sample tube, in which a rod with the sample (in our case a DAC) attached at the bottom is inserted. The next layer out can be filled with a cryogen, either liquid helium or liquid nitrogen. In the case of liquid helium use, there is another layer which is filled with liquid nitrogen to prevent excess boil off of liquid helium. The cryostat is thermally insulated with a high vacuum jacket. This type of cryostat achieves low temperatures by transferring the cryogen, typically liquid helium, from a storage dewar to inner cryogen chamber of the cryostat and then controlling the rate of the flow of the cryogen to the sample tube. Due to inconsistent rates of cooling, most notably in the liquid ^{4}He system, heating curves were analyzed for temperature effects by letting a small pool of

liquid helium into the bottom of the cryostat sample tube, applying a vacuum, and allowing the system to heat passively.

A closed cycle cryostat has a chamber in which a similar rod with the sample (in our case a DAC) attached at the bottom is inserted. Cold helium gas is pumped through the chamber and an external mechanical pump extracts the warmer helium gas to cool and recycle. The DAC on the rod is cooled by being in thermal contact with a metal cold point of contact with the sample chamber walls. Once the system reaches the temperature of liquid helium, the sample chamber can be filled with helium gas which will liquefy upon contact with the metal cold chamber walls. In this manner, a small amount of liquid helium can pool into the bottom of the cryostat. A steady, slow heating can be achieved by forming a small pool of helium applying a vacuum and allowing the system to passively heat (in the same manner as in the continuous flow cryostat). This also allows the measurement to be taken without the vibrations of the chiller affecting the data.

For the experiments performed with the High Pressure Collaborative Access Team from the Carnegie Institute of Science in the Advance Photon Source at Argonne National Laboratory, a home-made continuous flow cryostat was used. The cryostat was made to be of a small enough size to fit into the synchrotron X-ray beam, which limited the base temperature to $\approx$ 10 K. As with the Janis systems, the cryostat is insulated with a vacuum jacket. A liquid helium dewar is connected to the cryostat and an open flow cools the system to base temperature by flow pipe of liquid helium in contact with the metal (Cu, due to it thermal conductivity) sample holder. A series of heaters near the DAC and Cu DAC holder serve to balance the temperature if higher than base temperature is desired.

For experiments performed in the National High Magnetic Field Laboratory, low temperatures of 0.3 K were achieved using an Oxford systems top loading ^{3}He cryostat.

For experiments performed at Oak Ridge National Laboratory, low temperatures were limited to about the boiling point of nitrogen ($\approx$ 77 K). A home-made system of circulating LN2 was used to keep the pressure cell (a PE press) cold and a series of heaters were employed to raise the temperature above the base temperature, and balancing the heaters versus the circulating LN2 could keep a mostly constant temperature ($\pm$ 5 K). Due to the large mass of the pressure cell, using liquid helium was prohibitively expensive.

2.2.2 High Temperature

While low temperatures are key for the search of quantum solids, high temperature experiments also play a role. There are two popular strategies for applying heat to a sample inside a DAC: to apply heat to the sample only, keeping diamonds, gasket, and

body of the DAC at a colder and more constant temperature; or to heat the entire DAC evenly (the same strategy as cooling the entire DAC in the cryostat), slowly, and steadily to avoid thermal lag issues.

2.2.2.1 Laser Heating

Laser heating is a common technique used when one simply wants to heat the sample locally (not the entire DAC), or even to heat only a small portion of the sample. There are many reasons why one would desire to do this, most notably when wishing to heat the sample to temperatures that would damage, weaken, or even melt the gasket material or the other materials of the DAC. For instance, attempting to recreate conditions to melt iron under the extreme pressures (conditions near the molten/solid mantle interface) would require temperatures certainly high enough to melt an entire DAC (if it was made of a material such as hardened steel). In order to heat only the sample to these >1000 K temperatures, a high power laser (generally in the near IR range), is focused on the sample, or a portion of the sample. Increasing the laser power increases the temperature of the sample. For some samples, such as hydrogen, an absorber is placed in the sample chamber of the DAC with the sample to absorb the laser power and heat the sample [41].

In this type of laser heating experiment, the temperature must be measured remotely. A popular technique used to measure temperature is the collection of the black body radiation emitted from the sample [41, 16]. The error in temperature can be determined though the fit to a calculated black body spectrum, which can lead to large error bars. The emitted radiation is collected from the sample and split into two portions; one portion goes to the detector (in order to fit into the black body curve), and the other portion is generally used for a visual image of the sample which is in turn used to confirm that the laser is striking the appropriate piece of the sample and also to possibly monitor the laser reflections from the sample (for example, speckle motion can be used to determine if the laser is reflected from a solid or a liquid, see section 3.3 [16]).

2.2.2.2 Resistive Heating

For lower temperatures, temperatures which are not likely to damage the DAC, resistance heating techniques can be used rather than laser heating. In many cases, only relatively low increases in temperatures are desired, such temperatures would require low power lasers and would be so low that distinguishing the black body signal from the room temperature is problematic. In these cases, resistively heating the entire cell is a possible solution. In this work, two different resistive heating methods were used. The first used a

plate DAC made by Almax-easylab, and to measure temperature, a K-type thermocouple was anchored to the bottom side of the top plate, resting against the side of the diamond and insulated with Kapton. The DAC and a thermocouple were placed inside a clay cylinder which had a high resistance nichrome coil inside. This whole assembly was placed in a 4 inch diameter petri dish, with the thermocouple wire, two ends of the nichrome coil wires, as well as the four electrical probe wires leading to the outside. Either a whiteclay lid with a glass window or a standard petri dish cover was used to close the home-made oven, depending on the need for quality optical access. The oven was then mostly sealed with electrical tape; vents were left on purpose to prevent overpressure forming from expansion of hot gas. By applying voltage across the nichrome coils, the high resistance, R, of the nichrome generates heat, where the heat, P, is related to the voltage, V, by: $P = \frac{V^2}{R}$. This system was capable of reaching temperatures of ≈ 600 K. Another system for resistively heating a DAC is using a DAC designed to reach high temperatures. The Almax-easylab Helios DAC is a piston-cylinder type diamond anvil cell that has a resistive heater built near the base of one diamond. A gasket may be placed in contact with the heater. The thermocouple may also be fed through a small opening to come into contact with the gasket. The heater is externally powered by leads reaching out of the cylinder. This setup is capable of reaching higher temperatures of ≈ 1000 K.

2.3 High Pressure Resistance Measurements

Resistance is an excellent material property to measure, since it is a relatively straightforward measurement to perform and analyse. This makes resistance measurements at high pressure incredibly useful. Resistivity (the inverse of a material's conductivity) is an intensive material property; its value is independent of the amount of material present or the type of electrical measurement employed [66]. Resistivity is a function of temperature; the behaviour of the resistivity as temperature is varied reveals whether the material is a metal, or a semi-metal, or even if it is high quality metal or not. The resistivity of metal can be described by the Matthieson rule:

$$\rho(T) = \rho_0 + \rho_i(T) \tag{2.5}$$

where ρ_0 represents the resistivity, or impedance of current carrying electrons, from impurities and ρ_i is the intrinsic resistivity of the material [27, 120]. This work is chiefly concerned with resistivity of metals. If a material becomes less resistive (more able to carry current) as temperature is decreased, then it is exhibiting metallic behaviour [66]; the slope of that decrease gives information regarding the quality of the metal.

A cartoon picture to consider is the following: If one considers a metal as a material that has 'free' electrons, the electrons have the ability to carry electric current through a metal. A material at a nonzero temperature is not completely still. The ions forming the lattice will have motion due to the thermal energy, k_BT (or in the case of a quantum solid, motion from zero-point energy). The motion of the lattice ions, expressed as phonons, can create random points of interaction for the electrons. Therefore, a portion of the current (consisting of current carrying electrons), instead of flowing through the lattice without impedance, actually experiences impedance through interaction with lattice phonons. Thus, the current is impeded by the thermal motion of lattice ions. A simple metal (with the Fermi surface contained entirely inside the first Brillouin Zone) has an intrinsic ability to conduct a current; in a completely defect-free crystal, the current would be infinite in the absence of lattice motion. Thus, at zero temperature, and in the absence of zero-point motion, a perfect simple metal crystal would be an ideal conductor, with zero resistivity (the inverse of conductivity). (For metals in which the Fermi surface crosses the Brillouin Zone boundaries, there is a nonzero resistivity due to umklapp processes.) The intrinsic resistivity of metal, ρ_i, is due to electron-phonon interactions. This can be expressed as a function of temperature by the Gruneison-Bloch relation [138, 68]:

$$\rho_i(T) = \frac{C}{M\Theta_R}\left(\frac{T}{\Theta_R}\right)^5 \int_0^{\frac{\Theta_R}{T}} dz \frac{z^5}{(e^z-1)(1-e^{-}z)} \tag{2.6}$$

where C is a constant, M is the atomic weight, T is the absolute temperature, and Θ_R is the empirical temperature characterizing the metal's ideal resistivity, analogous to the Debye temperature, Θ_D, which characterizes the specific heat of a sample [27]. At high temperature, $T \gg \Theta_D$, the number of phonons liable to interact with electrons is directly proportional to the temperature [6]. Thus, the resistivity becomes a linear function with respect to the temperature:

$$\rho_i(T) \sim T, T \gg \Theta_D \tag{2.7}$$

Below about $0.1\Theta_R$, $\Theta_R \approx \Theta_D$, the integral in 2.6 is a constant and the expression can be reduced to:

$$\rho_i(T) \approx \frac{C_1}{M}\frac{T^5}{\Theta_R^6} \tag{2.8}$$

where is $C_1 = 124.4C$ [27]. The Gruneison-Bloch equation is relevant for simple metals characterized by nearly spherical Fermi surfaces, making it applicable to lithium and other alkali metals, though not over the entire temperature range. It is a good approximation for alkali metals, particularly at low and high temperatures.

Metals have a recognizable trend in resistivity as a function of temperature as seen in this equation. When the system is cooled, the thermal motion of the ions is reduced, thus decreasing the number of possible random electron-phonon interactions. Thus, the ability to carry electric current (the conductance) increases, reducing the resistivity as a function of temperature. If we see the resistivity decrease as a function of temperature, then it can be interpreted that the interactions between the phonons (produced by the thermal motion of the lattice ions) and electrons are decreasing. In other words, as the lattice ions move less and less due to the decreasing thermal energy, then the current flows through the lattice with less impedance, meaning the material has less resistivity.

Impurities cause defects or distortions in the lattice, which serve as additional sources of impedance for the current (ρ_0). The slope at which the resistivity decreases as a function of temperature can also be used to determine the quality of a metal sample. This is expressed by the RRR (residual-resistance ratio); this value of samples is sometimes reported to indicate how free a metal is from impurities. The RRR value is the resistance at room temperature divided by the resistance of the sample at low temperature, generally $\sim$ 4 K; the higher the number (the greater the slope of the decrease of resistivity as a function of temperature) the more pure the metal is. If the slope of decrease is very rapid, then this may show that the majority of the resistance is due to intrinsic resistivity, $\rho_i(T)$ (as opposed to impurities or defects, ρ_0) [31]. The steeper the rate of descent of resistivity as function of temperature, the more pure the sample.

The slope of the resistivity as a function of temperature may also show that the material is not a particularly good metal. The mean free path of the electrons through the materials may be short, and the slowing of the motion of the lattice ions may not strongly affect the short mean free path of electrons. Thus, we are left with the resistivity decreasing as a function of temperature, though perhaps with a shallow slope.

The nature of the decrease of resistivity as a function of temperature may also change once lower temperatures have been reached. A common example is Pt, the slope of the resistivity is quite steep with the decrease in temperature until near 20 K [142]. At this point, magnetic impurities begin to dominate the trend, and the resistivity becomes nearly constant as a function of temperature (0 K $<$ T $<$ $\sim$20 K). Whilst these magnetic impurities were not apparent at higher temperatures, once the intrinsic resistivity (ρ_i) has diminished, they become the dominant source of the resistivity of the material.

There is much information regarding the sample embedded in the resistivity as a function temperature, including information regarding the material's structure. Whilst *resistivity* is

an intensive material property, it must never be forgotten that what is actually measured is *resistance*. Resistance, as opposed to resistivity, is an extensive property; it *does* depend upon the amount of material measured and the configuration of the electrical probe employed. These have a very simple relation: $\rho = \frac{A}{l}R$ (drawn in Figure 2.8); where resistivity is ρ, resistance is R, cross-sectional area of the sample is shown by A, and length of the sample is l (for all practical purposes, this would be the length between the voltage probe). If we apply a known current through a material, we can measure the voltage difference at two points, shown in Figure 2.9. Using Ohm's Law $V = RI$, we control I, the current, and we measure V, the voltage, so we may solve for R, resistance, without much difficulty. However, the sample, as a part of the circuit (with a constant voltage supply), does affect the current. In the case of metals, the correction is too small to be significant. Though to be exact, we would have to include the effect that the sample itself has on the circuit, since the circuit used has a constant voltage source, not a constant current supply. This means the equation to solve for resistance becomes:

$$R = \frac{\sqrt{V_s^2} * \frac{R_c}{V}}{(1 - \frac{\sqrt{V_s^2}}{V})} \tag{2.9}$$

where V_s is the voltage measured (the absolute value is considered as the sign of the voltage can be negative depending upon the phase), V is the constant voltage applied, and R_c is a resistor hard wired into the circuit to give nearly constant current with a constant voltage source.

In all experimental setups, resistance is the parameter that is measured, then the resistivity is calculated from the geometric properties. However, since those geometric properties are present in the relation, $\rho = R\frac{A}{l}$, changes in the geometry of the sample can indeed change the signal. For example, if one measures the resistance and then applies an anisotropic pressure from say the top and bottom (as the case when driving the two diamond

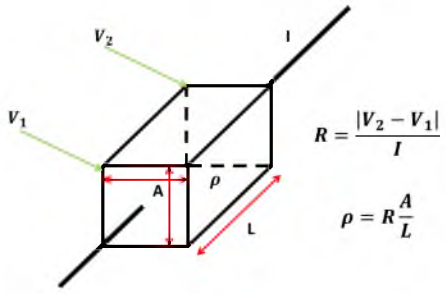

Figure 2.8. A cartoon of the relation between resistance and resistivity.

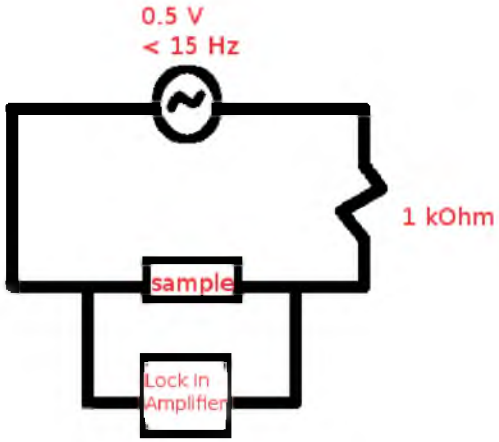

Figure 2.9. A diagram of the circuit used to measure resistance inside of the DAC. The function generator of a SR830 Lock Amplifier was set to values near 0.1 V and < 15 Hz to provide a nearly constant current through the sample. Since the Lock In Amplifier provides a constant voltage source, not a constant current source (though the use of a resistor with a resistance $\gg$ than the sample's resistance serves partially regulate the current), the resistance of the sample and any leads inside of the voltage probe can have an effect on the current of the overall circuit. For metals, this correction is smaller than the noise in the measurement itself.

anvils together with a nonhydrostatic pressure medium), the area, A, could decrease faster than the length, l, could either decrease or increase. Though most likely l would be constrained, then the resistance of sample will increase. In the case of pressure-induced structural phase transitions, these are certain to be reflected in the resistance data; however, they may be difficult to distinguish from all other sorts of geometric changes. For example, when applying nonhydrostatic pressure, the area, A, of the sample may be reduced, causing the measured resistance of the sample, R, to increase.

To measure resistance under high pressures, an electrical four-point probe or quasi-four probe must be built to function inside the sample chamber of the DAC.

For a four-point measurement, four separate wires electrically contact the sample independently. Two of the wires are used to induce a current through the sample and the other two wires are used to measure the voltage across the sample. Generally, this is considered to be the standard method of measuring voltage across a sample. The two voltage leads contact only the sample. However, even a true four probe arrangement, as seen in Figure 2.10, does require the resistivity of the sample itself to be taken into account if a constant

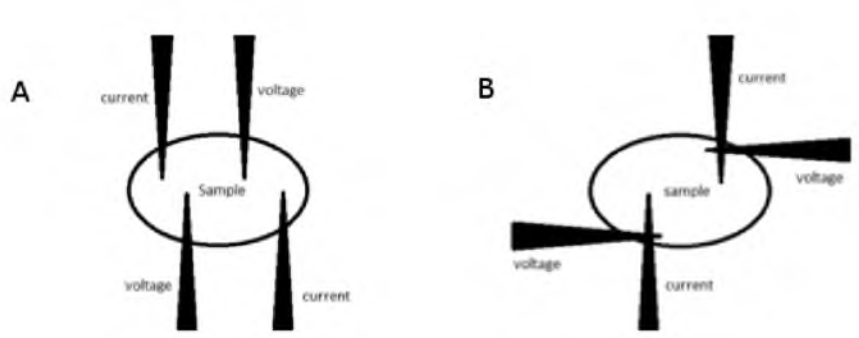

Figure 2.10. Methods for measuring the voltage drop, which can be related to resistance, across a sample. A) a cartoon of the 4-point probe arrangement. B) a cartoon of the quasi-4-point arrangement.

voltage source is used in the measurement. This is because the portion of the sample between the current leads and the voltage leads determines the amount of current flowing through the sample ($I = \frac{V}{R}$ where $R = R_{sample} + R_{leads}$). In the experimental setup, this effect is reduced by limiting the space between the current leads and voltage leads, and in the analysis by using equation 2.9.

Due to size constraints present in a DAC, especially when attempting to reach higher pressures by using smaller culets, the quasi-four probe is often advantageous. The quasi-four probe works according to the same principles as the four-point probe, the only difference is that each current lead touches one voltage lead (as seen in Figure 2.11). The greatest consequence of this configuration is that a portion of the signal now comes from the leads themselves. Several of the experiments in this dissertation have used resistance under high pressure to measure either solid to liquid transitions or superconducting transitions under pressure. The technique is naturally modified according to the needs of the experiment; here, the basic outline of the process will be explained, though each chapter with results also contains some explanation that is specific to those results.

To prepare a DAC for electrical resistivity measurements, first the DAC must be properly aligned and a gasket preindented and drilled. The gasket must then be electrically insulated. For these experiments, stycast BLU (2850 KT) epoxy is used to insulate the gasket. Inside the indented area of the gasket, alumina powder is pressurized to form a solid sheet. This acts as another layer of insulation as well as a pressure transmitting medium. A small hole is then poked in the center of the gasket chamber hole (which was filled with solid alumina); this is where the sample will be placed. Depending upon the material and the desired pressure range, other materials besides alumina may be used, such as NaCl or LiF for example.

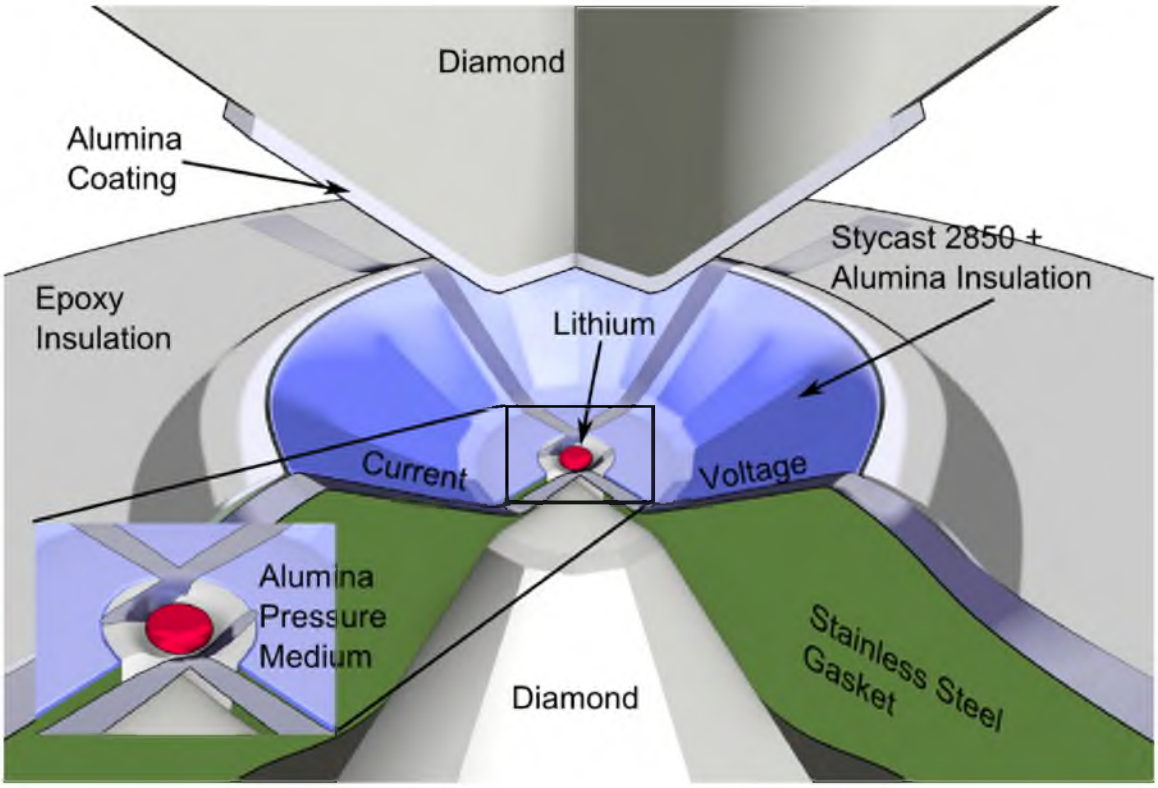

Figure 2.11. A cartoon of a typical electric probe built on a DAC. When size constraints allow, a four-point probe is built (culets of $\approx$ 350 - 500 μm); when smaller culets are used, a quasi-4-point probe is built. When building the quasi-4-point probe, all the leads are placed as close to the sample as possible to have a minimal signal from the leads. Figure by William B. Talmadge.

The electrical probe itself consists of Cu wires (typically $\sim$ 35 AWG) leading outside of the DAC (attached to wires eventually connecting to the Lock In Amplifier) and attached to smaller leads cut from very thin foil that eventually contact the sample. Pt is a good material for such leads; it cuts fairly cleanly allowing one to make very thin, sharp leads. However, at times other materials are desired such as Ni or Ta. The thin leads are glued to the gasket and arranged so that they will make a mechanical connection to the sample when under pressure. They are attached to the Cu leads by a mechanical connection, at times reenforced with nonsuperconducting silver epoxy. This method, of course, is altered, and often improved, with each experiment. Thus, Chapters 3, 4, 5, and 8 will discuss the particular method of building the electrical probe used for those particular data. Particular details of the method are described in section 4.3.

2.3.1 Resistance for Detecting Melting of Metals

Whilst the resistance of a metal becomes lower with the decrease of temperature, and this can be used to probe the sample quality, it is interesting to consider what happens with the increase in temperature. As the temperature and thus thermal energy is increased, the electrical resistivity of the metal increases as well, causing an increase in the measured resistance of the metal. This behaviour is intuitive, at least up to the melting point of the metal, at which point, the behaviour of the resistance of the solid and liquid metal becomes of interest.

At high temperatures, $T \geq \Theta_R$, the Gruneison-Bloch equation, 2.6, can be rewritten as:

$$\begin{aligned} \rho_i(T) &\approx \frac{C}{4M}\frac{T}{\Theta_R^2} \\ \rho_i(T) &\propto T \end{aligned} \tag{2.10}$$

At higher temperatures, the resistivity is roughly linearly as function of temperature. However, once the metal melts, the uniformity of the lattice is lost. Upon melting, the lattice ions become disordered, they are no longer arranged in a pattern that the electrons may 'flow' through with minimal impedance. The periodicity of the solid is lost and the Bloch Theorem no longer applies. Mott, [126], devised an empirical formula to describe the abrupt change in resistivity of a metal upon melting. He assumed that the lattice of a metal was regular up until the moment of melting at the melting temperature, T_m, and that each atom in the solid vibrated with the same frequency, ν_s. Using Einstein's model for specific heat, the characteristic temperature of the solid, Θ_s, is thus expressed as:

$$\Theta_s = \frac{h\nu_s}{k_B} \tag{2.11}$$

where h is Planck's constant, and k_B is Boltzmann's constant [126]. Assuming that the atoms in a liquid would have a different frequency, ν_l, and that the change in resistance upon melting is due to the change in ν_s or Θ_s to ν_l or Θ_l, and by setting the free energy of the liquid and the solid equal at T_m, we get the resultant empirical relation:

$$(\frac{\nu_l}{\nu_s})^2 = \frac{\rho_s}{\rho_l} = e^{\frac{80L}{T_m}} \tag{2.12}$$

in which L is the latent heat with the units of kilojoules per gram and the constant 80 has the inverse units. This relation agreed quite well with the measured results of the abrupt increase in resistivity upon melting of several metals [126, 27] and is shown in Figure 2.12.

2.3.2 Resistance for Detecting Superconductivity

As mentioned in Chapter 1 section 1.6, two main features of superconductors are zero DC electrical resistivity and the expulsion of magnetic fields. An electrical probe as described in section 2.3 is capable of detecting an abrupt drop in the electrical resistance, as seen in Figure 2.13. The frequencies used in all the resistance measurements presented in this work are low enough for the current to be considered effectively as DC (frequencies $\leq$ 15 Hz). Under pressure, however, the abrupt drop in resistivity may become a much broader transition. There is always a pressure gradient inside a DAC, and the sample always exists over a range of pressure. Especially in a region of a superconducting phase diagram where the slope of $\frac{dT_c}{dP}$ is steep, the transition as a function of measured temperature can become quite broad as shown in Figure 2.14. This can be due to the fact that one portion of the sample exists at a pressure at which the T_c is quite low or there is no superconductivity, and another portion of the sample may exist at the pressure at which the T_c could be quite high. This situation will lead to a drop in the resistivity that will begin at the highest T_c in the sample; however, since other portions of the sample have lower $T_c's$, the drop is broad as a function of temperature. The drop or transition continues to remain broad until the entire sample reaches a superconducting state.

Comparing the two Figures 2.13 and 2.14, we can see two views of different superconducting transition. In the case of $BaLi_4$, this transition is indeed more sharp and actually completes, the resistance flattens at the end of the transition, either at zero resistance or the resistance of the portion of the (Pt) leads which are part of the quasi-four probe arrangement. This is due to a few different factors, the most notable being that the change in T_c as a function of pressure is very shallow in the region at which these data were taken; also, this particular sample is a rather hard substance that is contained in a small region near the center of the culet. The transition of Figure 2.14, in a much smaller temperature

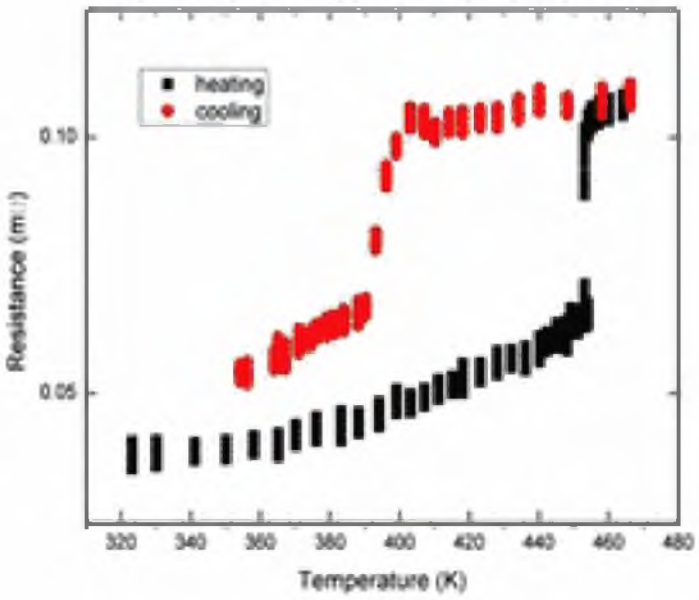

Figure 2.12. The melting transition of natural lithium measured by means of electrical resistance. The resistance was measured via a four-point probe. The lithium was kept inside of a argon-atmosphere cell to prevent reaction with moisture or air. Melting was confirmed both against the literature values for the melting temperature of lithium as well as confirmed visually (video of the sample was taken under a metallurical microscope during heating and cooling, the sample was large enough to confirm change of shape upon melting). The red curve shows the cooling of the sample and a significant hysteresis consistent with a first-order phase transition.

scale to illustrate the point, shows a much broader transition that continues until the entire sample superconducts. Likewise, there are a few explanations for this: the slope of $\frac{dT_c}{dP}$ is steep in this region of the superconducting phase diagram for this sample; also Li is very soft sample that is liable to spread considerably when pressurized, thus experiencing almost the maximal possible differences in compression across the pressure gradient.

There are different manners in which one may choose to define a T_c when faced with data in the form of the resistance as a function of temperature. Due to general broadening of the transitions under high pressure, in this work, we have typically chosen to look at the onset of the superconducting transition.

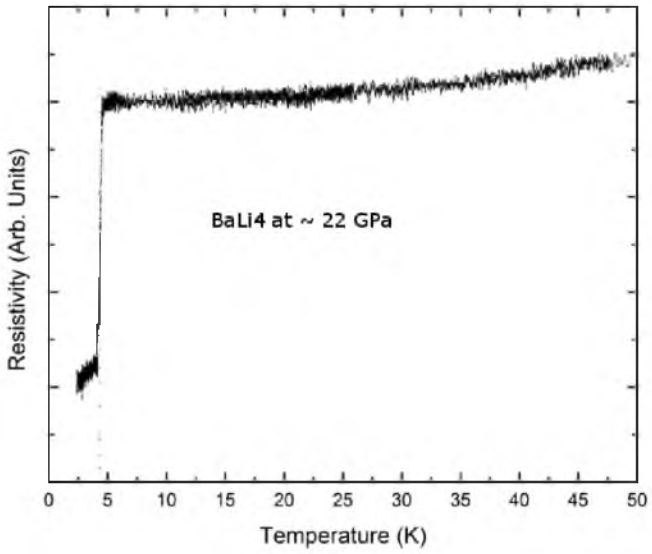

Figure 2.13. An example of a superconducting transition of $BaLi_4$ under pressure at $\sim$ 22 GPa (see Chapter 8). This transition is very sharp despite of the high pressure applied due to the moderate change of $\frac{dT_c}{dP}$ in this pressure region.

2.4 AC Magnetic Susceptibility

Another method to detect superconductivity is to measure the expulsion of the magnetic field within the sample, the Meissner-Ochsenfeld Effect. In order to detect this expulsion, coils are placed around the sample to detect the change in magnetic flux. The coil system typically used consists of four coils. They were made using an ACME coil winding machine. The pickup coil consists of 40 μm diameter wire wound in 4 layers of 30 turns each (total of 120 turns, with a height of $\sim$ 1.2 mm) with an inner diameter of 1.6 mm. The field coil is then wound on top of the pickup coil. The field coil also consists of 4 layers; however, it is typically one to two turns less per layer, since there must be room left at the ends of the coil for the pickup coil's wires. The field coil is 115 turns; however, when balancing, part of the last turn may be removed. The coil dimensions in this work were designed to fit the dimensions of a nonmagnetic DAC manufactured by D'Anvils (shown in Figure 2.15). The magnetic field of a coil (B in Telsa) is given by:

$$B = \frac{\mu_0 N a^2 I}{2(a^2 + z^2)^{\frac{3}{2}}} \tag{2.13}$$

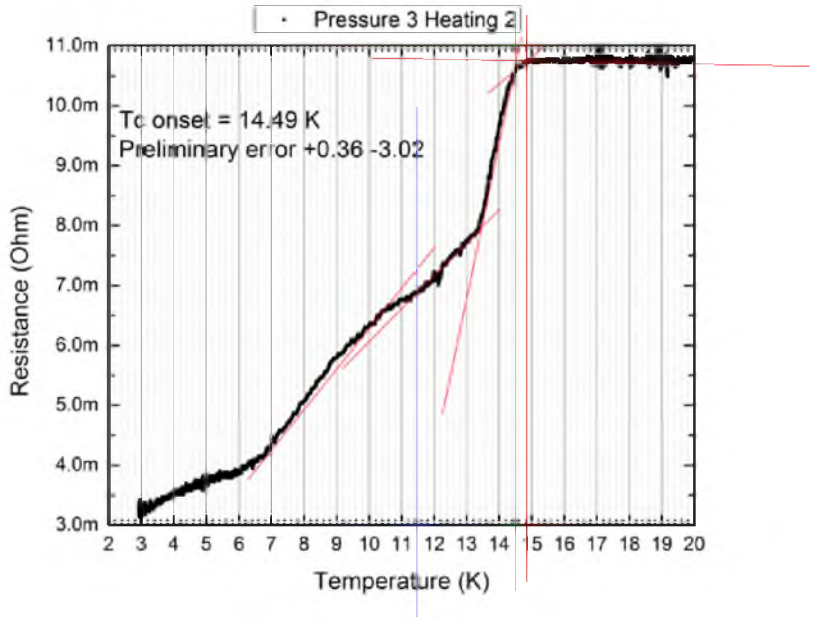

Figure 2.14. An example of a superconducting transition of Li at about 30 GPa. The transition here is very broad and does not actually complete all the way. The lines demonstrate the onset of the superconducting transition and the possible double transition.

where I is the current (in amperes A), N is the number of turns, μ_0 is the permeability of vacuum ($4\pi \times 10^7 \frac{N}{A^2}$), a is the radius of the coil (m) and z is the axial distance from the center of the coil (m).

The coils are connected such that the fields of the inner coils (the pickup coils) are opposite of each other (Figure 2.16). This is accomplished by connecting the two inside wires of each coil to each other and the outside wires of each coil will be used to measure the induced voltage of these coils. It is an important note for superconductivity measurements that no material with a T_c greater than the base temperature be used to connect the wires. Otherwise, this will give a signal that is unnecessary background. Given that most solders are composed of alloys of Sn, Pb, or In, solder generally superconducts near 6 to 8 K, which can mask the signal from the sample at approximately the same temperature. Silver solder or conducting epoxy can be used; however, if this creates a region of impedance with a different temperature dependence than the material of the remainder of the coil, then the background function can become much larger than is necessary. The method used in this work has been to spot weld the ends of the wires together. A circuit that produces a spark is used to induce a spark between the two ends of the wires; the wires are held together so

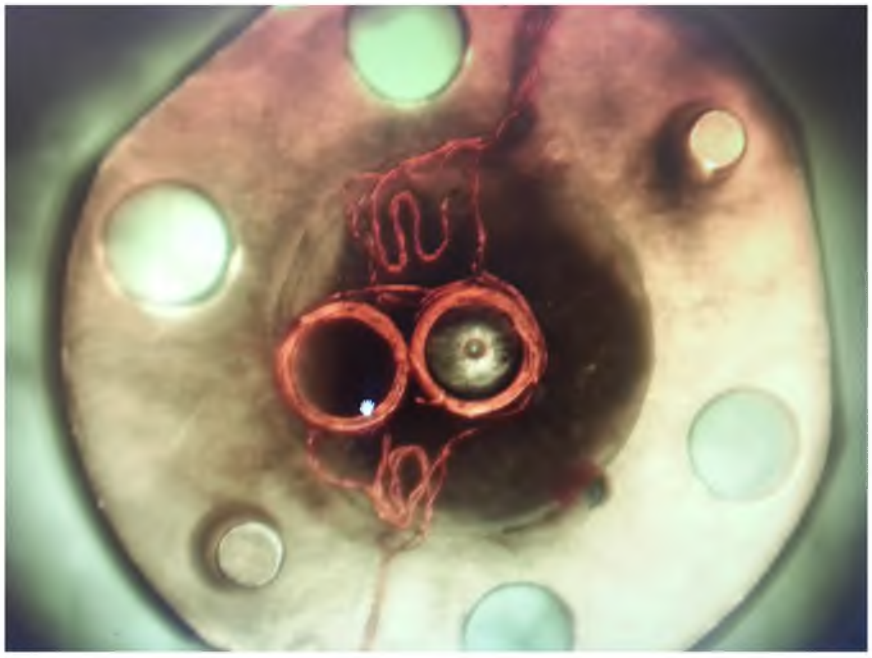

Figure 2.15. A typical set of coils placed on a D'Anvils nonmagnetic DAC.

that the spark partially melts the ends. The two melted ends of the wires can then fuse together and produce a connection which consists of the same material as the rest of the coil. The field coils are also connected via spot welding; however, they are connected so that the magnetic fields (induced by an applied current) of the field coils are in the same direction. The inside wire of one field coil is connected to the outside wire of the other field coil. This leaves one inside wire and one outside wire of the field coils, which were used to apply a current.

The field coils are connected to the function generator side of the Lock In Amplifier (Stanford Research model SR830) with a constant AC voltage source (in the kHz range) through a relatively high resistor (which is kept at constant room temperature) to produce a functionally constant current source. The temperature dependence of the resistivity of the coils themselves does affect the current flowing through the field coil. This in turn contributes to the temperature-dependent background of the signal. The current through the field coils induces a magnetic field inside the coils, where the pickup coils are located. This magnetic field change induces a voltage which is measured by the Lock In Amplifier.

When the magnetic field inside the pickup coils is altered, the measured voltage is affected. The pickup coils are balanced so the net voltage measured is zero. This makes the coil system sensitive to even very slight variations in the magnetic field. If the magnetic field

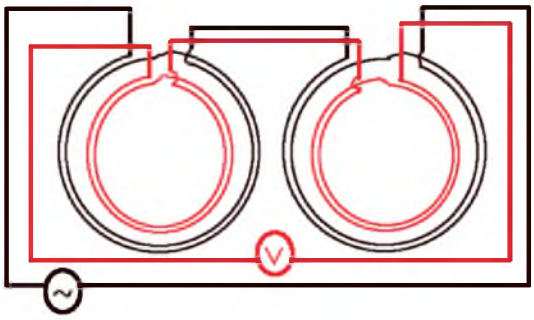

Figure 2.16. The wiring configuration of the coil system. The magnetic fields of the two field coils (in black) are in the same direction. The magnetic fields of the two pick-up coils (shown in red) are in opposite directions.

is altered, for example by a magnetic material placed inside the the coil, the voltage changes from zero (or near zero value). This method is very sensitive to the Meissner-Ochsenfeld effect (the repulsion of the magnetic field inside a superconductor at temperatures below T_c). As the superconductor ejects the magnetic field in its bulk, the voltage of the pickup coils is altered, shown in Figure 2.17. The intensity of the signal of the pickup coil (I measured in volts) is:

$$I = \frac{\pi f \alpha H V N}{R(1-D)}\chi \tag{2.14}$$

α is $\frac{1}{\sqrt{1+(\frac{L}{R})^2}}$, $2L$, R, and N are the length, radius, and number of turns of the coil, respectively. f is the frequency driving the field coil, and H is the magnitude of the applied magnetic field (produced by the field coil). V and D are the volume of the sample and the demagnetization factor (which depends upon the geometry of the sample). χ has the value -1 for a superconductor.

In high pressure experiments, the signal is complicated by the fact that the coil system must be placed inside of a DAC. For the experiments on the superconductivity of $BaLi_4$ (Chapter 8), the coil system was mounted on a thin insulating plate and placed with one pickup coil positioned with the diamond in the center (see Figure 2.15). In order to minimize the effects of the system being surrounded by metal, a DAC fashioned completely of nonmagnetic materials is used, in this case, a DAC manufactured by D'Anvils, made of a copper alloy. However, even with nonmagnetic materials, the body of the DAC will still produce some background from eddy currents [73]. Another complication is that the gasket in this configuration sits inside the pickup coil, meaning that this also contributes to the background signal. Nonmagnetic materials are preferable for gasket material, such

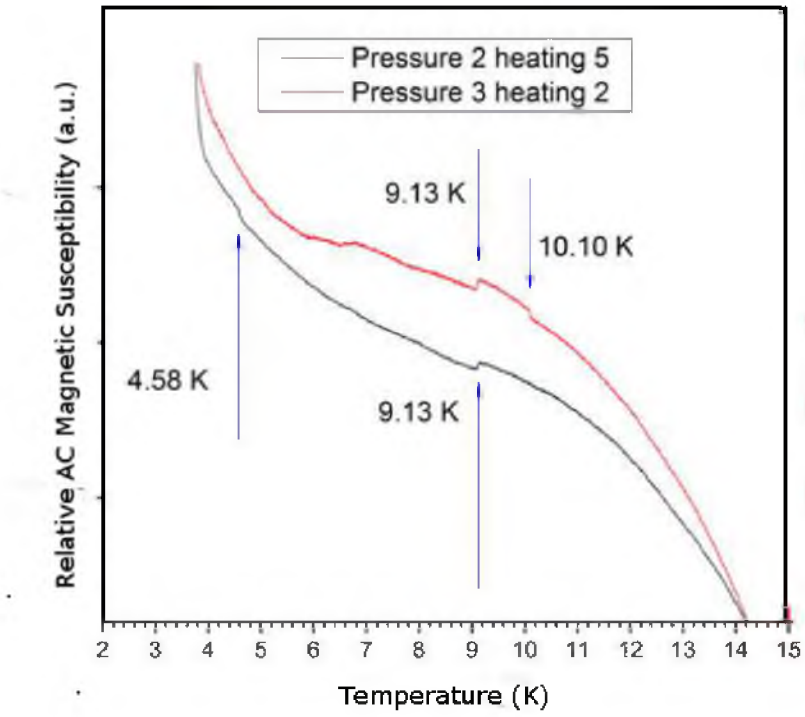

Figure 2.17. AC magnetic susceptibility signals of Li at 18 and 25 GPa (Pressures 2 and 3, respectively). A sample of Nb of comparable size to the sample was placed in the compensating coil, creating a signal of roughly equal magnitude, yet opposite direction, of the signal of the sample under pressure. The x-axis shows the temperature and the y-axis is the amplitude of the magnetic susceptibility signal; here, the raw measured voltage is shown. The arrows show the superconducting transitions.

as CuBe. However, the gasket must also be a strong enough material to withstand the deformation from the diamonds at high pressures. In the experiments described in Chapter 8, Re gaskets were used. The disadvantage to Re is not only the larger background signal, but also the compressed Re (from the indented area of the culet, around the sample chamber) superconducts near 4 K. The gasket is cut to fit the diameter of the pickup coil (in this case 1.6 mm); however, in the case of a 300 μm diameter culet, the sample chamber is only $\approx$150 μm in diameter. The result is that, at best, the area of the sample is an order a magnitude smaller than the gasket. Considering also the thickness of the gasket (250 μm outside of the indented area, and $\approx$ 50 to 70 μm in the area indented by the culet, and decreasing with increasing pressure), the volume of gasket is at least two orders of magnitude greater than the sample. This means that once the gasket superconducts, there is no possible means

of detecting superconductivity in the sample. Any measurements with a Re gasket are therefore limited to temperatures above 4 K.

2.5 de Haas van Alphen Effect

The de Haas van Alphen effect is the oscillation of diamagnetic susceptibility as a function of changing magnetic field, shown in Figure 2.18. At sufficiently low temperatures and high enough magnetic field, the magnetization of metal is affected by the increase or decrease in the applied magnetic field [38]. The frequency of these oscillations provides information regarding the size of the extremal area of the Fermi surface through the Onsager relation [91]:

$$\frac{1}{\Delta B} = \frac{1}{F} = \frac{2\pi e}{\hbar S} \Longrightarrow F = \frac{\hbar}{2\pi e} S \tag{2.15}$$

where S is the extremal area of the Fermi surface, m^{-2}, e is the elementary charge, C, and $\hbar$ is Planck's constant, Js. This gives the frequency of the quantum oscillations, F, the somewhat unusual units of T. These oscillations occur as the Landau levels [66]:

$$\hbar\omega_c = \frac{e\hbar B}{m^* c} \tag{2.16}$$

expand past the Fermi level with the change in magnetic field B (m^* is the effective mass of the electron). As the magnetic field is increased (or decreased) the magnetic moment of the sample responds to the change in field. As the Landau levels expand in the increasing field (or contract in a decreasing field) and pass the Fermi level, the magnetic moment of the sample oscillates. This quantum oscillation of the sample can be recorded as a function of the magnetic field and then related to extremal cross-sectional area of the Fermi surface through the Onsager relation 2.15.

2.5.1 Torque Magnetometry

All magnetic measurements referred to in Chapter 7 were made at the National High Magnetic Field Laboratory in Tallahassee, FL by means of torque magnetometry. This method measures the torque created by a transverse magnetic field:

$$\vec{\tau} = \vec{M} \times \vec{B} \tag{2.17}$$

where $\vec{M}$ is the magnetic moment and $\vec{B}$ is the magnetic field. Commercially available piezoresistive cantilevers were used to measure the quantum oscillations of lithium isotopes (Chapter 7) through the de Haas van Alphen effect. The samples are placed on the cantilever and when the sample experiences torque, $\vec{\tau}$, from the applied magnetic field sweep, the

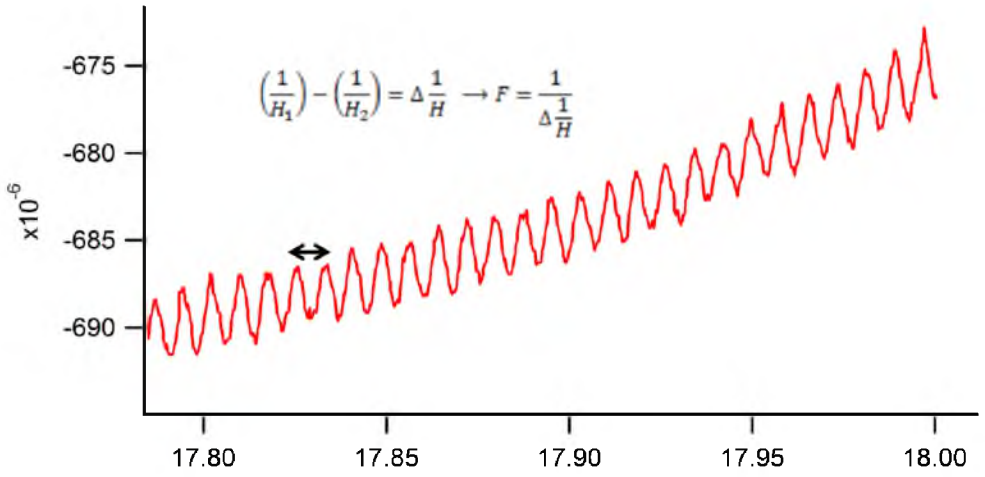

Figure 2.18. An example of quantum oscillations in lithium with natural isotopic composition. The x-axis is the magnetic field in Telsa and the y-axis is the intensity of the signal (measured in voltage from the torque magnetometry). The frequency of the change in the inverse field, shown as F in the figure, can be related to Fermi surface.

deflection of the cantilever produces a resistance which is then measured. The cantilever platform has two arms, which are balanced to have nearly equal electrical resistance. The sample is placed on one arm and the other is empty as a reference; the setup is shown in Figure 2.19 adapted from [64].

The sample is placed on the tip of the cantilever secured in Apiezon N grease (a silicon-free lubricant generally used in cryogenics), connected to a Lock In Amplifier as well as rotator. The sample is then cooled to mK temperatures as described in section 2.2.1.1; the subsequent freezing of the grease secures the sample on the cantilever. As the magnetic field is swept ($|\vec{B}|$ either increasing or decreasing), the magnetization of the sample ($\vec{M}$) applies a torque ($\vec{\tau}$)to the cantilever per equation 2.17, which is in turn measured in terms of voltage via a Lock In Amplifier.

Chapter 7 contains more details regarding the applications of this method for lithium isotopes.

2.6 Diffraction

2.6.1 X-Ray Diffraction

X-ray diffraction (XRD) is a powerful method used in the characterization of solids. The technique has been used for several purposes in the present work: in Chapter 6, XRD was

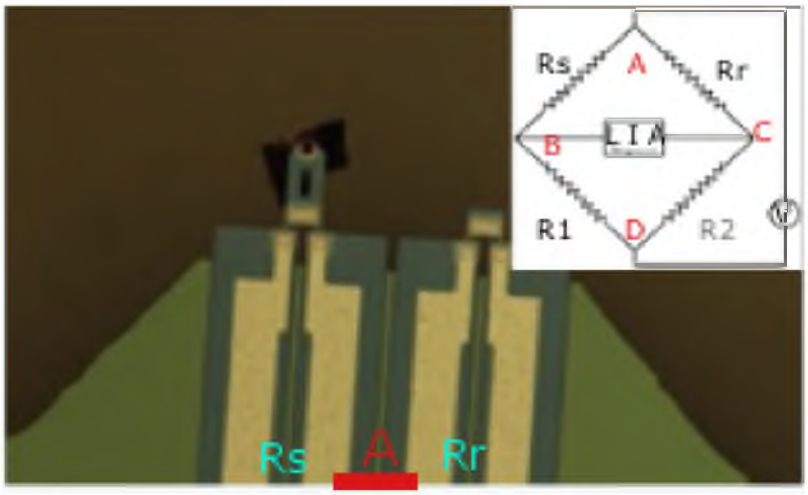

Figure 2.19. A Wheatstone bridge circuit for measuring quantum oscillations by means of a piezoresistive cantilever. R1 and R2 represent two outside dedicated boxes. The resistances of the cantilever arms, Rs is the arm that holds the sample, and Rr is the reference arm, are shorted together at point A. AC voltage is applied from points B to C, and the voltage across points A and B is measured with a Lock In Amplifier (LIA in the figure). This figure is adapted from [64].

used to identify high pressure, low temperature phases of lithium; in Chapter 7, it was used to determine the quality of the single crystals; finally in Chapter 8, it was used to identify the intermetallic compound synthesized.

X-rays are a form of electro-magnetic radiation that are very well suited for investigation into the structures of crystals, as the wavelength of X-rays is comparable to the interatomic distances of solids. Scattered radiation occurs when the electric field of the incident X-ray interacts with the electrons of an atom. Following classical theory, an accelerated charged radiates, the electron-cloud of the atom acting as the origin. The radiation has the same frequency as the incident beam and the intensity is represented in Figure 2.20 and can be expressed with the Thomson scattering equation.

$$\frac{I}{I_0} = \frac{e^4}{m^2 c^4 r^2} \left(\frac{1}{4\pi\epsilon_0}\right)^2 \left(\frac{1+cos^2(2\theta)}{2}\right) \tag{2.18}$$

where e is the charge of the electron, m is the mass of the electron, c is the speed of light in a vacuum, r is the distance from the electron to the detector, and θ is the scattering angle. When 2θ is perfectly 90 degrees, the beam can be completely polarized (polarization factor $P = \frac{1+cos^2(2\theta)}{2}$), since the index of refraction (n) of X-rays in most materials is 1. Whilst this intensity is very small, the typical number of electrons in even μg samples is large

enough to be quite detectable. Since the scattering is from the interaction of the beam with the electrons of the solid, the intensity is affected by the number of electrons surrounding the atom. This can be expressed in terms of the atomic form factor:

$$f_n = \int d^3 r \rho(r) e^{-iG \cdot r} \tag{2.19}$$

From this equation, we can go on to define the Structure factor:

$$S_G = \sum_n f_n e^{-iG \cdot r} \tag{2.20}$$

Assuming the electron density ($\rho(r)$) is spherically symmetric about the origin, and at $r = 0$, the integral can be written to express the number of electrons in the unit cell proportional to atomic number Z.

$$Z = 4\pi \int dr \rho(r) r^2 = f_n \tag{2.21}$$

The optimal signal is at small values of $\frac{sin(\theta)}{\lambda}$ where the structure factor reduces to Z:

$$\text{structure factor} \rightarrow \text{atomic number} \tag{2.22}$$

The signal obtainable from X-rays interacting with a crystal is proportional to the structure factor, thus proportional to the atomic number, Z. This factor causes an issue for low Z elements, such as lithium. With few electrons, the structure factor of low Z elements is proportionally low, making them very weak scatterers. In order to compensate for the weak scattering factor, higher flux or brightness of X-rays and generally longer exposure times are necessary for experiments investigating materials such as lithium. For the work on the martensitic transformation of lithium (Chapter 6, [151]), a synchrotron source was necessary to acquire the X-ray diffraction data.

Diffraction of X-rays through a solid is the same mechanism as other forms of diffraction (see Figure 2.21): this occurs when light encounters obstacles or slits that are of a comparable size to the wavelength of the light. This is one of the main features of X-rays that makes them so useful for the study of crystals: the wavelength of X-rays is in the range of interatomic spacings of crystals (≈Å). The recorded diffraction pattern shows the regions of constructive interference, where the light waves have interfered in phase with one another. This diffraction does require that the solid be crystalline (periodic). This condition for diffraction can be formulated by Bragg's Law:

$$2dsin(\theta) = n\lambda \tag{2.23}$$

where θ is the angle between the incident X-ray beam and the face of the crystal (see Figure 2.22), n is an integer (values of n greater than one were not visible in any of the present

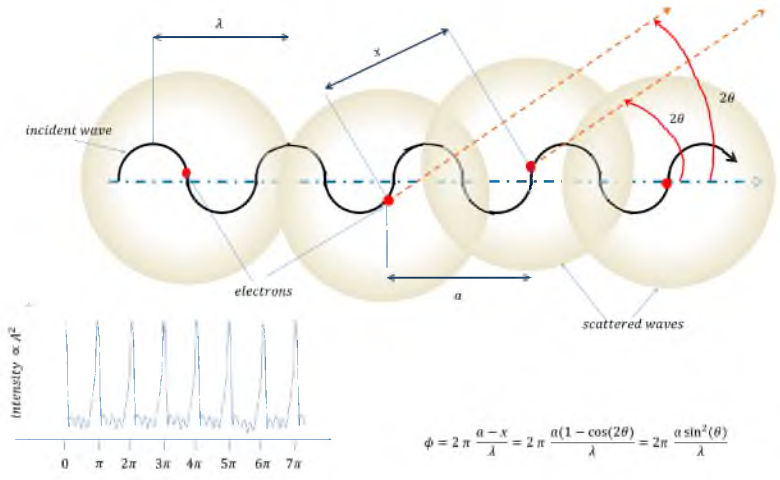

Figure 2.20. Example of Thomson scattering. The concept of this figure was inspired by Pecharsky et al. [139]. This shows a two-dimensional cartoon of the concept behind Thomson Scattering.

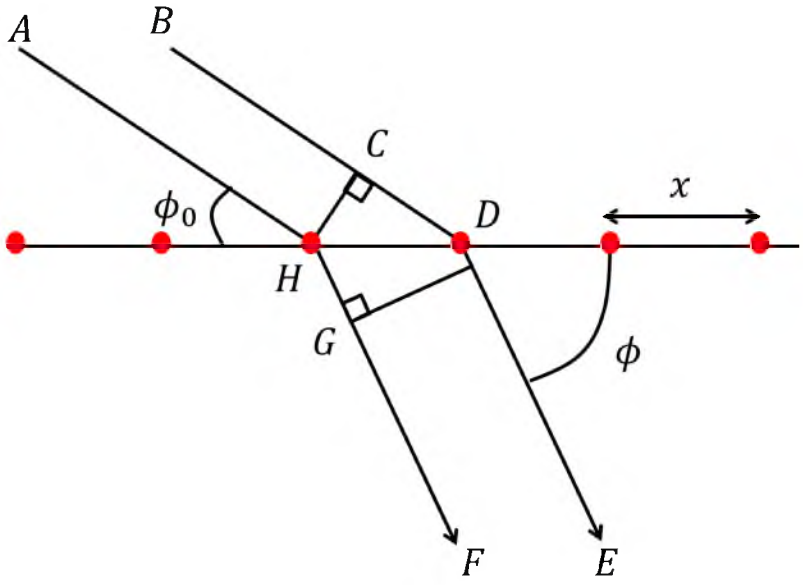

Figure 2.21. An example of simple diffraction of light by a grating. Constructive interference only occurs at the condition CD-HG = nλ (λ is the wavelength of the light). This idea for this schematic comes from chemwiki.ucdavis.edu.

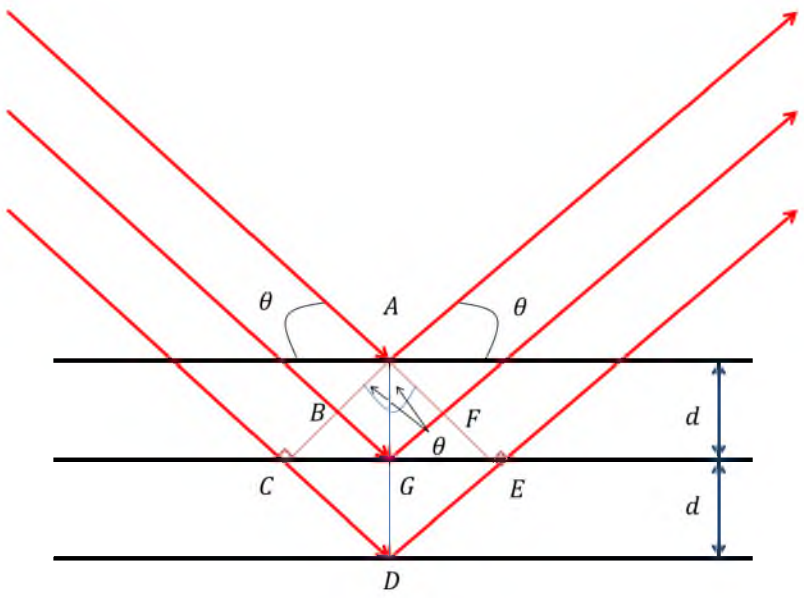

Figure 2.22. An example of simple Bragg's law. The concept of this figure comes from chemwiki.ucdavis.edu.

work), d is the spacing between the planes, and λ is the wavelength. By utilizing Bragg's law, one can determine the values of d by applying simple geometry to the recorded pattern (wavelength and distance of the sample to the detector naturally must be known). It is from determining the values of the d-spacing that the crystal structures can be identified.

2.6.2 Neutron Diffraction

Neutron diffraction works according to the same fundamental properties as X-ray diffraction. The main difference between the two techniques is a consequence of the differences between electro-magnetic waves and neutron beams. The most notable change is that the scattering power of a material is not proportional to Z, since neutrons are neutral particles, thus they do not interact with the electron-cloud, but instead interact with the core nuclei.

As with X-rays, the wavelength of neutrons used for diffraction experiments is near 1 Å, in the range of thermal neutrons. At the instrument in SNAP, ORNL, the neutron beam can be focused by means of a parabolic guide into a hexagonal boron-nitride tubing, which prevents scattering from the air from reaching the detectors [71].

The scattering factor of neutrons is not related to atomic number, meaning that in principle, low Z materials are not discounted due to low scattering. Also, there are negative scattering lengths in neutron diffraction. A positive scattering length, b, corresponding to

a repulsive Fermi pseudo-potential ($V(r) = \frac{2\pi\hbar^2}{m} b\delta(r)$, b is the scattering length, and $\delta(r)$ is the Dirac Delta function, $r = 0$ is the centre of mass of the nucleus) and a negative scattering length corresponds to an attractive Fermi pseudo-potential [24]. For thermal neutrons, a positive scattering length results in a negative phase shift, whilst a negative scattering length results in a positive phase shift. This means that alloys can be formed which have effectively zero scattering. This can be used to the experimenter's advantage to create a sample chamber which does not contribute to the background.

As with XRD, the goal is to determine the d-spacing between the lattice planes:

$$\begin{aligned} 2dsin(\theta) &= \lambda \\ d &= \frac{\lambda}{2sin(\theta)} \end{aligned} \tag{2.24}$$

for the neutron experiments described in Chapter 6, experiments were carried out at the Spallation Neutron Source in Oak Ridge National Laboratory using the time of flight technique. This technique uses a chopper to produce a pulses of neutrons and the arrival time of neutrons of the diffracted neutrons onto the detector is recorded to determine the d-spacing.

$$d = \frac{\lambda}{2sin(\theta)} = \frac{h}{mv}\frac{1}{2sin(\theta)} = \frac{ht}{2mLsin(\theta)} \tag{2.25}$$

First, we put λ in terms of Planck's constant, the mass and velocity of the neutron; we then put the velocity of the neutron in terms of distance from the sample to the detector (L) and the time of flight (t) of the neutron from the moment of diffraction to interacting with the detector. Determining the time of flight and the angle, when the remainder of the parameters are known through calibration, allows for solving the d-spacing.

2.6.3 Analysis

The data from diffraction experiments are typically recorded as an image. This image can be converted in a spectrum of peaks plotted versus 2θ or d-spacing (see Chapter 6); these data represent powder data (a collection of randomly oriented crystals, as opposed to a single crystal) that were collected by neutron and X-ray diffraction. This mapping to a spectrum requires knowledge of the position of the sample in relation to the detector as well as knowledge of the wavelength of the X-rays or neutrons. The profile of these peaks can be fit to a variety of different functions to describe the position and shape; the intensity and sharpness of the peaks can contain information regarding the strain the sample undergoes. In the work described in Chapter 6, the diffraction sets were refined with fits to Gaussian peaks in Origin Pro or GSAS. In this case, whilst the peaks remained sharp up to 6 GPa, there were clearly effects of strain upon the broadness of the peaks as well as

texture affecting the intensities of the peaks. For this reason, the intensities of the peaks were not taken into account for the refinement of spectra (Rietveld method); instead, only the positions of the peaks as a function of d-spacing or 2θ were considered (LeBail Method).

The d-spacing represents the distance between the lattice planes and can be related to the lattice parameters of the crystal by determining the Miller indices (h,k,l), and identifying the symmetry. The relation of the d-spacing to the lattice parameters depends upon the particular symmetry of the lattice. The highest symmetry, four-fold, cubic symmetry has the simplest relation to lattice parameter a:

$$\begin{aligned} d^2(h^2+k^2+l^2) &= a^2 \\ d &= \frac{a}{\sqrt{h^2+k^2+l^2}} \end{aligned} \tag{2.26}$$

The cubic symmetry is simple enough that it can be indexed without the aid of powerful computer programs; in essence, it can be indexed by hand. Once the d-spacing has been determined for the refined peaks, the peaks positions can be listed in terms of $\frac{1}{d^2}$:

$$\frac{1}{d^2} = (h^2+k^2+l^2)\frac{1}{a^2} \tag{2.27}$$

it is then convenient to divide all these terms by the minimum value. The resultant values in turn can be rounded to the nearest integer value and related to the value of $h^2+k^2+l^2$; which values appear allow for identification of which type of cubic phase is present (body centered, face centered, or primitive) [139]. This method makes it very easy to identify cubic phases since only cubic symmetries will produce a column ($\frac{d^2_{min}}{d^2}$) with near integer values; other symmetries, of course, have different relations between the d-spacing and the lattice parameters.

For the work in Chapter 6 ([151]) identifying phases of lithium, all three of the phases had been previously characterized [14, 13, 74, 75, 166]; using the information published in the Inorganic Crystal Structure Database (ICSD), the expected positions of peaks are known (and can be calculated for different pressures using knowledge of the equation of state) and can be plotted with the recorded spectrum. This allowed us to identify two cubic phases of lithium, bcc and fcc, and the low temperature hR3 phase (with hexagonal symmetry $\frac{1}{d^2} = \frac{4}{3}\frac{h^2+hk+k^2}{a^2} + \frac{l^2}{c^2}$).

For the work described in Chapter 8, X-ray diffraction was used to identified the compound that was synthesized for the experiment ($BaLi_4$). For this work, the XRD data set was used in much the same manner as a fingerprint. The collected peaks were plotted with the expected pattern of $BaLi_4$ as well as other intermetallics consisting of Ba and Li

(such as $Ba_{19}Li_{44}$) as well as Ba and Li alone. The data matched the expected values of $BaLi_4$ only; thus, the sample was identified as that compound.

CHAPTER 3

HIGH PRESSURE MELTING OF LITHIUM

Lithium, as the lightest metal at ambient pressure, presents as a promising candidate for quantum solidity. One pathway by which to investigate this possibility is the study of its melting curve as function of pressure. As mentioned in section 1.1, other alkali metals (Na, K, Rb) all display a maximum in their melting curves [65, 110, 130]. Whilst generally this can be attributed to structural phase transition to lower symmetry phases, the results presented in [70] show a maximum near 10 GPa, where it was previously reported, and a minimum near 50 GPa of ≈ 200 K attributed to quantum effects, cold melting. The work in this chapter was carried out to investigate the claim of cold melting further, to find evidence of quantum melting (see section 1.5.1).

S. Deemyad contributed the original concept of this experiment. The experiments and analysis were carried out by A.M. Schaeffer (Richards) and S.R. Temple; W.B. Talmadge implemented the data collection software. The laser heating and pyrometry design was from [41]; the resistance measurements were modified from [73] and from M. Debessai and T. Matsuoka. All experiments were carried out in the Deemyad Laboratory at the University of Utah. The manuscript was written by S. Deemyad and A.M. Schaeffer, with input from W.B. Talmadge and S.R. Temple.

Reprinted with permission from Physical Review Letters, Deemyad, S., Talmadge, W.B., and Temple, S.R. 2012. High Pressure Melting of Lithium, *Physical Review Letters*, 109, 185702. Minor changes to the text and figures were requested by the committee members and University of Utah Thesis Office.

3.1 Abstract

The melting curve of lithium between ambient pressure and 64 GPa is measured by detection of an abrupt change in its electrical resistivity at melting and by visual observation. Here, we have used a quasi-four-point resistance measurement in a diamond anvil cell and measured the resistance of lithium as it goes through melting. The resistivity near

melting exhibits a well documented sharp increase which allowed us to pinpoint the melting transition from ambient pressure to 64 GPa. Our data show that lithium melts clearly above 300 K in all pressure regions and its melting behavior adheres to the classical model. Moreover, we observed an abrupt increase in the slope of the melting curve around 10 GPa. The onset of this increase fits well to the linear extrapolation of the lower temperature bcc - fcc phase boundary.

3.2 Introduction

At ambient pressure, lithium is the lightest metallic element and the prototype of a simple metal, with a nearly spherical Fermi surface. The structural and electronic properties of lithium at high densities are highly counterintuitive [119, 160, 172, 42, 177], and under high pressure, lithium undergoes a series of symmetry-breaking structural phase transitions [70, 75]. The properties of lithium under pressure have attracted considerable attention, especially because of its possible analogy to metallic hydrogen and considerable quantum solid behavior (e.g., [132, 100, 63, 62, 55, 146, 170, 105]). Despite a broad interest, the high pressure properties of lithium above 200 K are poorly studied. This is due to technical challenges caused by the reactivity, at high pressure and temperature, of lithium with diamond, which is the building block of static high pressure diamond anvil cells (DACs). Recent structural studies on lithium in a diamond anvil cell used X-ray diffraction to characterize the region between 77 K and room temperature at pressures up to 120 GPa [70].

The study found that the diffraction lines had disappeared in the region between 40 to 60 GPa at temperatures as low as 190 K, which can be indicative of melting. This study, together with earlier high pressure melting measurements up to 15 GPa, using differential thermal analysis (DTA) in a multianvil cell [70, 100, 110, 16], suggests a very sharp drop in the melting line between 15 to 40 GPa. Lithium's structure changes from fcc to lower symmetry structures in the region around 40 GPa, which according to recent molecular dynamic calculations is followed by a sharp decrease in the melting temperature to 280 K at about 60 GPa [173]. The drop in the melting temperature of lithium suggested by X-ray studies is in qualitative agreement with the molecular dynamics calculations. However, above 40 GPa, melting was observed at much lower temperatures than predicted, which has been attributed to quantum effects caused by large lattice dynamics of lithium. No prior experiments before our study have observed this drop in the melting temperature directly, and in the pressure range between 15 to 40 GPa no experimental data have been available

[110, 16, 98].

3.3 Methods

Several methods have been employed to determine melting temperature at high pressure. These include differential thermal analysis, a technique suitable for larger volume pressure cells, as well as latent heat measurements, laser reflection, X-ray diffraction, discontinuity in the physical properties of the material, and visual observation of melting and crystallization [16, 41, 19].

Determination of the onset of melting at high pressure in a diamond anvil cell, in which the sample size is small, can be very challenging. In the particular case of lithium, which is highly reactive with diamonds at high pressures and temperatures, all previous diamond anvil cell experiments were conducted in cryostats. Those experiments conducted above room temperature were done in large volume, relatively low pressure cells. In this study, for the first time we unified these two pressure and temperature ranges with a single method.

We attempted four different methods of determining the onset of melting: observation of the laser speckle pattern with simultaneous latent heat measurement, direct visual observation, and electrical resistance measurement. Of these, only the latter two methods were successful.

The low melting temperature of lithium made remote temperature sensing by blackbody radiation impractical. Successful blackbody measurements are crucial to both speckle motion and latent heat methods. (Some surface effects were observed during laser heating which are explained later in this chapter in section 3.7.) To collect the data presented here, we used two complementary methods. First, we used direct visual observation of the melting of lithium in an argon pressure medium below 35 GPa. Direct observation of the melting requires a relatively soft pressure medium. As lithium melts, its shape changes to minimize surface area. Determining the onset of melting visually, with a small sample, in a solid pressure medium, is difficult and susceptible to large errors. Therefore, to confirm these visual data, we used a quasi-four-probe resistance measurement to detect the abrupt jump in electrical resistivity as the sample melts across the entire pressure range studied. The abrupt jump in the electrical resistivity of normal metals at melting has been known for a long time [126, 27]. Recently, this effect has been used in a novel design to determine the melting of Au and tin in a diamond anvil cell up to 21 and 45 GPa, respectively [188, 187]. However, in these measurements the circuit was optimized for reaching very high temperatures by resistive heating of a thin film of sample in situ, and the jump in the resistivity of the sample was a 5 % effect. Using the same principle in our measurement, we

used a conventional quasi-four-probe resistivity circuit that allows determination of the jump in resistivity with much higher sensitivity (Figure 3.1). Detection of melting by the abrupt jump in resistivity relies upon the characteristics of the melting transition rather than upon the differences between solid and liquid phases, and so it very precisely detects the onset of melting while preventing confusion with, e.g., an amorphous phase [126, 27, 50, 148, 94]. The resistivity method is a tabletop experiment providing a very clear and sharp signal which is reproducible. In his paper, Mott has shown that the resistivity of normal metals just below and above their melting point approximately follows the relation (equation 2.12):

$$\frac{\rho_l}{\rho_s} = e^{\frac{80L}{T_m}} \tag{3.1}$$

in which ρ_l and ρ_s are resistivity of a metal in liquid and solid phase at the melting temperature respectively, L is latent heat of fusion with the units kilojoules per gram atom, and T_m is the melting temperature in kelvin. The presence of a solid pressure medium allows confinement of the sample to prevent it from flowing away from the leads upon melting.

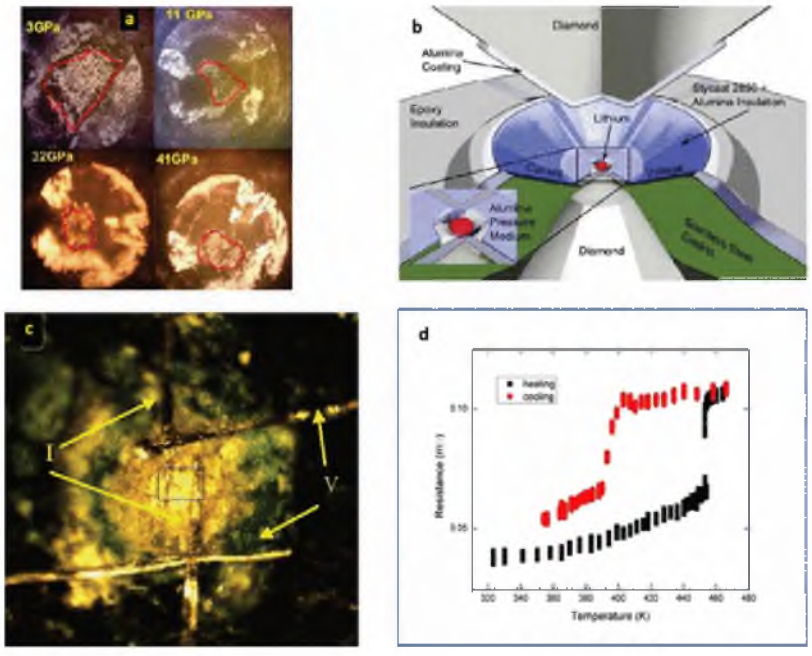

Figure 3.1. Aspects of melting lithium under pressure. a) Micrographs of sample in reflected light. Red dotted lines represent the contour of the sample. Dark spots are regions of sample or electrodes deformed under pressure and are shiny if viewed from a different angle. b) Schematic drawing of the quasi-four-probe resistance. c) The arrangement of electrodes prior to loading the lithium sample. The square region marks the approximate area of the sample in the measurement. d) Large hysteresis between melting and recrystallization temperatures of a lithium sample at ambient pressure due to rapid cooling.

This method also allows the observation of mixed solid phases and crossing of the solid-solid phase boundary in regions where structural phase transitions occur (Figure 3.2). Also, this method allows estimation of the latent heat of metals at high pressure. In the presence of a solid pressure medium, which serves to confine the sample to roughly the same shape, the measured jump in resistance would be sufficient to empirically estimate the latent heat of fusion based on Mott's equation. One notable drawback to this method is that it is limited to metals. In this Letter, we present an extensive determination of the high pressure melting of lithium to 64 GPa. A sample of lithium was loaded directly onto the leads inside an argon glove box. To prevent reaction of the diamonds with the sample, a layer of alumina (Al_2O_3 or LiF) of approximately 10 μm thickness was baked onto the diamond culets, and alumina or LiF nanopowder was used as a pressure medium. Proper baking time was necessary to remove the moisture prior to loading the lithium. No epoxy was used in the vicinity of the lithium. An insulated stainless steel gasket with a 150 μm hole was used in all cases. The sample was 99.9 percent pure lithium with a natural isotopic makeup (Sigma Aldrich 266000). The dimensions of the sample were approximately 50 to 100 μm in diameter by 10 to 20 μm thick, but varied between pressure runs. This variability, and the difficulty of determining precise sample size in situ, precluded measurement of the absolute resistivity of the sample; the discrete change in resistivity indicative of melting is not impacted by sample size. Pressure was calculated before and after melting by ruby scale. To enhance the signal quality and reduce the resistive heating of the sample, ac resistance measurements were

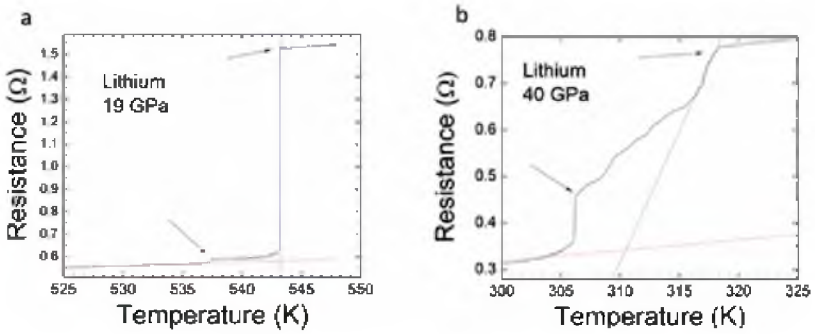

Figure 3.2. Jump in resistivity at a) 19 GPa, well within the boundaries of the fcc phase, and b) 40 GPa, which is at the boundary of fcc and CI16. The broadening of the melting signal in the latter was reproducible, indicating the existence of mixed solid phases. The higher temperature arrow defines the completion of the melting transition and the lower temperature arrow gives the lower limit of melting. The resistances are estimated after subtraction of the lead contribution and would approximate $L_{40\mathrm{GPa}} \approx 3$ kJ per mol. and $L_{19\mathrm{GPa}} \approx 5$ kJ per mol., using Mott's equation.

done using a small current $I_{rms} \approx 100$ μA. We measured resistance with a quasifour-probe system using Ta and Pt as electrodes and the data were collected by a lock-in amplifier (Figure 3.1 b).

The resistivity of the combined solid electrode-lithium voltage path was on the order of 10^{-7} Ωm at room temperature, with a temperature coefficient on the order of $\approx 10^{-3}$ $\frac{\Omega m}{K}$. These values were pressure dependent and also dependent on the relative dimensions of the lithium sample and the electrodes. By measurements of the relative size of the sample, including the leads in each pressure point, and comparison of our data to the theory of melting in metals, some very crude numerical estimates of the latent heat of lithium and temperature dependence of its resistivity are possible. These estimates would give a rough value of jump in resistance of lithium of about 2 times on all transitions.

3.4 Experiment

Temperature was increased isobarically for each data point. The results from both of these methods, in the region they overlap, are consistent within the error (Figure 3.3). The temperature of the whole DAC was controlled in two ways. Near room temperature, a homemade ceramic oven resistively heated the DAC and was initially precooled with a dry ice bath. The DAC was heated at a rate slow enough to avoid thermocouple delay (≈ 0.5 $\frac{K}{min}$). Between 77 and 325 K, the DAC was cooled with liquid nitrogen in a cryostat and data collected during passive warming (<0.2 $\frac{K}{min}$). The temperature in both cases was recorded on the gasket surface. One of the problems in high pressure and temperature studies of lithium is its high chemical reactivity. Lithium reacts with diamond at elevated pressures, which leads to failure of the experiment and the diamonds. Several methods have been employed to minimize this reactivity, including limiting the studies to lower temperatures typically below 200 K. This would not be suitable for completing the phase diagram from 15 to 30 GPa based on previous studies [70, 110, 98]. Lithium can flow through small cracks at high pressure, and a sufficiently thick layer of nonreactive pressure medium is required to protect the diamonds and preserve sample purity. To maintain the purity of the lithium sample in our experiments, we separated the lithium from both diamond anvils by nonreactive pressure transmitting media. In the two different parts of this study, by visual observation and electrical resistivity, argon, alumina, and LiF were used as pressure transmitting media. LiF is nonreactive with lithium. At ambient pressure, argon and alumina do not react with lithium to the highest temperatures of this study (<600 K). We excluded the possibility of any reaction between alumina, argon, and LiF at high pressure

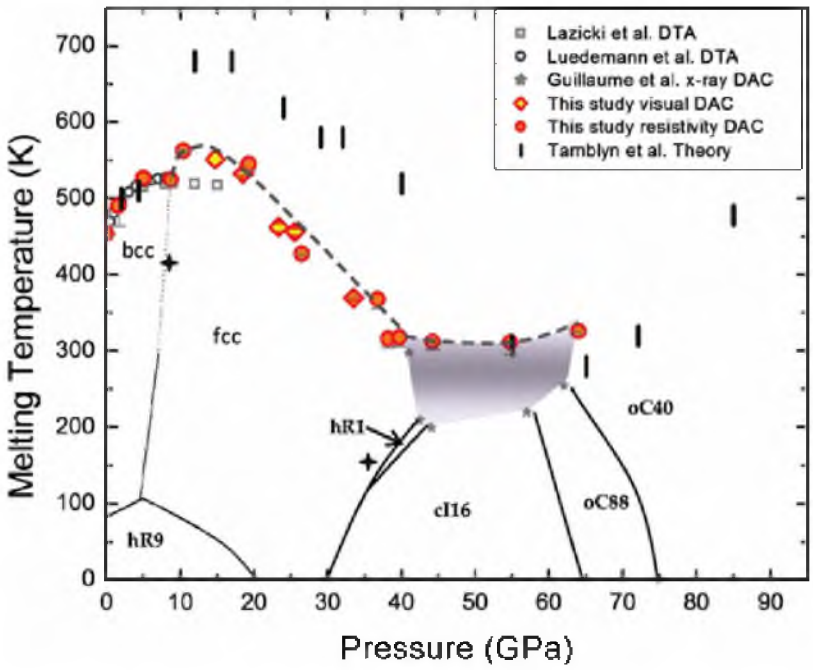

Figure 3.3. The melting curve of lithium [70, 100, 110]. Solid lines represent the boundaries of solid structures determined by X-ray diffraction [75, 70]. The dotted line is the interpolated bcc - fcc phase boundary. The dashed line is to guide the eye along the melting curve of lithium. The shaded area is the region below the melting curve in which X-ray diffraction lines disappear in condensed lithium. Pressure uncertainties are $\pm$ 1 GPa. Slope changes at 9 and 35 GPa represent small but clear change in the resistance versus temperature (+).

and confirmed the lack of any reaction between the diamonds and the sample by several observations:

(a) Lithium remained shiny throughout both resistivity and visual observation experiments and no sign of darkening, change of color, or loss of metallic luster was observed over long periods of data collection (Figure 3.1). Data were collected in five separated runs, each lasted anywhere from two to seven days.

(b) The diamonds remained intact after completing each pressure run and were reused.

(c) Some of the ruby spheres (Cr doped Al_2O_3) that were used to measure the pressure were embedded in the sample, and all of them remained active.

(d) After cooling, the electrical resistance of the sample returned to the initial value at lower temperatures. This, however, required several hours of annealing to recover the sample from cold working.

(e) The discontinuity at electrical resistivity was observed at the same temperature for

a given pressure and was reproducible.

(f) While there was hysteresis between melting and recrystallization, melting occurred consistently at the same temperature. The recrystallization temperature was highly dependent upon the rate of cooling, and in all instances recorded, it was lower than the melting temperature. This difference between the melting and recrystallization temperatures of lithium have been reported previously at ambient pressure [110] and is observed in many materials due to cold working [94, 22, 156, 178, 21].

(g) Consistent melting data points have been taken in random pressure order during several runs, in one of which the sample was kept in a cryostat and below room temperature during the entire run.

(h) During resistivity measurements we once cooled the sample to 4 K and measured its superconductivity at 45 GPa, which was consistent with previous electrical resistivity measurements on lithium [160].

(i) The resistivity measurement resulted in consistent melting temperatures for both LiF and alumina as the pressure medium.

3.5 Results

In this study, we measured the melting line of lithium up to 64 GPa and observed several new phenomena (Figure 3.3). At about 10 GPa, we observed a jump in the melting temperature which may be indicative of a structural phase transition from bcc - fcc; this change agrees with the Clausius-Clapeyron relation, as the fcc phase is denser than the bcc phase. The melting temperature decreased monotonically and very quickly between 11 to 40 GPa, going from 535 to 310 K, in qualitative agreement with previous interpolations. This rapid decrease in melting temperature is consistent with theory, and may be indicative of the onset of a symmetry-breaking phase transition from fcc to a lower symmetry phase. The melting temperature showed a very flat landscape between 40 to 64 GPa and reached a minimum of 306 K at about 44 GPa. We did not observe any indication of melting below room temperature down to 77 K at any pressure, and the resistivity of the sample between 77 to 279 K had a nearly linear temperature dependence in all pressures (Figure 3.4). At two pressures, 19 and 35 GPa, an obvious change in slope was observed (Figure 3.4, inset). This change in slope in both cases is seen at pressures and temperatures very near solid-solid phase boundaries. We did not observe any obvious change in slope in the range of 200 K between 40 and 60 GPa, which would indicate a change in phase at the previous reported "cold melting" region. Our experimental limitation in determining the absolute value of the resistivity of lithium in the present experiments does not allow us to estimate

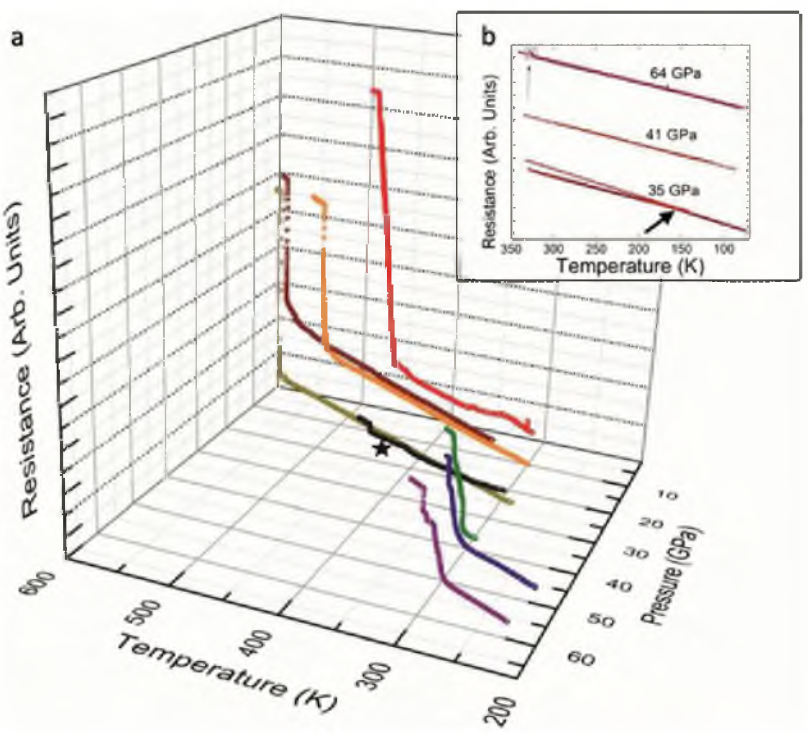

Figure 3.4. The resistance as a function of temperature. a) The resistance of lithium at different pressures. The sample size was smaller in the run shown by the black curve marked with a star in which the jump in the resistivity is proportionally smaller. b) The resistance versus temperature from room temperature to 77 K at 35, 41, and 64 GPa. Melting at 64 GPa was observed above room temperature inside the cryostat (see arrow); melting at 35 and 41 GPa was measured in the homemade oven outside of the cryostat (see text). Red dotted lines in the subset graph are linear guidelines. A change in slope is observed at 35 GPa. Arrow in the subset graph points to the change in slope at 35 GPa near the boundary of fcc - CI16/hR1 phases.

the pressure dependence of the resistivity of lithium on a high temperature isotherm. A four-probe resistivity measurement at room or higher temperature would provide insight to the electronic properties of this phase.

We observed a large contrast between our melting temperatures above 40 GPa with earlier results on the melting curve of lithium using an X-ray diffraction technique [70]. Above 40 GPa, lithium undergoes several symmetry breaking structural phase transitions to low symmetry phases and the x-ray studies on the sample are very challenging. Loss of solid X-ray diffraction peaks is not a proof of melting if the liquid peaks are not observed. which is the case for the previously reported melting line ([70], section 3.3). One possibility is that the lithium in these X-ray studies has been supercooled to form a glassy, or highly

disordered, phase due to cold working. Information on the thermodynamic paths of the sample is necessary to rule out this possibility. While detailed information is not provided in the previous X-ray studies about the thermodynamics paths of the sample, it has been specified that the sample has been mainly kept below 200 K and in some instances data could have been collected at 300 K for 2 to 3 hours, which may not be sufficient time for annealing the sample. Cold working can cause a drop in the recrystallization temperature, and in lithium we could show a very large effect at ambient pressure by rapid cooling of the sample (Figure 3.1(d)). Recrystallization temperature (TRC) is not a fixed temperature like melting point temperature (T_m),and in pure metals it can be as low as TRC $\approx 0.4T_m$ [21]. The recrystallization behavior depends on several variables, including temperature, time, initial grain size, and amount of recovery or polygonization prior to the start of recrystallization [21], and the extent that material is cold worked can be substantial in high pressure experiments.

3.6 Conclusion

In conclusion, the result of this study does not support any drastic effect on the melting temperature due to lattice quantum effects at any pressure, in contrast to previous X-ray experiments [70]. Our results, however, do not exclude the importance of lattice quantum dynamics, which are present in both liquid and solid phases, to the high pressure properties of lithium.

3.7 Notes on Laser Heating

We did not succeed to measure the melting temperature of lithium by laser heating method. However, during these pulsed laser heating attempts, we observed a reversible change in the sample's appearance between 16 and 40 GPa. A sample of lithium in an argon pressure medium was heated from room temperature to a few hundred degrees above its melting temperature with 40 ns pulses of 1064 nm light from an Nd:Yag laser. The sample turned black in the visible and IR above 25 GPa. The appearance of the sample did not change when the pressure was increased to 40 GPa. We then released the pressure slowly to 16 GPa and over the course of a few hours the sample returned to its original appearance. In the absence of a sudden temperature change, the sample remained shiny at all pressures studied.

The blackening of the sample has been reported in the past by some groups, but was not seen in other studies [75, 62, 21]. We find that this process is highly dependent on the thermal history, and is reversible. The precise nature of this change is not yet clear, but the

phenomenon emphasizes the importance of identifying the thermal history of the sample during high pressure studies.

CHAPTER 4

TWIN SAMPLE CHAMBER FOR SIMULTANEOUS ELECTRONIC TRANSPORT MEASUREMENT IN A DIAMOND ANVIL CELL

The results of the melting curve of lithium as a function of pressure (Chapter 3) did not provide conclusive results regarding the dominance of quantum effects in dense lithium. Whilst it did show a distinct maximum and minimum, the lowest temperature of the melting remained high enough to preclude cold melting. In order to further investigate the quantum properties of lithium, a new method of simultaneous measurement was conceived. In order to measure the properties of two samples fairly, it was decided the sample must experience the same conditions and same history. This would mean that two samples must be loaded into the DAC, and the transport properties could then be measured simultaneously. This chapter outlines this novel technique with a test sample of YBCO.

The original concept for simultaneous measurement was provided by S. Deemyad. Experimental setup design was provided by A.M. Schaeffer (Richards). Experimental measurements and analysis performed was by A.M. Schaeffer. The manuscript was written by S. Deemyad and A.M. Schaeffer (Richards).

Reprinted with permission from Review of Scientific Instruments, Deemyad, S. 2013. Twin sample Chamber for Simultaneous Electronic transport Measurement in a Diamond Anvil Cell, *Review of Scientific Instruments* , 84, 095108. Minor changes to text and figures were made at the request of the committee as well as the University of Utah Thesis Office.

4.1 Abstract

In static high pressure experiments, performed within a diamond anvil cell (DAC), several different methods of thermometry may be employed to determine the temperature of the sample. Due to different DAC designs or particular experimental designs or goals,

uncertainties in the determination of the temperature of a given sample exist. To overcome the inaccuracy in comparing the temperature dependence of transport properties of different materials at high pressure, we have used a novel design of resistivity measurement in a twin sample chamber built on an insulated gasket in a DAC. In this design, the transport properties of two samples are measured simultaneously and therefore the two samples are always in thermal equilibrium. The uncertainties in the temperatures of the two samples are exactly the same and therefore their relative phase diagrams are compared precisely. The pressures of the chambers can be slightly different and are easily determined by the ruby pieces placed in each chamber. To demonstrate the feasibility of this method we have compared the superconducting properties of two $YBa_2Cu_3O_{7-x}$ ($0 \leq x \leq 0.65$) samples with slightly different superconducting transition temperatures at ambient pressure as a function of pressures up to 11 GPa. The upper limit of the pressure can be achieved using this design would be lower than single chamber gaskets. The highest achievable pressure, as in a conventional single hole setup, depends upon the thickness of the gasket, the culet size, the size and symmetry of the sample chamber. For the twin chamber, it also depends upon the separation of the holes from each other as well as from the edge of the culet.

4.2 Introduction

Static high pressures of several million atmospheres can be achieved in a DAC. In an DAC variety of remote and in-situ measurements, such as transport, optical and magnetic measurements, can be carried out at extreme conditions. Comparing the physical properties of different materials, sometimes with slight differences, as a function of pressure is done in many studies. However, uncertainties in reproducing the exact experimental conditions often challenges proper comparative studies on materials studied in different high pressure experiments. One such problem is comparing P-T phase diagrams or critical temperatures for phase transitions of different samples as a function of pressure. While temperature measurements can be carried out with high precision at relatively close distances to the samples in a DAC, the relation between the measured temperature and the actual value of temperature in the location of the sample depends on many factors. Slight differences in the design of high pressure cells, methods of thermometry or even slightly different temperature gradients which are present in the same setup but in two different high pressure runs can lead to differences of the orders of few Kelvin between different experiments. These differences generally define the boundaries of the phase diagram of a material. For many cases of comparative high pressure experiments, the study of the small differences between the

temperature dependence of various physical properties of different materials is the desired result. These small differences can easily fall within the boundary of the uncertainties in temperature. In this work, to overcome the uncertainties in temperature differences between the two samples we have used a new method of simultaneous resistivity measurements with a twin chamber gasket. In a twin chamber gasket, two identical holes, serving as pressure chambers, are symmetrically drilled into a gasket (Figure 4.1, inset). A twin chamber gasket for optical studies has been recently used by Shukla et al. [162], in which the one sample was loaded in one chamber and the ruby was loaded in the other chamber to prevent contamination from the ruby, a source of oxygen, to the sample to be synthesized at high temperature and relatively high pressure. In this work, we have modified a gasket with a twin chamber design for transport measurements in a diamond anvil cell.

4.3 Experimental Setup

In series of experiments, we have used various design of the chambers in a gasket. While in these experiments we have achieved pressures as high as 21 GPa, there is no reason to assume that 21 GPa is the limit of highest pressure could be reached in this design. The placement of the holes plays a very important role for the eventual drift in pressures of the twin chamber cell. The symmetry of the holes has been shown to be the most important factor for avoiding an early failure of the gasket. The next important parameter is the initial distance between the holes. The region of the highest pressure in the cell is the middle of the culet, in between the two gasket holes [20]. This region will always deform, making the spacing between the two holes larger. On the other hand, very small separation between the two holes provides a thin barrier between the two samples and may fail under pressure, allowing electrical contact between the two samples. Proper distance between the holes is crucial in successful simultaneous transport measurements in twin chamber design. We have tried several arrangements of chambers with initial radii varying between 80 μm $\leq r \leq$ 140 μm and the nearest distance between the inner side of holes varying from 10 μm $\leq d \leq$ 100μm on 500 μm single beveled diamond anvils. The minimum drift of the pressure chambers from each other (Figure 4.2), which can warrant achieving maximum pressures, were achieved in the design that we explain here.

A gasket with twin sample chambers was prepared with some modification after the model by Shukla et al. [162]. A gasket was preindented with 500 μm culet diamonds to $\leq$ 50 μm thickness, gaskets with a greater than 50 micron thickness were found to be unstable and prone to collapse. Two 120 μm diameter holes were drilled symmetrically with an

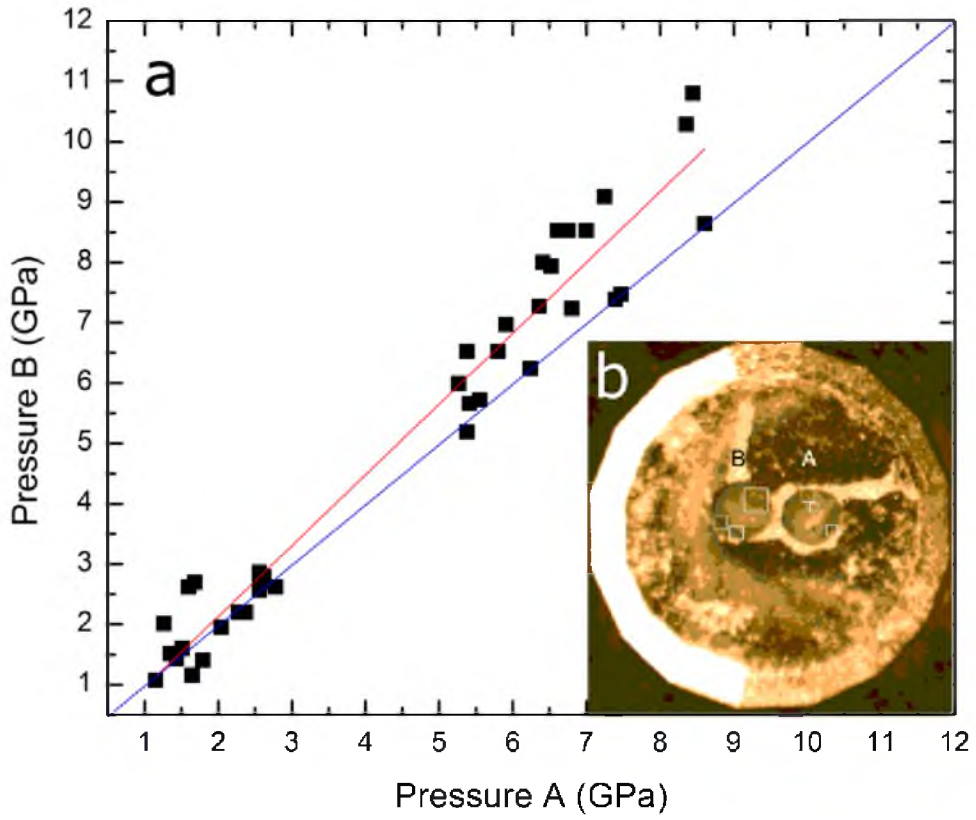

Figure 4.1. The correlation between the pressures in the two chambers up to 11 GPa. Three rubies across each sample chamber are measured for each pressure. The blue line is a guide to the eye, having a slope of 1. Red is a linear fit for PA vs. PB.

electric discharge machine (EDM) less than 20 μm apart from each other. The holes are drilled with micron precision by a modified EDM from Hylozoic Products. Micrometer precision for drilling is achieved by adding a centering microscope to the EDM stage. Two identical magnetic kinematic mounts are secured under the EDM wire and under a centering microscope respectively. The gasket was held in a cup that could be moved between the magnetic mounts, returning to exact position in each location. Initially, a centering mark is drilled on the edge of the gasket, well removed from the preindentation area, then the gasket is moved to under the microscope. In the next step, microscope, which itself is mounted on an XY stage, is centered on the mark. Then the gasket was centered with respect to the microscope and shifted on one axial line away from the center for half the desired distance

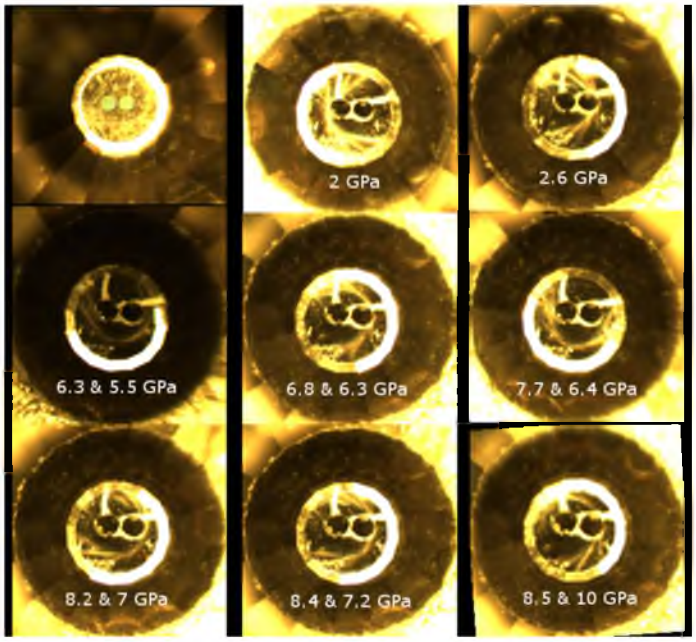

Figure 4.2. Evolution of gasket under pressure. The pressures shown are the pressure in either sample chamber. The probes are mounted on the opposite side.

between the holes. The gasket is then moved under the EDM wire and the first hole drilled. The gasket is moved back under the centering microscope, which should be centered with the drilled hole if the alignment is still good. Next the gasket is moved along the same axial line, proper distance away from the first hole, and the next hole is drilled by the EDM.

For transport measurements, the gasket must be electrically insulated. Thermally conducting STYCAST 2850 KT (BLU) epoxy by Emerson and Cuming was used to insulate the gasket from the DAC, also to insulate the top of the gasket. A thin layer of epoxy was painted onto the entire top surface, save for a small region to attach an electrical lead to the gasket, and roughly one third into the preindentation. At least three spherical rubies were loaded into each gasket hole before packing each hole and the preindentation with a combination of fine lithium fluoride and alumina powder which serves as a pressure medium as well as electrical insulation. The powder is pressurized until the gasket holes slightly deform and the powder becomes clear. Depending on the material studied in a particular experiment, a range of different insulating solid pressure transmitting materials, such as NaCl or a mixture of epoxy and alumina, can be used instead of the particular combination we used here. The resulting layer is then secured on its outer edges to the preindentation area with superglue. Smaller holes are poked into the gasket holes with a 70 μm tipped

acupuncture needle.

Two quasi−four probes are built onto the insulating gasket using leads cut from a 25 μm thick platinum foil. The Pt leads are secured to the top of the gasket with superglue with the ends tied to 35 AWG copper leads. The joints between the Pt and Cu leads are secondarily secured with silver epoxy over the mechanical connection. To prevent the failure of the entire pressure run, two additional leads were added to each quasi-four probe as back-up leads.

To test the system we used two small pieces of two different samples of $YBa_2Cu_3O_{7-x}$ ($0 \leq x \leq 0.65$), with slightly different superconducting transition temperatures at ambient pressure. The samples were labeled A and B with ambient pressure superconducting transition temperatures of 91.2 K and 89.2 K respectively. The samples were cut and loaded into each gasket hole making electrical contact with the respective quasi-four probes (2.3). Electrical contact between the samples as well as electrical contact of either sample with the gasket or the body of the DAC was checked and ruled out before beginning the pressure run and each data point.

The AC resistivity of both samples were recorded with two separate SR830 lock-in-amplifiers, shown in Figure 4.3. The reading from both lock-in amplifiers as function of temperature was recorded simultaneously using a LabView program. The constant AC current generated through the sample in different heating runs ranged from 10 mA to 100 μA. Since in this design samples and the electrical leads are very close to each other, it is necessary to pay close attention in designing the measurement circuit. To avoid electrical interference, which would be detected by both lock-in-amplifiers if the measurements are carried out at the same frequency, the transport properties of the samples was measured in two different frequencies. The frequency for sample A was 7.061 Hz and for sample B 13.023 Hz. The DAC was cooled to liquid nitrogen temperature inside a Janis SVT-200 cryostat with a calibrated diode thermometer in thermal contact with the DAC. In this calibration test we compared the pressure dependence of the superconducting critical transition temperature (T_c) of the two samples up to 11 GPa (Figure 4.4). Above 11 GPa, the T_c of sample A dropped below the minimum temperature that could be measured in our liquid nitrogen cryostat. The pressure in the two chambers started to deviate noticeably above 5 GPa. The deviations of the pressures in sample chambers does not create a problem as long as the difference is known. Three rubies in each sample chamber were spread and their fluoresce was measured for each different pressure. The correlation between pressures of the sample chambers are plotted in Figure 4.2. From 1 GPa to 3 GPa, the pressures in

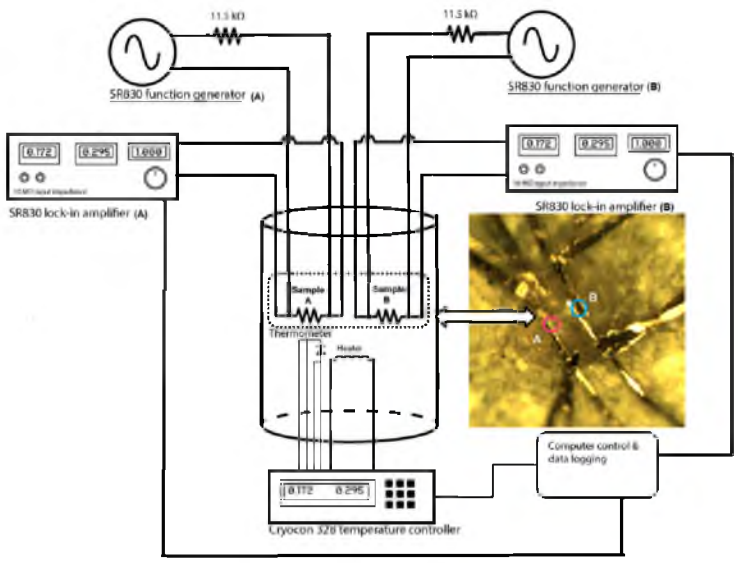

Figure 4.3. Diagram of the electrical circuit used to measure the two electrically isolated samples. The inset shows the quasi-four-point probes built on the twin chamber gasket.

each sample chamber are very close to being equal each other, with the pressure in sample B being slightly higher than sample A. Above 5 GPa, the pressure difference began to diverge more significantly. While the gasket holes continued to deform with increasing pressure, their deviation from the central radial line of the culet did remain symmetric up to the highest pressure. The pressures, as divergent as they became, remained within the pressure error bars of each other, the highest pressure in chamber A being close or higher than the lowest pressure in chamber B. The rubies were not completely symmetric inside each sample chamber, the rubies for chamber B were placed closer to the center of the culet than the rubies for chamber A. The initial drift of the sample chambers slowed down as the pressure increased and there was no sign of approaching the maximum possible pressure.

4.4 Conclusion

This experiment has shown the feasibility of conducting a comparison of two samples within the same diamond anvil cell. The ability to measure two samples simultaneously allows for temperature dependent properties to be precisely recorded even if the method of thermometry is not as absolutely accurate. The simultaneous measurements of transport properties as a function of temperature have been shown to be precise and capable of determining differences of 1 K or less.

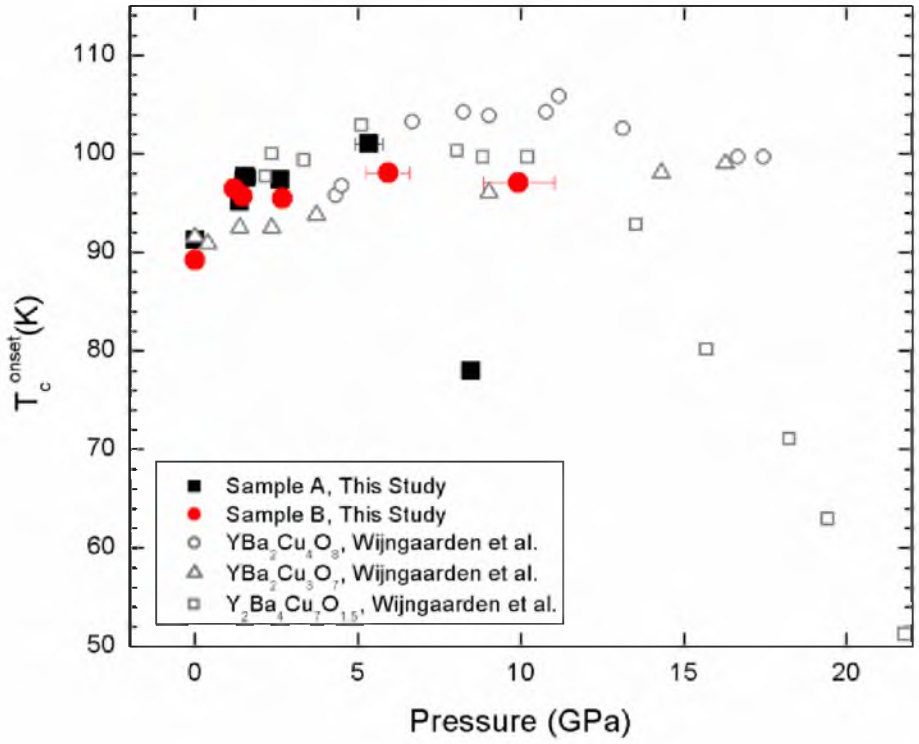

Figure 4.4. The superconducting phase diagram of two $YBa_2Cu_3O_{7-x}$ ($0 \leq x \leq 0.65$) samples with slightly different initial critical temperatures were measured as a function of pressure to test the feasibility of simultaneous transport measurements at high pressure in twin chamber design. Open symbols are plotted from previous high pressure studies for comparison [191].

4.5 Notes

Since the publication of this work, this method has been much improved. Whilst the method did not change, improvements such as better precision in aligning the holes was accomplished through operator practice. The following chapter (Chapter 5), provides results of this method to lithium isotope samples.

CHAPTER 5

HIGH-PRESSURE SUPERCONDUCTING PHASE DIAGRAM OF ^{6}LI: ISOTOPE EFFECTS IN DENSE LITHIUM

In order to further investigate the potential quantum solid properties of lithium, the superconducting isotope effect was thought to be usable to shed light on the question. After developing a method for simultaneous transport measurements (Chapter 4), the same method was employed for two stable isotopes of lithium, one with natural isotopic composition ($\approx$ 92 % ^{7}Li and $\approx$ 8 % ^{6}Li) and one isotopically enriched sample ($\approx$ 95 % ^6Li and $\approx$ 5 % ^{7}Li. The superconducting isotope effect was chosen due to the low temperatures at which the effect occurs, the distinct trend of a function of pressure which natural lithium had been shown to exhibit [42, 160, 172], as well as the sensitivity of the transition to resistance measurements.

The design of the experimental setup was provided by S. Deemyad and A.M. Schaeffer (Richards). The experimental measurements and analysis were carried out by A.M. Schaeffer and S.R. Temple with additional pressure analysis provided by J.K. Bishop. The manuscript was written by S. Deemyad and A.M. Schaeffer with contributions from S.R. Temple and J.K. Bishop. Incidental experiment assistance was provided by A.M. Freidman.

Reprinted with permission from the Proceedings of the National Academy of Sciences, Deemyad, S., Temple, S.R. and Bishop, J.K. 2015. High Pressure Superconducting Phase Diagram of ^{6}Li: Isotope Effects in Dense Lithium, *Proceedings of the National Academy of Science* , 112, 60 - 64. Minor changes to the text and figure were made at the request of the committee and the University of Utah Thesis Office.

5.1 Abstract

We measured the superconducting transition temperature of ^{6}Li between 16 to 26 GPa, and report the lightest system to exhibit superconductivity to date. The superconducting phase diagram of ^{6}Li is compared to that of ^{7}Li through simultaneous measurement in

a diamond anvil cell (DAC). Below 21 GPa, Li exhibits a direct (the superconducting coefficient, α, $T_c \propto M^{-\alpha}$, is positive), but unusually large isotope effect, while between 21 to 26 GPa, lithium shows an inverse superconducting isotope effect. The unusual dependence of the superconducting phase diagram of lithium on its atomic mass opens the question of whether the lattice quantum dynamic effects dominate the low temperature properties of dense lithium.

5.2 Introduction

Light elements (Low Z) and their compounds have been the subject of many recent studies for their potential as high temperature superconductors (e.g. [26, 198, 104, 184, 80]). Due to their low mass, the physical properties of the low Z compounds can be strongly influenced by large zero-point effects (lattice quantum dynamics) in the physical properties [76] and mass-related isotope effects may be present in their thermodynamics of vibrational degrees of freedom of low Z compounds. Such effects will influence the superconducting properties of these materials. Dependence of superconductivity on isotopic variations of low Z compounds can be used to probe and determine the magnitude of mass-related effects. This in turn allows better development of models to determine their superconducting properties.

Under ambient pressure, lithium is the lightest elemental metallic and superconducting system and it exhibits one of the highest superconducting transition temperatures of any elemental superconductor under compression [147, 177, 87, 29, 12]. Despite the large mass difference between the stable isotopes of lithium (~15 %), isotope effects in superconductivity of lithium have not been studied before.

In systems with long-range attractive potential such as coulomb systems the ratio of lattice zero-point displacements to interatomic distances may increase under compression (increase to the Lindemann ratio at high densities), provided they retain their long-range interactions [77, 170]. (This is opposed to systems with short-range interactions, e.g., helium, in which the lattice becomes more classical under compression.) In these systems, more deviations from the static lattice behavior are expected at higher densities. At sufficiently low temperatures, where thermal energy is small, lattice quantum dynamics can play a more dominant role in the bulk properties. Sound velocity measurements on stable isotopes of lithium at 77 K and up to 1.6 GPa show that quantum solid effects in lithium, at least in the pressure range studied, do not decrease as a function of pressure [67]. Raman spectroscopy studies between 40 to 123 GPa and at 177 K report a reduced

isotope effect in high frequency vibrational modes of Li, which may be related to quantum solid behavior [62]. Up to this point, no experiments have reported a comparison of any physical properties of lithium isotopes at low temperatures and high pressures concurrently. Since the superconducting transition of lithium occurs in a relatively low temperature range [160, 42, 172], studying its superconducting isotope effect provides excellent conditions to search for zero-point lattice effects and their evolution as a function of pressure.

In the present study, we have measured the superconducting isotope effects in the stable isotopes of lithium under pressure. Lithium is a simple metallic system which is expected to exhibit conventional phonon mediated superconductivity and a well-defined superconducting isotope effect with nominal pressure dependence of the relative $T_c s$ [175] (according to the model by Treyeva and Trapezina, [175] using theoretical values of Coulomb coupling constant, $\mu^*(P)$ [30] by Christensen and Novikov and EOS of lithium [74] by Hanfland et al., assuming similar structures for the two isotopes, should not vary by more than 10 % for 15 GPa $\leq P \leq$25 GPa). Since phonon-mediated superconductivity depends on lattice and electronic properties of a material, any unusual isotopic mass dependence of the superconducting phase diagram can be indicative of the effects of large lattice dynamics on electronic and/or structural properties.

5.3 Experiment and Results

The expected conventional isotopic change in T_c of lithium is $T_c^{6Li} \approx 1.08 T_c^{7Li}$. This leads to a relatively small temperature shift at low temperatures, where lithium becomes a superconductor ($^{max}T_c^{7Li} = 20K$, for which a BCS isotope shift of <2 K is expected for ^{6}Li) [160, 42, 172]. This small difference in the relative Tc's and lack of in situ thermometry in a DAC makes designing conducting experiments sensitive enough to resolve the differences challenging. Any inconsistency in the temperature measurement between experimental runs may mask the expected isotope effect. In addition to experimental uncertainties, differences in a sample's thermal history may change T_c [46]. This is especially so for Li, in which it is know that the boundaries of the martensitic transition (bcc - hR3) can be shifted if the sample is not annealed [122]. To achieve the required resolution in evaluating the relative $T_c's$ of the two samples, both isotopes were measured simultaneously inside the same DAC, shown in Figure 5.1 [153, 162]. The details of these experiments are given below, and the general principles of the method used have been previously published [153] (Figure 4.4). Previous comparative measurements on the low temperature electrical resistivity on lithium isotopes under ambient pressure also noted the importance of

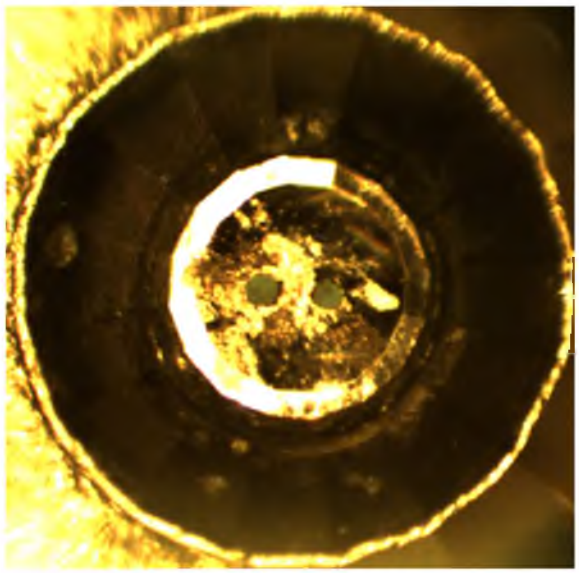

Figure 5.1. A picture of a twin chamber gasket drilled with alumina pressure medium and rubies. The symmetry of the two holes is key to having an even pressure pressure distribution across both holes. Rubies are loaded into each sample chamber, and three rubies in each pressure chamber are measured.

simultaneous measurements [46]; however, simultaneous electrical measurements on large samples under ambient pressure are less technically limiting than similar measurements under high pressure. Considerations regarding the thermal history are important for any comparative studies, such as structural or magnetic studies on lithium isotopes.

In the present work, we have used two isotopically rich samples of lithium; a ^{6}Li-rich sample (the ^{6}Li samples contained 99.99 % lithium with the isotopic composition 95.6 % ^{6}Li and 4.4 % ^{7}Li together with the metallic impurities of Na, Mg, Al, and other elements; Sigma Aldrich) and a ^{7}Li-rich sample (the isotopic composition of the 99.9 % pure natural lithium was 92.41 % atomic ^{7}Li and 7.59 % atomic ^{6}Li; the metallic impurity composition was the same as in the case of the ^{6}Li; Sigma Aldrich), which we refer to as ^{6}Li and ^{7}Li samples respectively for the remainder of this manuscript.

All measurements were carried out in a DAC using electrical resistance as a means of determining the superconducting transition temperatures. All pressure increases were carried out at room temperature. The return to room temperature after every measurement allowed the samples to be transformed to their equilibrium phase. Lithium reacts readily with many materials including diamond [160, 172, 70], which may cause a DAC to fail. In order to prevent any such reactions, compressed, dehydrated alumina powder, which

was heat treated at 110 ° C to remove moisture, was used both as an electrical insulator and a pressure medium [155]. This allowed us to keep the samples at room temperature inside the DAC without risking failure of the diamonds. An insulated gasket was made from a 250 μm thick stainless-steel foil, preindented to a thickness of 40 to 55 μm. Two pressure chambers with initial diameters of 110 μm were symmetrically drilled 10 to 20 μm apart from each other on the gasket and several ruby spheres were dispersed evenly in each pressure chamber. The gasket then was insulated with a mixture of epoxy and alumina.

The use of alumina as pressure medium exposes the sample to nonhydrostatic conditions that may in principle affect the superconductivity. However, in the case of lithium, studies up to 50 GPa in which no pressure medium was used, show very sharp Bragg peaks. This provides evidence that lithium itself remains a very soft solid which does not support large shear stresses [74, 75]. (The superconducting phase diagram of ^{7}Li measured using helium as hydrostatic pressure medium by Deemyad and Schilling and nonhydrostatic measurements by Struzhkin et al. without any pressure medium, are very similar below 30 GPa). In the current work, the presence of quasi-hydrostatic conditions is supported by the sharpness of ruby peaks.

We have used high precision spectroscopy to measure the pressure distribution of each chamber from several ruby spheres. The maximum pressure gradient remained below $\pm$ 0.8 GPa up to the highest pressure measured; see section 5.2 and notes on pressure distribution for further discussion. In a twin chamber gasket, not only the absolute pressure difference between the chambers and the pressure gradient across each sample is measured but also each chamber on its own acts as an independent indicator of the pressure dependence of the properties of its sample.

An isolated quasi-four probe arrangement was built on each sample chamber using platinum electrodes. To eliminate the interference between the two circuits, each circuit was connected to a separate lock-in amplifier and run on a different frequency ($\approx$ 5 and 13 Hz). To prevent any possible chemical reactions, the samples were loaded and pressurized inside a high purity dry argon glovebox. An AC current of $I_{rms} \approx 100$ μA was applied across each sample. Since the arrangement used here was a quasi-four probe, a small portion of the signal always came from the piece of Pt electrode in the path (Figure 5.2). The onset of superconductivity was defined by the temperature at which the resistance of sample drops to zero (Figure 5.3). As an additional test of superconductivity, we used a small magnetic field ($\sim$100 Oe) to suppress T_c (Figure 5.3 b and c). The experiments were completed with 6 separate loadings of the lithium isotopes, all of which overlapped in pressure range and

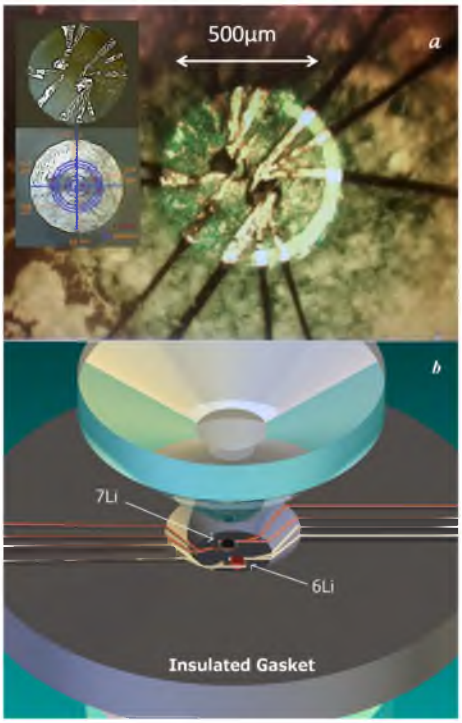

Figure 5.2. Experimental set up for simultaneous measurements. a) Twin chamber gasket built on a 500 μm culet diamond which is used in the present experiments in a DAC for simultaneous measurements of superconductivity. Each pressure chamber has a pair of extra Pt leads and contains several pieces of ruby for accurate determination of pressure gradient within each pressure chamber. The insets show the gasket and samples under reflected light only, at 21.3 GPa, demonstrating the metallic appearance of both samples and map of ruby pieces inside each pressure chamber in the same run. b) Schematic drawing of the twin chamber design used in the experiments. Small portions of the platinum leads in the path contribute to the total resistance measured for each sample. The electrodes for measuring the resistance of ^{6}Li and ^{7}Li are shown in different colors.

showed complete internal consistency.

Figure 5.4 part a shows the superconducting phase diagram of ^{6}Li and ^{7}Li for pressures between 16 and 26 GPa. The correlation between the superconducting transition temperatures of the two isotopes is anomalous and in the range of this study three distinct regions can be identified. The sign of $\frac{dT_c}{dP}$ in the pressure range 16 GPa $\leq P \leq$26 GPa changes two times for ^{6}Li. In this region, the slope is always positive, though not constant, for ^{7}Li. A change in slope may be indicative of the presence of a structural phase boundary (such as hR3 to fcc for ^{7}Li). Between 16 and 21.5 GPa, the superconducting Tc of ^{6}Li is higher than that of ^{7}Li. Figure 5.4 c shows the calculated values of the superconducting isotopic coefficient, α, $T_c \approx M^{-\alpha}$, as a function of pressure. The lowest pressure points at 16 and 18

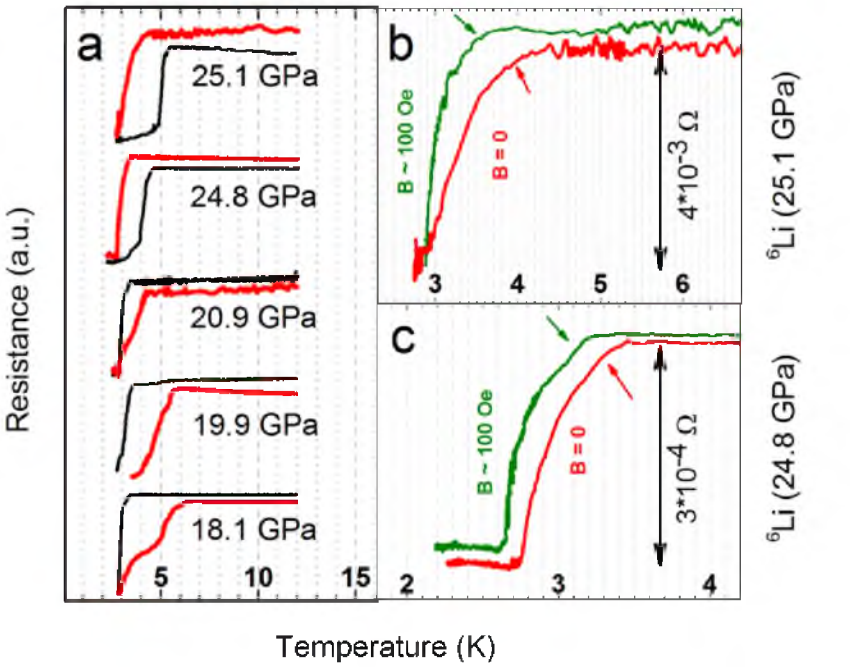

Figure 5.3. Electrical signals from lithiums samples. a) Superconducting transitions as determined by electrical resistivity. All black lines show transitions for ^{7}Li, red lines are the transitions for ^{6}Li. Each pair shows the simultaneous measurement. The double step in 18.1 GPa transition of ^{6}Li may be related to presence of mixed phases with different $T_c's$ at a structural phase boundary. The samples' resistances in a normal state above their superconducting transitions is 0.5-10 m Ω varying by the sample size and geometry. These values would give an estimate of $\rho \approx 0.5$ - $1\mu\Omega$cm, at room temperature, for a typical sample size of $50 \times 50 \times 10\mu m^3$. An RRR value of $\approx$ 75 is estimated from ambient pressure measurements on the samples used here [162]. The transitions above are scaled for ease of comparison. b,c) The shift of T_c with an applied external magnetic field of B $\approx$ 100 Oe for ^{6}Li at 23.3 and 26.6 GPa. B $\approx$ 100 Oe for green lines and B=0 for red lines.

GPa for ^{6}Li display an initial positive slope $\frac{dT_c}{dP}$, however, the paucity of data in this region does not allow to properly assign a slope of α vs. pressure. For 18 GPa $\leq P \leq$21.5 GPa, the value of the isotopic coefficient decreases monotonically with pressure, and the value of α is always higher than expected for BCS-type superconductors, $1 < \alpha < 4$. For P >21.5 GPa, the value of the isotopic coefficient, α, changes sign and remains constant within error ($\alpha \approx -1.5 \pm 0.5$).

Figure 5.4 b shows the superconducting phase diagram of ^{7}Li which has been plotted

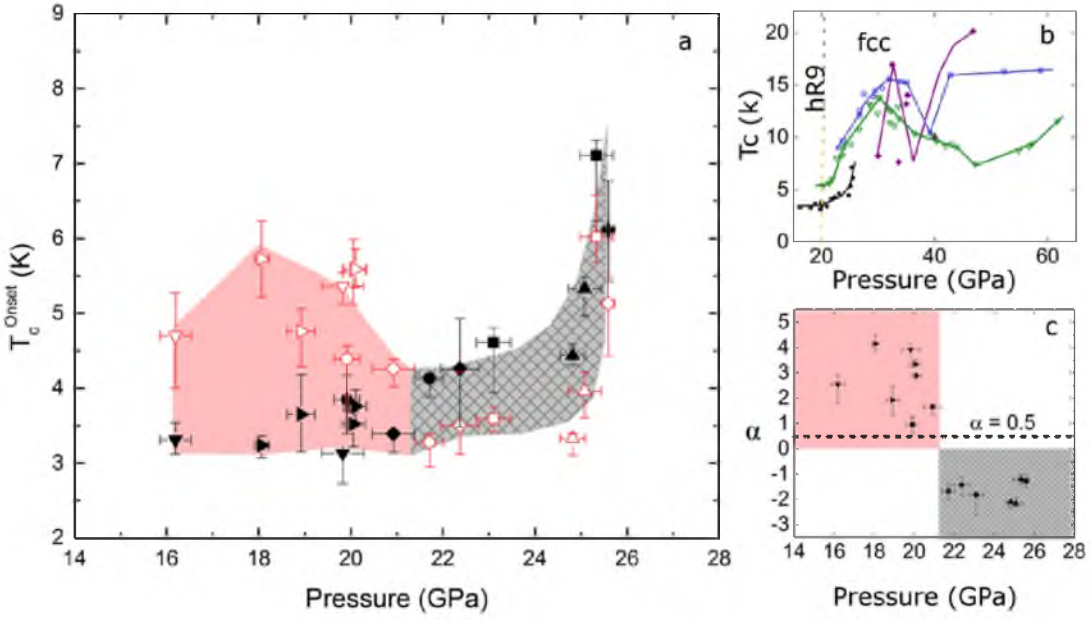

Figure 5.4. Results of the measurements of the superconducting $T_c's$ of lithium isotopes. a) Superconducting phase diagram of lithium isotopes. Open shapes represent ^{6}Li, solid shapes represent ^{7}Li. The different shapes designate separate loadings. The pink shaded region from 18 GPa to 21.5 GPa shows the direct isotope effect with a large difference in the $T_c's$ for ^{6}Li and ^{7}Li. The grey shaded region shows the inverse isotope effect from 21.5 GPa to 26 GPa. The pressure error bars represent the maximum pressure difference between all the rubies shown in Figure 1 in the two chambers (the value is generally is equal to the difference between the pressure from the ruby in the smallest radii of one chamber and the ruby in the largest radii of the opposite chamber). The T_c onset error is determined from the resistance signal, the upper error marking the first drop in resistance from a normal metallic state, the lower error is determined by the completion of the change in slope of resistance. b) Comparison of the various superconducting phase diagram of natural lithium measured by various techniques (Open triangles: Deemayd and Schilling [42], Open squares: Struzhkin et al. [172], diamonds: Shimizu et al. [160]. and circles: this study). The solid lines are guide to eye. Dashed line is the speculated boundary between hR3 and fcc at low temperature. c)The isotope coefficient, a, as a function of pressure. The dashed line at α = 0.5 shows the expected value for a conventional isotope effect.
The errors from the T_c onset measurements are propagated through the calculation.

here together with all the previous measurements. The current result only overlaps with the studies of Deemyad and Schilling [42] for 22 GPa $\leq P \leq$26 GPa. As shown in Figure 5.4 c, the measurements of the superconductivity of natural lithium in the present work display the same trend as Deemyad and Schilling (with the shallow slope at the beginning followed by rapid increase in the slope). The present measurements consistently show slightly lower transition temperatures than Deemyad and Schilling, which can be caused by differences in thermometry and/or thermal histories of the samples and other differences between the methods that have been used. For example, Deemyad and Schilling never annealed their samples above 100 K, which, according to the phase diagram suggested by Guillaume et al. may not allow the sample to relax to fcc or bcc phase between pressure applications below 20 GPa [70]. In the present experiments, we applied the pressures at room temperature. For the comparison of the transition temperatures of the two isotopes, however, the samples compared need to have experienced the exact same thermal history and their relative transition temperature must be known precisely. All previous measurements of the high pressure phase diagram of lithium done in past (excluding the measurements of the superconducting phase diagram of natural lithium by Deemyad and Schilling) used no pressure medium [62, 160, 172, 74, 70, 75, 119]. The experiments done by Deemyad and Schilling used helium as pressure medium and found very reproducible results. The results, however, may have been influenced by diffusion of helium into the lithium lattice. Moreover, Deemyad and Schilling as well as Struzhkin et al. [172] used magnetic susceptibility to detect the superconducting transition. Magnetic susceptibility measurements currently cannot be employed for simultaneous measurements; critical for an experiment designed to characterize the slight differences between isotopes.

5.4 Discussion

For a BCS-type superconductor composed of one atomic species with a harmonic lattice, the T_c and the ionic mass follow the simplified relationship, $T_c \approx M^{-\alpha}$, in which α=0.5. This relation is mainly attributable to differences in the Debye temperature for different ionic masses of different isotopes. In the current experiment, we observe an anomalous isotope effect in the superconducting phase diagram of lithium that cannot be explained for a material with very harmonic lattice and absence of substantial mass related dynamic effects. Using conventional models in which a harmonic lattice condition is considered for deriving superconducting properties and equilibrium structures are evaluated using static lattice models. The eventual structure of lithium will require determination of the enthalpy

for the ground state, or the Gibbs energies otherwise. The manner in which the electronic energies are involved in the subsequent statistical averaging (in the presence of significant isotope dependent ionic displacements) becomes a very interesting question.

In the presence of large anhamonicity caused by large zero point effects, electrons do not see the lattice as a perfect crystal (this is the case even if the ionic displacements do not affect the structures of the isotopes) thus, in total, drastic deviations from conventional isotope effects in a superconducting quantum solid can be expected [171, 58].

Another possible mechanism that may be responsible for the isotope effects observed here can be the due to the differences in the structures of the two isotopes under pressure. For a solid with static lattice and in the absence of large zero point energy, the equilibrium distance between the lattice particles is determined by the minimum of the potential energy of the lattice and, to first approximation, is independent of the particles' mass [179, 93] and isotope effects in the structures are not expected. On the other hand, in a solid with large lattice quantum dynamics, the large zero point energy of the lattice will significantly contribute to the vibrational and rotational energies, which can have an impact on the equilibrium structures [179, 93]. Since BCS assumes identical structures for isotopes, the BCS superconducting isotope relation is not applicable in systems with a structural isotope effect. In the case of lithium, it has been theoretically shown that without inclusion of zero point energy some of the known structures of natural lithium (oC88) will not be stable. Therefore, it is not unexpected if the differences in the zero point energies of lithium isotopes lead to different structural phase diagram for them [117]. It should be emphasized here that given the known differences between the phonon free energies of the two lithium isotopes [63] one can see that large differences in structures of two isotopes is unlikely (although these measurements are not overlapping in pressure and temperature range with present work).

The structures of Li as a function of pressure (for pressures above 0.65 GPa [167]) are not known for T <77 K, which contains the boundaries of the hR3 phase(with bcc and fcc phases) [70]. This phase is thought to play an important role in superconductivity. Moreover, the isotopic dependence of the structures of lithium is not known in this pressure regime. Between 16 to 22 GPa, ^{6}Li exhibits a change from a positive to a negative slope in T_c. In contrast, ^{7}Li shows a positive slope in the entire range where superconductivity was observed. It is possible that the large difference in $T_c's$, the initial change in slope for ^{6}Li, and the opposite slopes observed between 18 to 22 GPa are caused by a low temperature structure in ^{6}Li not present in ^{7}Li. Low temperature structural studies are required to

characterize this region. Above $\approx$ 21 GPa, the superconducting T_c of ^{6}Li falls below that of ^{7}Li, this effect remains until the highest pressure studied here, $\approx$ 26 GPa. The inverse isotope effect in conventional superconducting systems is noted in some transition metal hydrides (MH), such as PdH, and in the element $\alpha-$U [78, 57, 52, 163]. The inverse isotope effect in MH has been attributed to the existence of large quantum effects in hydrogen, which cause anharmonicity in phonon spectra [86, 51]; an explanation which cannot account for the behavior of $\alpha-$U. If the unusual isotope effect in Li is solely a consequence of its zero point displacements and a consequent anharmonicity in its lattice, Li is the only elemental solid known to exhibit such behavior (dominant anharmonic effects may also be responsible for large positive isotope coefficient in pressures below 21 GPa). Another possible condition for inverse isotope effect is when the magnitude of the Coulomb coupling constant (μ^*) becomes comparable to the electron-phonon coupling constant (λ). However, in this case, a small T_c ($<$1 K) is expected for realistic values of the parameters [95]. For fcc lithium, this condition is theoretically not present [174] and cannot explain the sudden change in the sign of isotopic shift above 21 GPa. However, in the present case, electronic and structural effects may be entangled. Comparative structural studies for lithium isotopes at low temperature are very challenging but they are currently possible in 3^{rd} generation synchrotron sources. The results of this study would justify the investment on such works. The detailed comparative studies on additional low temperature properties of lithium isotopes may also shed light on the predicted properties of metallic hydrogen.

It should be emphasized that based on current experimental results and without complementary structural studies one cannot conclude a departure from isotope effects expected within BCS theory. Hypothetically, if the sequence of structural phase transitions in ^{6}Li were different from that of ^{7}Li, which on its own is an interesting mass-related effect, the present observations could still be consistent with a BCS model. Under such conditions, emphasis then would be on explaining isotope effects on the phase stability and the origin of such mass-related phase instabilities. However, should it turn out in follow up structural studies, that there is no significant difference in the PT phase diagrams of the two isotopes, it would imply that the present observations point to superconductivity-related physics, possibly the strength of the electron-phonon coupling. This could, for instance, be an effect of zero point vibrations on the ground state (i.e. T=0) electronic structure.

It is notable that isotopes of Li possess different quantum statistics, and natural lithium has been shown to exhibit nuclear order at one atmosphere [85]. The magnetic order in lithium isotopes may contribute to their superconducting isotope effects at ambient pressure

where natural lithium superconducts below 0.4 mK. Studying the isotope effects in ambient pressure superconductivity of lithium would be also enlightening.

5.5 Notes on Pressure Distribution

In order to ensure that there is an even pressure distribution across both of the samples, as extra loading of only rubies in alumina was performed in order to measure the ruby fluorescence cleanly as a function of the distance from the center of the culet. This was performed since the softness of lithium can at times cause it to diffuse around a ruby and hinder the measurement. In order to completely rule out the possibility of the two samples having drastically different pressures, the extra measurement was performed. The results of these measurements are shown in Figures 5.5, 5.6 and 5.7.

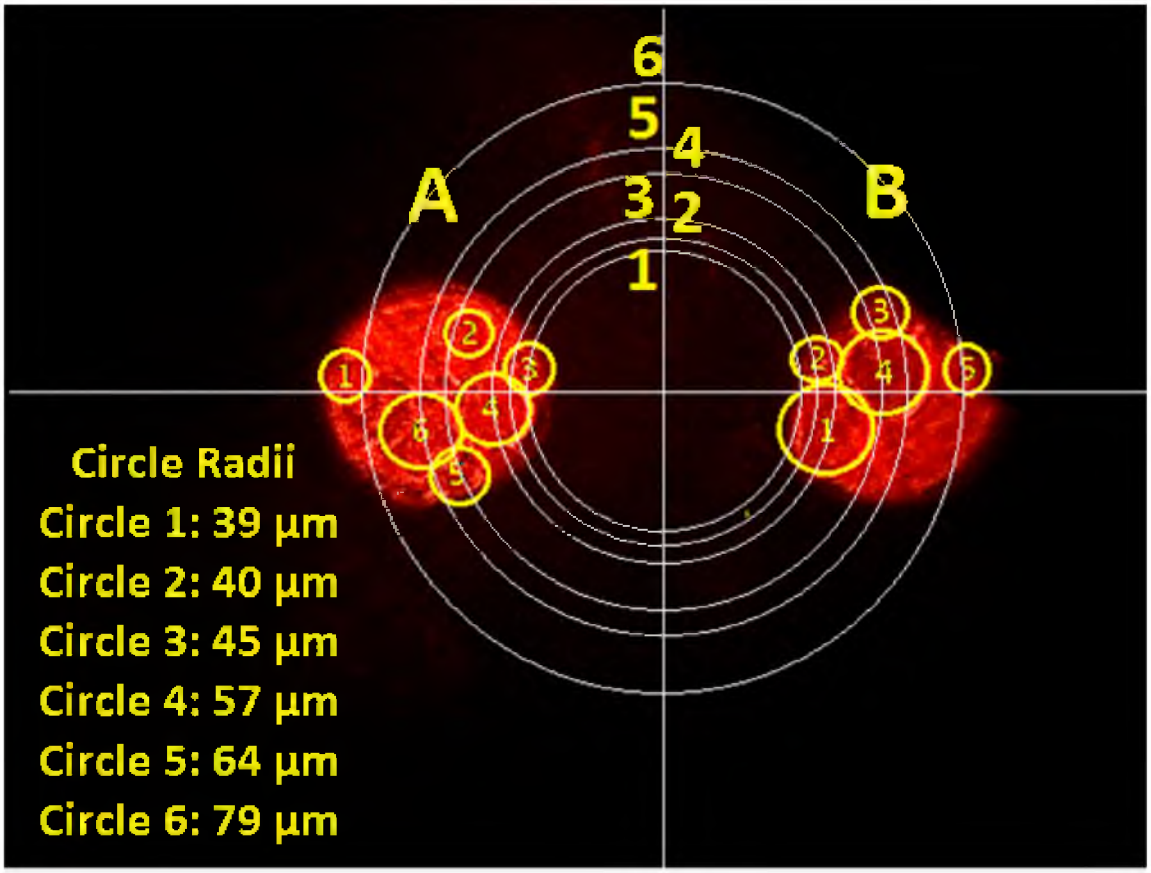

Figure 5.5. A diagram of the placement of rubies inside both twin chambers. The labeled radii refer to the distance of the rubies from the center of the culet.

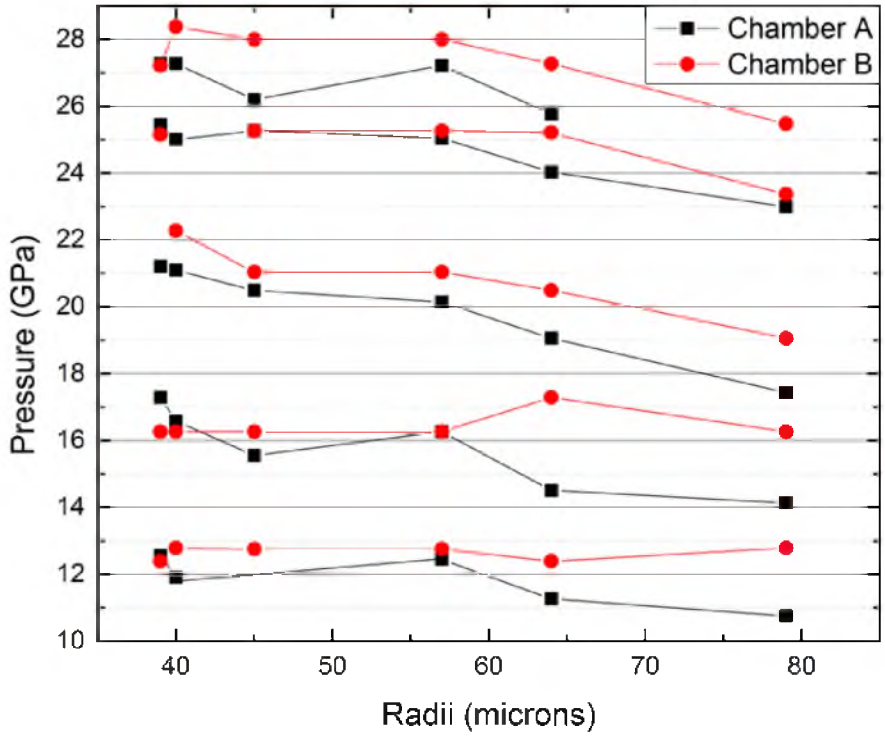

Figure 5.6. Using the radii measured and shown in Figure 5.5, a plot of the pressures for both samples as a function of radius is plotted. The black symbols and lines represent the pressures of the rubies in chamber A, and the red symbols and lines represent the pressure measured in Chamber B. Whilst the pressure error inside the entire cell could be $\pm$ 1 GPa, both samples appear to experience the same pressure gradient.

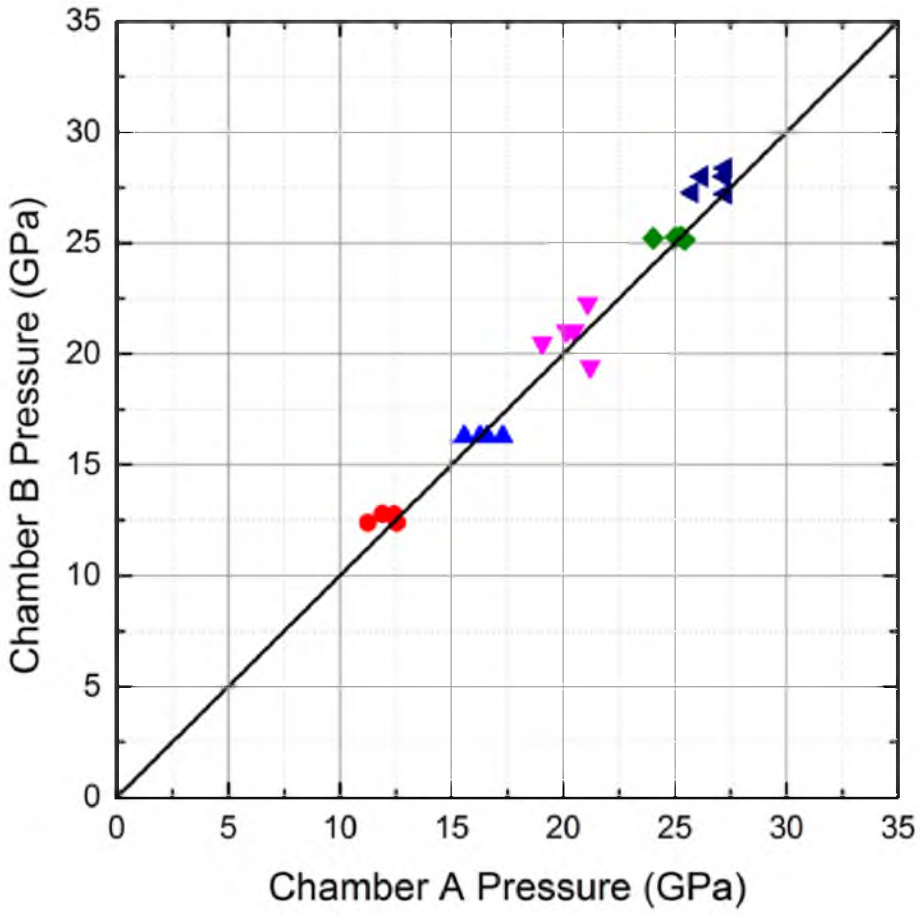

Figure 5.7. The pressures of the two samples chambers plotted as the measured pressure in chamber B as a function of the pressure in chamber A. The black line has a slope of 1, and serves as a guide to the eye to determine the drift of pressure between the sample chambers. Whilst there is some deviation from the line, the correlation between the pressures in each sample chamber is indeed rather close to the slope of 1. Comparing to the results from Figure 4.1, the improvement in the technique is quite evident.

CHAPTER 6

NEW BOUNDARIES FOR MARTENSITIC TRANSITION OF ^{7}LI UNDER PRESSURE

An important aspect of the nature of lithium is how its crystal structure changes as a function of both pressure and temperature. In Chapter 3, the melting curve as a function of pressure was investigated, showing that whilst the melting temperature does display a distinct maximum and reaches nearly room temperature near $\approx$ 50 GPa, this can be attributed to the series of symmetry-breaking phase transitions that lithium undergoes (bcc $\rightarrow$ fcc $\rightarrow$ hR1 $\rightarrow$ cI16) [132, 75, 4, 70]. Also, the superconducting critical temperature T_c appears to be affected by this series of structural phase transitions [42, 160, 172]. Lithium also undergoes a structural phase transition from bcc to hR3 at ambient pressure near $\approx$80 K. This phase had been thought to play a role in the low T_c of lithium at ambient pressure ($\approx$0.4 mK) [177, 14, 185]. Previous works have found the onset of superconductivity in lithium to be near 20 GPa [42, 160, 172], and it has been thought the boundary of the hR3 must lay nearby; the results shown in Chapter 5 indicate that superconductivity in natural lithium actually persists at pressures as low as 16 GPa below 4 K. This proposed an interesting question regarding the boundaries of the hR3 phase. If this phase does indeed suppress superconductivity (to temperatures below $\approx$2 K), then the boundary of the phase at low temperature should lay near this pressure. This chapter outlines the study of the martensitic phase boundaries between the bcc, hR3, and fcc phase as a function of pressure and temperature.

The proposals for this experiment for user programs at ORNL and APS were written by S. Deemyad. Experimental setup for neutron diffraction at Beamline 3, SNAP, at ORNL was designed and maintained, and additional assistance provided by A.M. dos Santos, J.J. Molaison, and C. Tulk. Data at SNAP were collected by A.M. Schaeffer (Richards), W.Z. Cai, and E. Olejnik. Experimental setup and assistance at HPCAT beamline 16-ID-B at APS, ANL, was provided and maintained by S. Sinogeikin, and C. Kenney-Bensen. Data at APS were collected by A.M. Schaeffer (Richards), W.Z. Cai, E. Olejnik, and S. Deemyad.

Neutron data analysis was carried out by A.M. Schaeffer. XRD analysis was provided by W.Z. Cai. Fits for equation of state data were carried out by A.M. Schaeffer, E. Olejnik, and W.Z. Cai. Manuscript was written by S. Deemyad and A.M. Schaeffer (Richards) with contributions from W.Z. Cai and E. Olejnik, and theoretical and experimental input from A.M. dos Santos, with other input from J.J. Molaison and S. Sinogeikin.

Reprinted with permission from Nature Communications, Deemyad, S., Cai, W.Z., Olejnik, E., Molaison, J.J., Sinogeikin, S., and dos Santos, A.M. 2015. New Boundaries for Martensitic Transition of ^{7}Li under Pressure, *Nature Communications* , 6, 8030. Minor changes to the text and figures were made at the request of the committee and the University of Utah Thesis Office.

6.1 Abstract

Physical properties of lithium under extreme pressures continuously reveal unexpected features. These include a sequence of structural transitions to lower symmetry phases, metal $\rightarrow$ insulator $\rightarrow$ metal transition, superconductivity with one of the highest elemental transition temperature and a maximum followed by a minimum in its melting line. The instability of lithium's bcc structure is well established by the presence of a temperature-driven martensitic phase transition. The boundaries of this phase, however, have not been previously explored above 3 GPa. All higher pressure phase boundaries are either extrapolations or inferred based on indirect evidence. Here, we explore the pressure dependence of the martensitic transition of lithium up to 7 GPa using a combination of neutron and X-ray scattering. We find a rather unexpected deviation from the extrapolated boundaries of hR3 phase of lithium. Furthermore, there is evidence that, above $\approx$ 3 GPa, once in fcc phase, lithium does not undergo a martensitic transition.

6.2 Introduction

Lithium is the simplest metal that undergoes temperature-driven martensitic transition [7, 29, 180, 87]. These are an important class of diffusion-less structural phase transitions that are integral to controlling the properties of steels and the design of many technologically important materials such as shape memory alloys. Because of its simple electronic structure, studies on the martensitic transition of lithium are of fundamental interest. Under ambient conditions, lithium is a nearly free electron system and has a bcc structure; however, the structures and electronic properties of lithium under compression deviate rapidly from a simple metal [75, 70, 155, 119, 160, 118, 172, 152]. Like all other alkali metals, lithium

undergoes a series of pressure-induced structural phase transitions to low symmetry phases, following an initial pressure induced transition from bcc to fcc phase at room temperature.

Whilst structures of lithium under pressure have been extensively studied, the mapped boundaries of the martensitic phase transition are limited to pressures below 3 GPa. In this region, lithium adopts the bcc phase at room temperature with a martensitic transition temperature (M_s) that increases with pressure at a rate of ($\frac{dM_s}{dP}_{P=0}$ =5 $\frac{K}{GPa}$) [180]. The low-temperature structure of lithium was initially identified to be hexagonal-close-packed [11] but later was shown to be samarium-type R-3 m H (166) structure (hR3) with 3 atoms per unit cell [7, 137, 158, 166, 112, 88, 128].

Lithium is a weak scatterer of both x-rays and neutrons, rendering scattering experiments only feasible in large facilities. Still neutron scattering is, in principle, more appropriate for structural studies of lithium, especially those at high pressure, as it combines a superior penetrating power with an improved scattering performance, when compared with x-rays, given the low atomic number of lithium. Yet, despite recent advances of neutron scattering in diamond anvil cells (DACs), these experiments remain challenging. Natural lithium is composed of 7 percent ^{6}Li, which has a neutron absorption cross section of 940 barn, thus requiring, for neutron studies, isotopically pure ^{7}Li (0.0454 barn), which is not commercially available. In addition, its softness and tendency to texture makes the production of both high quality fine powder or large single crystals of lithium extremely difficult, consequently limiting the quality of the structural data obtained, particularly inside a DAC as it requires very small samples. These limitations have led to an under-constrained low-temperature/high-pressure structural phase of lithium built mostly by extrapolation from higher temperature structural data or based on indirect evidence such as pressure dependence of its superconducting transitions [70, 172]. Earlier experiments only reported the superconductivity of lithium above $\approx$ 20 GPa with an initial positive and steep $\frac{dT_c}{dP}$. Later the superconducting phase diagram of lithium was revised with the discovery of ambient pressure superconductivity with T_c $\sim$0.4 mK [177] and lower boundaries of the superconducting phase transition under pressure shifted down to $\approx$ 16 GPa leaving an unexplored region of phase diagram for superconducting properties between ambient to 16 GPa [152]. Based on these results, it was suggested that the emergence of the pressure induced superconductivity of lithium is correlated with its structural boundaries at low temperature [172], with the fcc phase favoring superconductivity and the hR3 phase suppressing it. This, together with the higher temperature structural data leads to the conclusion that, akin to the bcc phase, also fcc lithium will undergo a martensitic phase transformation to the hR3

phase, extending the possible stability field of the hR3 phase to ≈ 20 GPa (or at least 16 GPa). It is thus clear that understanding the superconducting behavior and other low temperature properties of lithium as a function of pressure, relies first and foremost upon an accurate picture of its low temperature phase boundaries [7, 29, 87, 196]. In this study, we used state of art neutron and x-ray diffraction techniques under high pressure to expand the experimental phase diagram of lithium.

6.3 Results

6.3.1 Structural Analysis of Martensitic Transition

All structures were mapped by neutron scattering and x-ray angle dispersive diffraction at the SNAP instrument at the Spallation Neutron Source (SNS) and at HPCAT at the Advanced Photon Source (APS) respectively (Methods section). Figure 6.1 shows the revised phase diagram of lithium measured based in this study together with a selection of the data points previously reported by various groups. Figure 6.2 shows the equation of state (eos) of lithium at room temperature with neutron and X-ray, compared with previously reported curve for natural lithium. In Figure 6.3 we plot the low temperature eos of lithium at 80 K in which bcc and hR3 phases coexist. The presented data represents the first detailed high resolution structural analysis of the martensitic transition of lithium under pressure, including studies of the thermal hysteresis of the structural transformations (Figure 6.4). The observed bcc-hR3 phase boundary below 3 GPa is in agreement with those measured previously by Vaks et al. using acoustic emission method [180]. In a narrow pressure region between 2.5 GPa $\leq P \leq$3.5 GPa, the coexistence of a very small amount of hR3 with fcc and bcc phase is possible. Above 3.5 GPa, the bcc phase partially or completely converts to fcc, which remains to the lowest temperatures achieved.

6.3.2 Mixed Phases under Pressure

The phase fractions measured during each isobaric cooling show an increase in the percentage of fcc phase down to the lowest measured temperatures (Figure 6.5). On the other hand, the percentage of bcc phase decreases as result of isobaric cooling or during isothermal compression as it transforms into the hR3 and/or fcc structures. This suggests that only the bcc phase will convert to a fcc or hR3 phase and conversion of fcc to hR3 upon cooling or vice versa is not explicitly supported by the current experimental observations. Transition from bcc to hR3 is shown theoretically to be energetically favorable based on Hume-Rothery arguments [7]. However, similar arguments are not shown to apply similarly to support the transition of fcc phase to hR3 or another structure. Specifically, this is

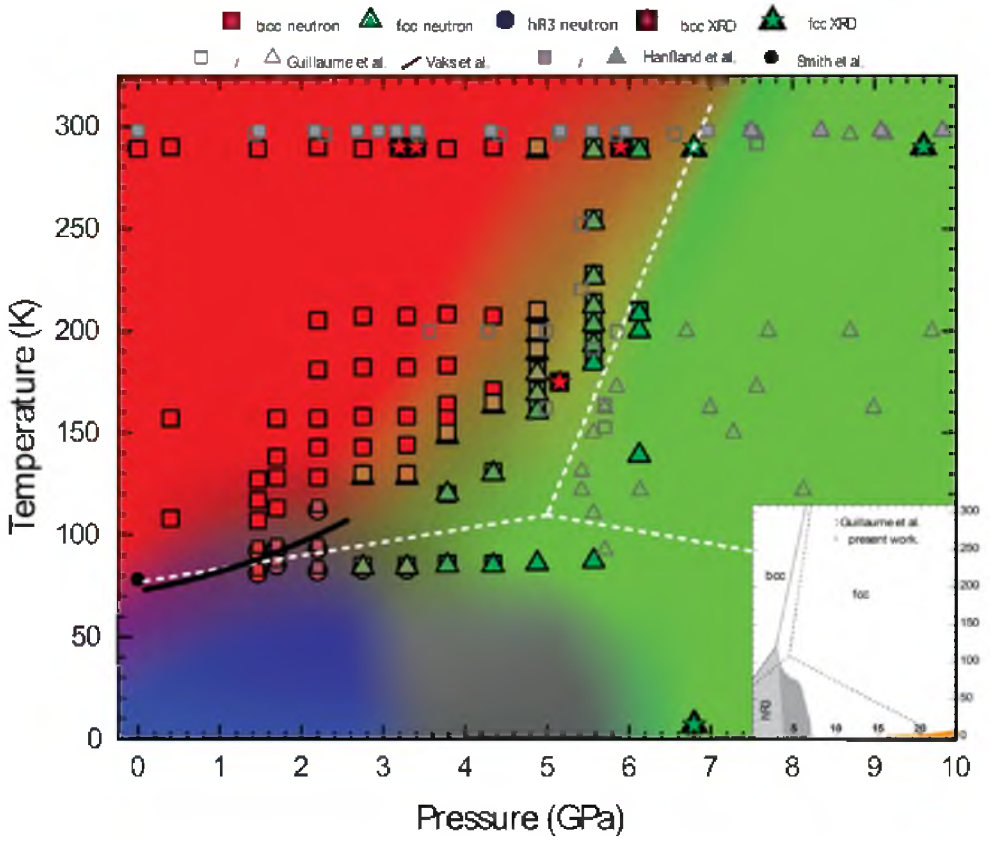

Figure 6.1. Phase boundaries obtained from data collected while cooling. Background shades are used to highlight the regions of the P-T phase diagram of lithium in which different structures are observed. Symbols designate different structures. Symbol overlap indicates the presence of mixed phases. The blue region here indicates two possibilities for the fcc/hR3 phase boundary, one boundary in which a transition from fcc to hR3 is not supported and one boundary drawing the upper limit. The inset shows the proposed structural boundaries of martensitic phase transition in lithium overlaid with previous reports. Orange region represents the superconducting region [160, 172, 152, 42].

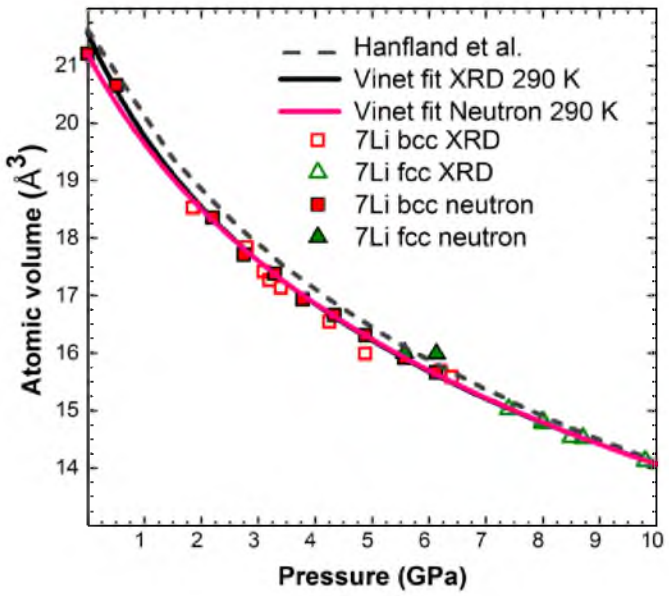

Figure 6.2. Equation of state for ^{7}Li measured at room temperature. Squares and triangles represent the experimental data points by neutron scattering and x-ray diffraction in bcc and fcc phase respectively. Open symbols are x-ray data. Dashed line is previously reported eos for natural lithium. Solid lines are Vinet fits to neutron and x-ray data.

seen in pressures above 5 GPa, at which the entire sample converts to fcc with moderate cooling; and upon further cooling, no indication of hR3 phase is observed down to the lowest achievable temperatures.

6.3.3 Complementary X-Ray Diffraction

Since achieving temperatures lower than ≈85 K is currently not possible in high pressure neutron studies, to further investigate the possibility of conversion from fcc to hR3, a complementary set of data at ≈7 GPa down to ≈7 K were collected using in-situ x-ray angle dispersive diffraction at APS. This measurement confirms that ^{7}Li is already in the fcc form at room temperature, and that remains the only observed phase down to ≈7 K, with no indication of any phase transition during cooling (Figure 6.4 d). These observations lead us to conclude that, once in fcc phase, ^{7}Li is stable in the pressure ranges studied and unlike what is known for the bcc phase, it will not undergo the temperature-driven martensitic phase transition. This confines the boundaries of the martensitic transition to pressures in which the bcc phase is still present and for a maximum of hR3 phase expected to not

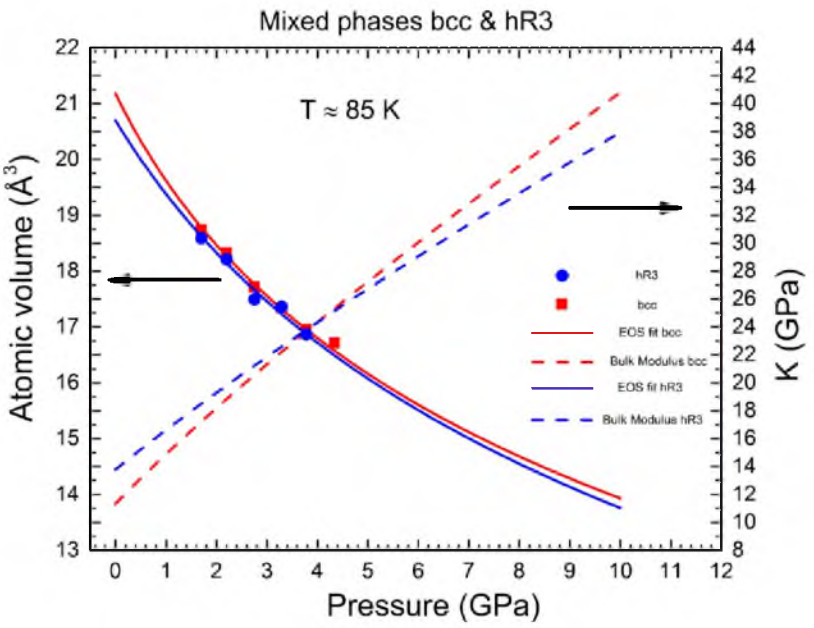

Figure 6.3. Equation of state and bulk modulus of lithium at 85 K. Equation of state fits and calculated bulk modulus ($K = \frac{dV}{dP}T$) for ^{7}Li at base temperature (∼80 - 85 K), in which bcc and hR3 phases coexist, form neutron data. Solid squares and circles are experimental data points of the present study in bcc and hR3 phase respectively.

exceed the proportion of bcc present at the lowest measured temperature (<15 % at 3.75 GPa and <10 % at 4.25 GPa). It is notable that this conclusion could not be made from the previously reported data alone, also that there is agreement in the regions in which the proposed phase diagram and previous works overlap.

6.4 Discussion

According to the previous phase diagram of natural lithium, in the fcc phase, $\frac{dM_s}{dP}$<0, there is a triple point near ∼110 K and ∼5 GPa (dotted line in Figure 6.1 inset). Should this be the case, several of the data points taken at the base temperature (≈85 K) above 3.5 GPa would show the presence of hR3 phase, which is not supported by the current experiments. Based on the updated phase diagram, the triple point is shifted to 115 K and 3 GPa. While in the neutron studies isobaric coolings, monitored via in-situ neutron scattering, have been used to build the proposed phase diagram; measurements on isobaric heatings were also measured performed at selected pressures (Figure 6.4). The martensitic transition temperature of lithium exhibits hysteresis and upon heating, the percentage of hR3 phase does not decrease up to 20 K above M_s (Figure 6.5). Furthermore, some fraction

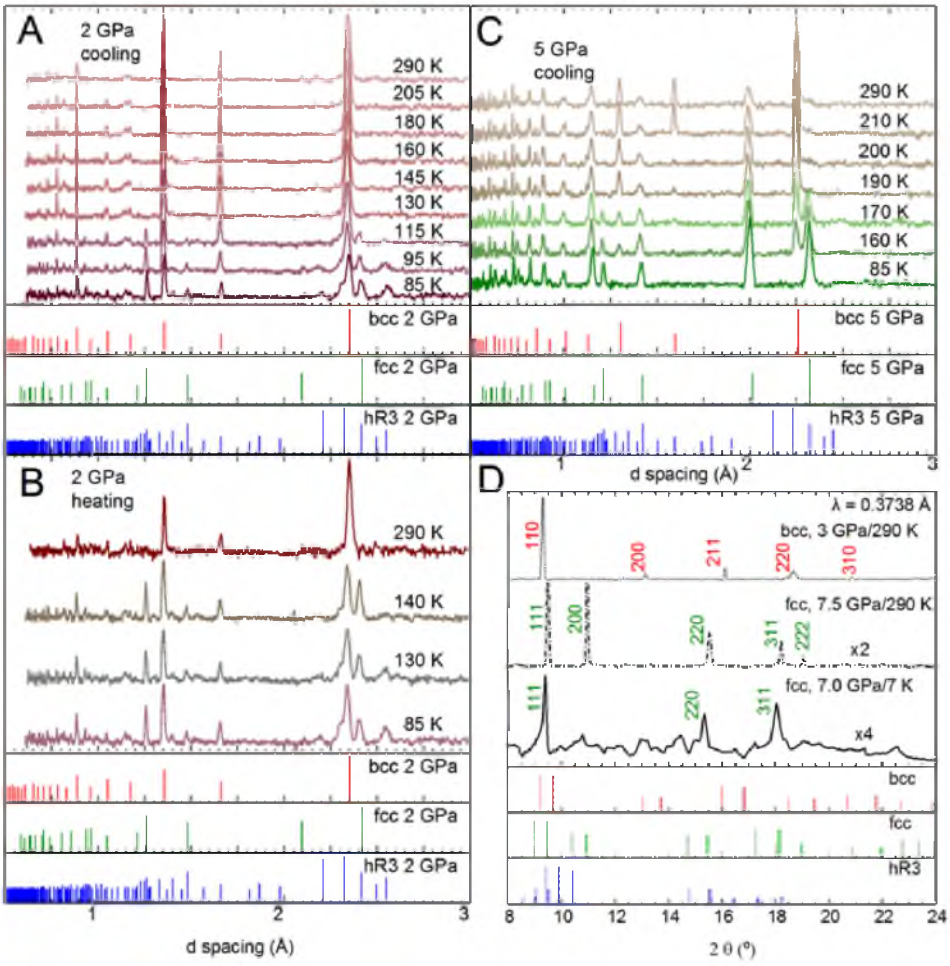

Figure 6.4. Diffraction signals from isotopically enriched ^{7}Li. A) and B) Neutron diffraction pattern of lithium at 2 GPa for cooling and heating respectively. The calculated peaks for the structures for this pressure are plotted below the spectra. The conversion upon cooling to hR3 is evident, and hysteresis is observed. The refined a lattice parameter for the bcc phase at room temperature is 3.323 ±0.002 Å, and at base temperature is 3.322 ± 0.002 Å. For the hR3 phase the calculated lattice constants at base temperature are a = 2.959 ± 0.004 Å and c = 21.726 ± 0.001 Å. C) The neutron diffraction at 5 GPa shows no indication of hR3 phase down to the lowest temperature. The lattice parameter a for the bcc phase at room temperature is 3.196 ± 0.001 Å, and for the fcc phase at base temperature a = 4.002 ± 0.003 Å. D) Structures of lithium at 3 and 7 GPa measured by x-ray in a DAC shows the presence of fcc phase to 7 K. Intensities are scaled for each data set. The dotted and solid lines show the location of the peaks at 3 and 7 GPa respectively.

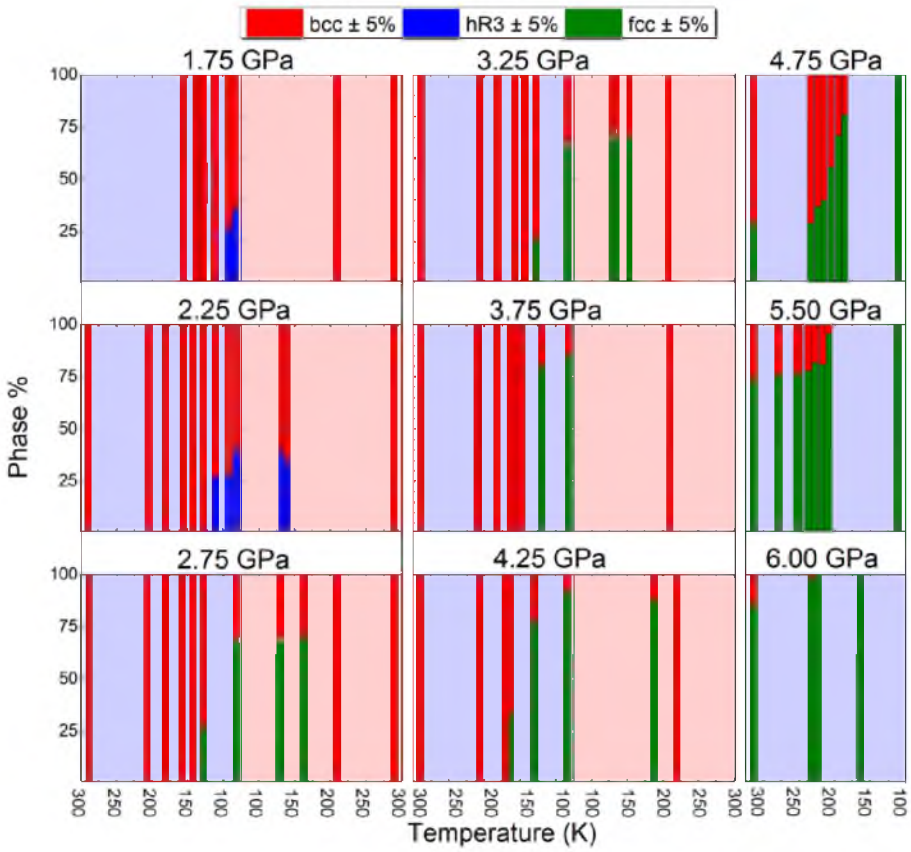

Figure 6.5. Phase fractions are presented in order during each isobaric cooling and subsequent heating. The gray area reported for 2.75 and 3.25 GPa are representative of areas with peaks of hR3 phase which appear as weak shoulders on characteristic bcc and fcc peaks. This could be indicative of a co-existence of bcc/fcc/hR3, or other phases. The slope of the hR3-fcc boundary in the region between 3.5 and 7 GPa below 80 K cannot be well defined by the current data. It should be noted, however, that at these pressures, once some percentage of the sample undergoes the transition to fcc, that percentage does not decrease upon further cooling to 80 K. This raises the possibility that bcc/fcc/hR3 co-exist in these pressure-temperature regions, and it is only the bcc that transforms to hR3, and the fcc percentage is stable or increasing upon cooling. It remains an open question if the transformation of fcc to hR3 upon cooling is possible.

of the hR3 phase is still observed, albeit at lower percentages, up to 30 K above M_s. This is consistent with the findings of Krystian and Pichl [96, 140] and Smith et al. [166, 167]. The hR3 phase can be visualized as a sequence of specific stacking of fcc and hcp and the difference in the free energy of fcc and hR3 phases even under ambient pressure is minute (≈1 meV, [75]). At pressures in the range between 2.5 GPa $\leq P \leq$3.5 GPa, bcc ^{7}Li cools into a possible mixture of three phases, dominated by a bcc/fcc mixture with the

possibility of hR3 phase also present. Interestingly, upon heating, the percentage of bcc present decreases while the fcc phase fraction grows, which may indicate the metastability of the hR3 phase in this regime, until the sample reverts back to the ambient temperature phase of 100 % bcc. Above 3.5 GPa, ^{7}Li cools into a bcc/fcc mixture, and upon heating, the bcc phase does recover but only above 20 K of the M_s upon cooling (e.g., 6.5, 4.25 GPa). This supports the previous reports by Krystian and Pichl [96, 140] and Smith et al. [166, 167] that lithium recovers from the martensitic transition into a mixture of bcc and hR3 phase with possible vestiges of fcc phase.

6.5 Summary

In summary, revised boundaries for the martensitic transition of ^{7}Li are presented. The proposed phase diagram demonstrates new features: a triple point (bcc/fcc/hR3) shifted to a lower pressure of ≈3 GPa; the low temperature boundary of the martensitic phase transition confined to pressures <5 GPa; and, up to 7 GPa, the fcc phase remains stable down to the lowest measured temperatures without indication of a martensitic phase transition. This opens the possibility for new structural boundaries of lithium below 80 K and at higher pressures, specifically where it was previously thought to be hR3, 7 GPa $\leq P \leq$20 GPa.

6.6 Methods

6.6.1 High Pressure Neutron Scattering Experiments

In-Situ diffraction patterns of a polycrystalline sample of 99.9 % isotopically pure ^{7}Li, were collected using time-of-flight neutron scattering at SNAP. The isotopically pure sample was enriched in ORNL allowing neutron experiments (these samples from the same batch were also used for later x-ray diffraction studies in a DAC). The data was collected using a neutron wavelength band centered at 2.15 Å, allowing access to Bragg reflections between 0.7 and 3 Å. Pressure was applied to the sample by means of a Paris-Edinburgh press fitted with cubic boron nitride anvils. Prior to loading in the press, the sample was sealed in a TiZr null scattering alloy gasket inside a helium glovebox to avoid exposure to atmospheric moisture. The sample was cooled via a custom-made liquid nitrogen cooling device connected directly to the anvils allowing measurements in the 83 K $\leq T \leq$320 K range. Complementary x-ray measurements on the same sample were done in HPCAT at 7 GPa from room temperature to 7 K in a diamond anvil cell (DAC). For neutron studies, pressure at each point was determined using the known equation of state (eos) of bcc lithium at room temperature [75, 2, 74]. The pressure was increased at room temperature and temperature dependent data

was taken on isobaric paths. Each pressure/temperature data point was collected in ≈50 minutes time exposure, after the sample reached thermal equilibrium. While martensitic transitions occur in short time scales, the long exposure time are necessary due to the weak coherent scattering cross section of lithium. At each pressure the sample was incrementally cooled to the base temperature (≈83 K). Additional datasets were collected upon heating to assess the hysteretic nature of the phase transitions. Following each temperature sweep, the sample was annealed to room temperature prior to a subsequent pressure increase. All the reported phases and transition temperatures used in assembling the proposed phase diagram were extracted from data collected while cooling.

6.6.2 High Pressure X-Ray Diffraction Experiments

To better define the boundaries of the martensitic transition, we acquired a supplemental set of data points on lithium using high resolution x-ray angle dispersive diffraction in a DAC. Lithium is a very weak x-ray scatterer and thus high pressure diffraction studies on its structures require high brightness, only accessible at a large facility such as the APS. These experiments were done using a 33 keV x-ray beam at the HPCAT beamline. A sample of lithium was coated with mineral oil, to protect the diamonds, with no other pressure medium. This was loaded in a DAC fitted with a rhenium gasket together with a small chip of NaCl as pressure marker. The initial data was collected at room temperature to confirm the bcc-fcc transition as a function of pressure. A new sample of natural lithium was pressurized to ≈3 GPa at room temperature, then transferred to a continuous flow liquid helium cryostat with 3" diameter Mylar windows and cooled to 7 K. Owing to thermal effects during cooling, the pressure on the sample increased to ≈5.1 GPa and 7.4 GPa at 175 K and 7 K respectively. The DAC was rotated by 20 degrees at a rate of 0.25 $\frac{deg}{s}$ and the data was integrated in 83 s exposure time. The pressure was determined using the eos of NaCl at each point [182, 40].

6.6.3 Structural Analysis

The known crystallographic information files of lithium from Inorganic Crystal Structure Database (ICSD) were used to identify the present phases of lithium [13, 135] at each pressure/temperature. Dioptas software v. 0.2.3 (2014) was used to analyze the x-ray data.

CHAPTER 7

FERMI SURFACE OF LITHIUM ISOTOPES

One of the open questions regarding the differences in the superconducting T_c's of lithium isotopes is whether those differences arise from structural or electronic differences. In order to investigate the electronic properties, the Fermi surfaces of lithium isotopes were measured at ambient pressure.

Whilst the Fermi surfaces of the alkali metals are thought to be be nearly spherical, far from the boundaries of the first Brillouin Zone, and conventionally the amount of distortion increases as one moves down the column of the periodic, lithium is actually a notable exception to that trend [36]. The amount of distortion calculated for lithium is actually more than that of Na or K [36]. The calculated Fermi surface of lithium is also quite large when considering the low temperature phase, calculated not to touch the edges of the first Brillouin Zone at ambient pressure but to do so under pressure [72, 72](note, this reference from 1962 used hcp as the low temperature structure of lithium as that reported by [10]). This indicates a possibility that whilst lithium is indeed a simple metal (with only one conduction electron), its electronic structure at low temperatures may not be so simple in practice.

This chapter describes measurements of the Fermi surfaces of lithium isotopes, and the motivation and experimental setup are discussed; however, the results or discussion of the specific results are not included, as they have not been previously published. The work described in this chapter was carried out in collaboration with S.W. Tozer, W. Coniglio, D. Graf, and J.H. Park at the National High Magnetic Field Laboratory (NHMFL) in Tallahassee, FL, USA. Z. Jiang assisted with the crystal growth of lithium isotopes at the Deemyad Laboratory in the department of Physics and Astronomy at the University of Utah. A. Arif performed the single crystal diffraction in the department of Chemistry at the University of Utah. Data were collected by S. Deemyad, A.M.S. Richards with assistance in experimental setup by D. Graf and W. Coniglio; however, those unpublished

data are not presented here. The experimental design was outlined by S. Deemyad in the proposal for use of the 18 T superconducting magnet in the Millikelvin division of the NHMFL. FFT analysis was performed by S. Deemyad and A.M.S. Richards using Igor Pro software; effective mass and dingle temperature fits were performed by A.M.S. Richards using Origin Pro. L. Balicas and D. Graf provided guidance and discussion regarding the analysis, results, and interpretation. The flat bottom Mo crucible was machined by W.B. Talmadge, and the plunger by A.M.S. Richards.

7.1 Abstract

This work investigates the Fermi surfaces of lithium isotopes. Whilst lithium is often considered to be a simple metal, there is much about this element that is currently not well understood. This is especially the case for the low temperature properties of lithium, where the phase transition from bcc to hR3 phase causes experimental difficulties. In order to achieve decent measurements of quantum oscillations, through either the de Haas van Alphen effect or the Shubnikov de Haas effect (see sections 1.8 and 2.5), high quality single crystals and low temperatures are required. The martensitic phase transition from bcc to hR3 poses a difficulty since a single crystal of the bcc phase may not remain a single crystal at temperatures below the martensitic transition temperature ($M_s \approx 80$ K). For this reason, all previous measurements of the Fermi surface of lithium have been in the bcc phase. This would be the first measurements of the Fermi surface single crystal lithium indicated to be in the low temperature hR3 phase as well the first measurements of three different isotopic compositions of lithium. The measurement of the Fermi surface of single crystal lithium is necessary in order to determine whether the Fermi surface touches or even passes the boundary of the first Brillouin Zone.

7.2 Introduction

The size and topology of the Fermi surface of a metal determine its electronic properties. Lithium, amongst the other alkali metals, with one conduction electron, has been thought to have a nearly spherical Fermi surface far from the boundaries of the first Brillouin Zone. Previous measurements of the Fermi surface of lithium [144, 145, 44, 134]; however, investigated lithium in the bcc phase, intentionally suppressing the martensitic transition, either at high temperature, using positron annihilation, or at low temperature, by means of the de Haas van Alphen Effect. This study is the first to investigate the Fermi surface of single crystal lithium in the low temperature hR3 phase. In light of the results from Chapter 5 regarding the anomalous superconducting isotope effect in dense lithium, three

different isotopes of lithium were studied in this work. The isotopes of lithium were studied by means of the de Haas van Alphen effect at temperatures ranging from ≈350 mK to 2.5 K and magnetic fields up to 18 T. The angular dependence of the quantum oscillations as well as Dingle temperatures and effective masses were also investigated. The results show a distortion from a spherical Fermi surface in the angular dependence, especially in the lightest isotope of lithium. The results also do not indicate that cubic symmetry is present, implying that the sample is in the hR3 phase. However, the size of the Fermi surface found is to be very close to that reported by Randles and Springford [144, 145]. Whilst this would be very far from the boundaries of the first Brillouin Zone if lithium was in the cubic bcc phase, in the hR3 phase, this size Fermi surface is nearly the same size or possibly greater than the shortest axis of the first Brillouin Zone of the hR3 phase.

7.3 Method

Detection of de Haas van Alphen oscillations in metals generally requires high quality single crystals and low temperatures [161]; however, this can prove problematic in the case of lithium. Lithium undergoes a temperature-driven phase transition at ambient pressure from bcc to hR3 [10, 166, 13]; this transformation may introduce stacking faults and defects which can interfere with the detection of de Haas van Alphen oscillations [144]. Previous de Haas van Alphen measurements of lithium were conducted on powder dispersions of lithium in order to suppress the martensitic transformation and therefore reports were limited to the maximal distortion from a sphere of a bcc-lithium Fermi surface [144, 145]. In this work, single crystals of the stable isotopes lithium were prepared and the angular dependence of the de Haas van Alphen oscillations in the hR3 phase were investigated with the effective masses of the electrons and the Dingle temperatures.

7.3.1 Single Crystal Growth

The single crystals of lithium were prepared by means of a modified method from [131] (Figure 7.1). Lithium is a very compressible metal and highly prone to texture that generally prefers the single crystal state over a fine powder. However, the low density, high surface tension, and chemical reactivity of lithium make the use of a typical crucible with a nucleation tip on the bottom problematic [131]. To address the chemical reactivity of lithium, all crystals were grown inside in a dry argon atmosphere and a crucible with a flat bottom was machined from molybdenum (Figure 7.2). Due to the low melting temperature of ambient pressure lithium, it is possible to heat the crucible past the melting point of lithium using a standard hot plate. The low density of lithium implies that most of the

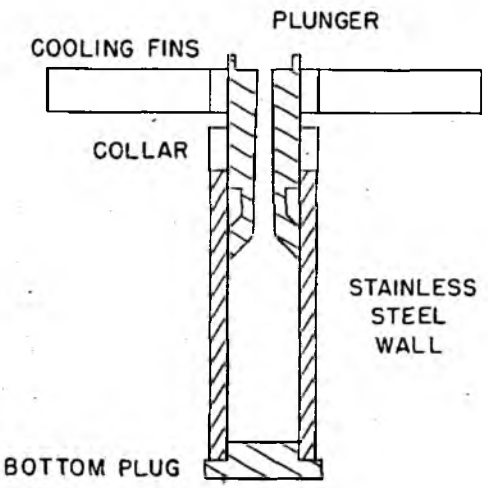

Figure 7.1. Design by Nash and Smith [131]. A stainless steel crucible is heated with a hot plate and it is lined with petroleum jelly to prevent reaction between the lithium ad the steel. The lithium melt forms an ingot in the crucible and the plunger is applied to the melt. The nucleation occurs at the top from the temperature difference of the cooling wings.

impurities therein will sink in a lithium melt; it is assumed that the best results will be obtained by providing a nucleation site from the top of the melt as in [131]. A plunger, similar in design to [131], was machined from molybdenum. The bottom forms a cone and a through hole of 200 μm was drilled with an electric discharge machine. The crucible is first lined with mineral oil to prevent the lithium from sticking to the sides, and the lithium is melted to form an ingot. Due to the high surface tension of lithium, the shape upon melting is well preserved and in order to form an ingot that conforms to the shape of the crucible, a small amount of pressure is applied to press the molten metal into shape. This was found to be most the efficient method over vibration of the crucible and stirring of the molten metal, and the vibration required to overcome the surface tension is quite intense and the probability of the lithium sticking to the stirrer is quite high. In general, the lithium is melted inside the crucible and the preheated plunger is placed on top. The melt is kept for 1 hour to give impurities time to sink and then the plunger is deployed downward until a bead of molten lithium forms at the top of the plunger. In order to clear as many impurities as possible, the ingot of lithium would undergo many meltings and resolidifactions with the bottom of the ingot physically cut with a steel scalpel blade at each iteration. This was done on the assumption that the impurities settle in the bottom. Once the lithium ingot is properly prepared, it is melted and the preheated plunger deployed until a bead of the

Figure 7.2. Modified crucible used to grow single crystals of lithium. Crucible and plunger are machined from Mo. The hole in the plunger was made using an EDM; the hole is $\approx$ 500 μm and tapers to $\approx$ 200 μm hole at the top. The size of the crucible is $\approx$ 0.75 cm.

desired size forms at the top of the plunger. A steel scalpel blade lined with mineral oil is used to cut the bead from the remainder of the melt and then it is cooled at a rate of $\approx$2 K per minute. The resultant bead of lithium forms a single crystal of a spherical shape.

The process of pushing the molten lithium through the plunger serves several purposes: one, it removes any residual impurities that may reside on the surface of the molten metal; two, it provides a means of placing a portion of the melt farther away from the heat source, providing a thermal gradient and a nucleation site; and three, it breaks the surface tension of the melt allowing the melt to crystallize in arbitrary orientation not affected by the remainder of the melt. However, this process leads to an unusual spherical shape. It should be noted here that the crystals produced in [131] were the shape of the crucible, as in a casting, and they were physically cut off to expose a face. In this modified method, the crystals are not constrained as outside physical structures as they solidify and so the only constraint on the shape is forced by the surface tension itself. The metal retaining its spherical shape as it crystallizes can be understood if one considers the Gibbsian dividing surface (λ) to be narrow, and much smaller than the radius, R, of the molten bead (λ <R) [61]. In this case, the high surface of the lithium allows for a large molten bead to form and remain stable, which in turn makes the condition λ <R possible, and the result is single crystal (confirmed using XRD, see Figure 7.3) that is, at least macroscopically, spherical.

While this method reliably produces clean, high quality single crystals, it does not allow for reliable indexing. The XRD data collected show sharply defined single crystal peaks;

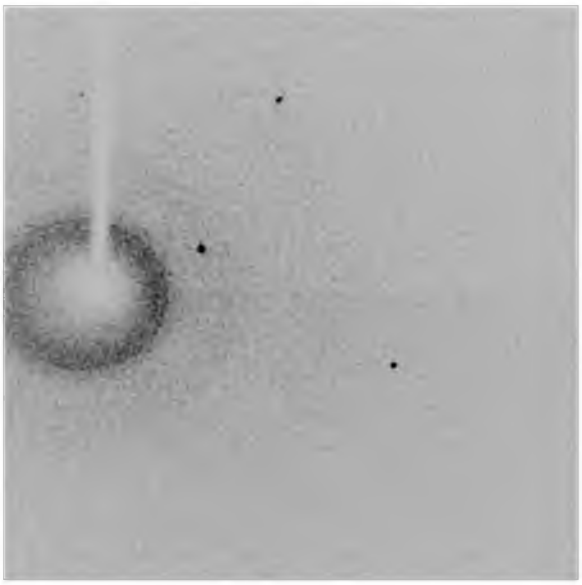

Figure 7.3. X-ray diffraction pattern from a Bruker system of single crystal lithium. The diffraction image shows clear single crystal spots.

however, overall appearance of the crystal itself does not allow for repeatable orientation along a face.

7.3.2 Data Collection

Single crystal of natural lithium (99.99 % lithium is 92.41 % by atomic weight ^{7}Li and 7.59 ^{6}Li; 0.01 impurities Na, Mg, Al, and other elements; Sigma Aldrich), isotopically enriched ^{6}Li (99.99 % lithium with the isotopic composition 95.6 ^{6}Li and 4.4 ^{7}Li with the same impurities as natural Li: Sigma Aldrich), and isotopically pure ^{7}Li (99.9 % ^{7}Li) provided by Oakridge National Laboratory were prepared in this manner. All magnetic measurements were made at the NHMFL in Tallahassee Florida. The de Haas van Alphen quantum oscillations were measured by means of torque magnetometry using piezo-electric cantilevers (outlined in section 2.5.1, shown in Figure 7.4), in an Oxford, top loading liquid ^{3}He cryostat with a working base base temperature of ≈350 mK and a superconducting magnet with a maximum field of 18 T. Several field sweeps were performed at varying angles in order to determine any angular dependence of the oscillations. Due to the high frequency of the oscillations reported in [144], ≈41,250 T, field sweeps were performed at the relatively slow rate of 0.04 $\frac{T}{minute}$ and over a range of 16.75 to 18 T in order to resolve the data. The collected data of the field sweeps were analysed by applying a Fast Fourier Transform (FFT) to solve for the frequency of the oscillations. Each FFT was applied

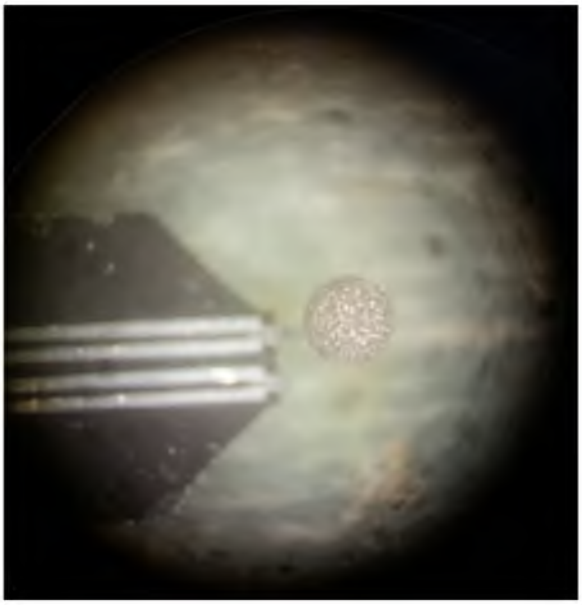

Figure 7.4. Lithium crystal on cantilever. The crystal is noticeably quite large (>400 μm) in order to compensate for the low mass of lithium.

over the same range of magnetic field (16.75 to 18 T). The temperature dependence of the oscillations were also recorded at several angles to fit for the effective masses of each of the isotope compositions of lithium. Also, the field dependence to fit for the Dingle temperature was collected at one angle as well.

7.4 Dingle Temperature

To confirm the quality of the single crystals used in this work, the Dingle temperature was measured for all isotopic compositions of lithium. The Dingle temperature is determined by fitting the function:

$$R_D = e^{\frac{\alpha r m^* T_D}{B}} \tag{7.1}$$

where $\alpha = \frac{2\pi^2 k_B m_e}{e\hbar} = 14.69\frac{T}{K}$, $r = 1$, m^* is the effective mass (see section 7.5), and R_D is the amplitude of the oscillations. This parameter accounts for electron scattering in the crystal by accounting for the reduction in the amplitude of oscillations as a function of inverse field. The Dingle temperature, T_D,

$$T_D = \frac{\hbar}{2\pi k_B \tau} \tag{7.2}$$

includes the relaxation time, τ, of electrons in the material. As the Dingle temperature is inversely proportional to the relaxation time, a low Dingle temperature indicates a long

relaxation time, indicating fewer scattering sites in the crystal (i.e., higher purity or quality material) by the mean free path of the electrons l:

$$l = v_F \tau \tag{7.3}$$

where the Fermi velocity $v_F = \frac{\hbar k_F}{m^*}$.

In each case, the Dingle temperature was low; however, it is possible that the crystal quality of the different isotopes differed slightly. This raises the question of where the amount of mixed isotopes may affect the crystal growth process.

7.5 Effective Mass

The effective mass is determined from the relation:

$$R_T = \frac{\alpha r m^* T \frac{1}{B}}{sinh(\alpha r m^* T \frac{1}{B})} \tag{7.4}$$

where again $\alpha = 14.69 \frac{T}{K}$, $r = 1$, R_T is the amplitude, and m^* is the effective mass:

$$m^* = \hbar^2 (\frac{d^2 E}{dk^2})^{-1} \tag{7.5}$$

The previously reported values for the effective of lithium (natural lithium) is 1.8 $\pm$ 0.4 $\frac{m^*}{m_e}$ [144]. We measured the effective mass for the three different isotope compositions and, as with the Dingle temperature, found an indication that the isotopic purity may have greater influence than the isotopic composition. Though the values measured in this work differ enough from the literature value to be outside of the calculated error, one possible explanation for this discrepancy is that the present measurements are for single crystals, and there could exist orientations which lead to an average over all orientations of 1.8 $\frac{m^*}{m_e}$. Also, in [144], the dispersion was meant to suppress the martensitic transformation, to preserve the bcc phase. In the present work, there was no such attempt to suppress the martensitic transformation and from the angular dependence data, the symmetry is not assumed to be cubic.

7.6 Discussion

In previous works regarding the de Haas van Alphen oscillations of Alakli metals, either evidence of cubic symmetry is found in the Fermi surface or from the preparation of the samples, it is assumed [144, 145, 101, 48]. From the angular dependence measured in all three isotopic compositions of lithium, there is no direct evidence of cubic symmetry; even with arbitrary crystal orientation, rotation of >180 degree would reveal cubic, four-fold

symmetry if present. This indicates that the lithium crystals in this work are in the hR3 phase, and not the bcc. It is also notable that when considering the size and shape of the Brillouin Zone of the hR3 phase of lithium, the size of the Fermi surface measured in [144, 145] would be much closer to the boundaries of the first Brillouin Zone. While the nearly free electron model for bcc lithium indicates a nearly spherical Fermi Surface that extends to $\approx \frac{1}{2}$ the crosssection of the first Brillouin Zone, after the lithium has undergone the martensitic transformation to hR3, the first Brillouin Zone is now much shorter along the c-axis, and the extremal area of the measured Fermi surface may now lay close to the boundary.

Deviations from a spherical Fermi surface measured in this type of experimental setup may have several different explanations. While it may be possible that Fermi surface is more distorted from a sphere in the hR3 versus bcc phase, there are some caveats which must be addressed. Unless structures of the single crystals are measured at a temperatures below ≈80 K, the idea of defects or twinning of the single crystal forming as a result of the Martensitic transformation cannot be ruled out. This is a difficult condition to meet, as facilities capable of measuring the structure of nonreacted lithium (i.e., kept in an airtight container) are rare, as are facilities capable of achieving high magnetic fields. This makes the reaction of small lithium crystals more likely to occur in transit. It is also possible that the timing of the experiments may be problematic. It may be possible that the crystals experienced more or less defects as a result of the martensitic transformation in the first cooling than the second, or that the process of multiple coolings and heatings worked the crystals into a higher or lower quality single hR3 crystal in later runs. However, it would be possible (though somewhat time consuming) to measure the Dingle temperature in every cooling. There is also the possibility that some isotopic purities or compositions are more prone to defects forming during the Martensitic transformation.

As far as the sizes of the Fermi surfaces are concerned, we would expect ^{6}Li to have a slightly smaller Fermi surface than the heavier isotopes, due to the lattice constant in real space being slightly larger [35].

Considering the primitive vectors of the reciprocal lattice of the hR3 phase:

$$\begin{aligned} b_1 &= \frac{2\pi}{a}[\frac{2}{\sqrt{3}}\hat{x} + \frac{\sqrt{3}}{9\sqrt{2}}\hat{z}] \\ b_2 &= \frac{2\pi}{a}[-\frac{1}{\sqrt{3}}\hat{x} + \hat{y} + \frac{\sqrt{3}}{9\sqrt{2}}\hat{z}] \\ b_2 &= \frac{2\pi}{a}[-\frac{1}{\sqrt{3}}\hat{x} - \hat{y} + \frac{\sqrt{3}}{9\sqrt{2}}\hat{z}] \end{aligned} \tag{7.6}$$

with the $\frac{c}{a}$ ratio being close to the ideal for close packing ($9\sqrt{\frac{2}{3}}$) [185]. For the sides of the Brillouin Zone, the distance is $\approx 2.36 \times 10^{10}$ inverse meters. A Fermi surface near the size measured by [144, 145] would make the Fermi surface actually rather close to the boundaries of the Brillouin Zone, especially in the case of the lightest isotope ^{6}Li. However, that is assuming a circular cross section, it could be distorted and necking out to touch the Brillouin Zone edge. The determination of low frequencies associated with necking can be measured experimentally, though it would require much higher magnetic fields.

A fair comparison of the sizes is complicated somewhat by current lack of ability to properly orient the lithium crystals with respect to the applied magnetic field. Again, low temperature structural analysis would have to done to find the crystal orientation of the sample. Then the crystal would have to have to transform in the same manner upon at least one subsequent cooling (unless *in situ* structural measurements were possible in the high magnetic field).

7.7 Conclusion

The quantum oscillations of lithium isotopes can be measured by means of the de Haas van Alphen effect through torque magnetometry and meaningful information can be found by comparing the different isotopic purities and compositions of lithium. Differences in these results could indicate that either the isotopic purity or composition of the samples lead to different amounts of distortion, twinning or faults from the temperature-induced martensitic phase transformation, or actual differences in the Fermi surfaces.

These results may also indicate that the Fermi surface is much closer to the boundaries of the first Brillouin Zone than was previous thought. This has some implications for the assumption that the hR3 (Figure 7.5) phase suppresses superconductivity [14, 185, 7, 8, 177]. As these experiments can show the first measurements of the electronic properties of lithium isotopes at low temperatures in the hR3 phase, further measurements are implied. High quality, low temperature measurements of the crystal structures of single crystals of lithium are required to confirm that a crystal which begins as a single crystal in the bcc remains as a single crystal after the Martensitic transformation. The measurements of the Dingle temperature indicate high quality crystals; however, a more direct determination of the quality and structure of the crystal is indicated. Also, further measurements regarding the effect of the amount of isotope purity are very interesting in regards to this study. In short, is it the mass of the isotope or the amount that is cause for the measured differences? Another way to approach that question would be to study the ambient pressure superconductivity of

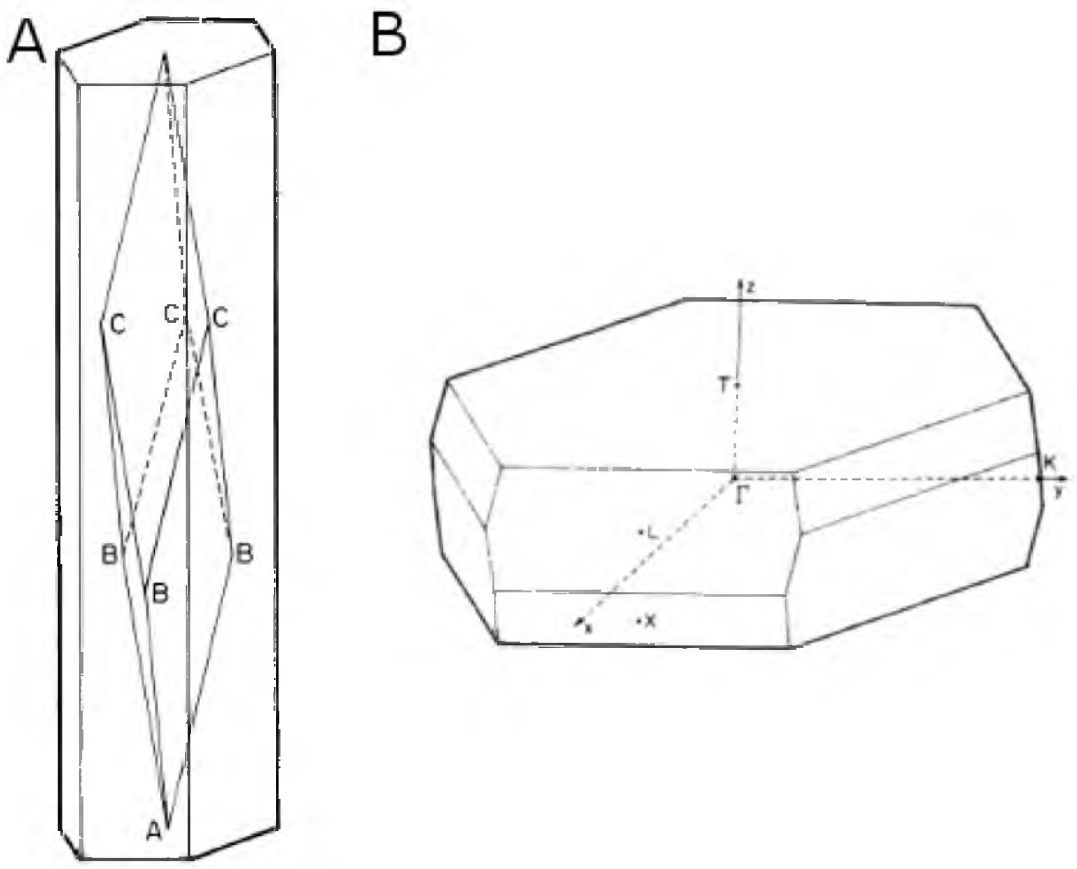

Figure 7.5. The two ambient pressure phases of lithium. A) The unit cell of the low temperature hR3 (or 9R) phase. B) The first Brillouin Zone of this phase.

different isotopic compositions of lithium. This is, however, not a trivial matter considering the very low T_c of ambient pressure natural lithium [177]. It would provide much insight into the possibility of differing degrees of contact between the Fermi surfaces of lithium isotopes and the boundaries of the first Brillouin Zone.

CHAPTER 8

SUPERCONDUCTIVITY OF $BALI_4$ UNDER PRESSURE

A possible means of enhancing the superconducting T_c of lithium was explored through chemical means. Lithium was combined with barium, one of the few elements with a lower electro-negativity, in an effort to increase the electron density. Lithium and barium, both with a low electro-negativity, are generally an electron donor when compounded with other materials. These two materials form an intermetallic compound when combined [164]; this compound, $BaLi_4$, is lithium-rich, thus having a relatively low mass, and was hoped to have improved electronic density of states which would in turn enhance the T_c according to the McMillan expression 1.14, $T_c = 1.14(\frac{\hbar\omega_D}{k_B})e^{\frac{-1}{N(E_F)V_{eff}}}$.

Experimental setup design was provided by S. Deemyad and A.M. Schaeffer (Richards). Sample synthesis was carried out by M.C. Delong, W.B. Talmadge, and Z.W. Anderson, with direction and equipment provided by S. Guruswamy. Coils for AC magnetic susceptibility were provided by W.B. Talmadge. Resistance, AC Magnetic susceptibility measurements, and analysis were completed by A.M. Schaeffer. Manuscript was written by S. Deemyad, A.M. Schaeffer, and W.B. Talmadge, with input from M.C. Delong, Z.W. Anderson, and S. Guruswamy.

Reprinted with permission from Journal of Physics Condensed Matter, Deemyad, S., DeLong, M.C., Talmadge, W.B., Anderson, Z.W., and Guruswamy, S. 2013. Pressure Induced Superconductivity of $BaLi_4$, *Journal of Physics: Condensed Matter* , 25, 375701. Minor changes were requested made at the request of the committee and the University of Utah Thesis Office.

8.1 Abstract

We studied the pressure-induced superconductivity of $BaLi_4$ up to 53 GPa by means of electrical resistivity in a diamond anvil cell. Superconductivity in $BaLi_4$ is first observed at a pressure of 5.4 GPa with a T_c of 4.5 K. Below 2 GPa, superconductivity is not observed

for temperatures down to the minimum temperatures achievable in the current study which is 2 K. Between 5.4 GPa and 12 GPa, T_c increases steeply to its maximum value of 7 K. Above 12 GPa, the pressure dependence of T_c is complex and the sign of $\frac{dTc}{dP}$ changes several times up to the maximum pressure studied of 53 GPa.

8.2 Introduction

Enhancement of properties of metals by alloying them with other metals is a technique that has been used from the earliest stages of human history. Prior to the discovery of superconductivity in MgB_2, with T_c = 40 K [127], it was widely thought that the superconducting transition temperature by electron-phonon coupling mechanism is limited to 30 K [121]. Superconductivity in MgB_2, which was confirmed to be a phonon-mediated superconducting system [79], restored interest in compounds of low atomic number (Z) elements. Lithium is the lightest metallic and superconducting element. Due to its light mass and metallic behavior, several compounds of lithium have been predicted and studied for superconducting properties (e.g., [39, 99, 53, 98]). At ambient pressure, lithium becomes a superconductor below 0.4 mK [177]. This value is orders of magnitude lower than the theoretically predicted T_c of ≈1 K by ab initio electronic structure calculations and the McMillan expression [147]. This low T_c is attributed to several factors such as the reduced electronic density of states at the Fermi surface in the hR3 phase of lithium [7], and/or the suppression of superconducting T_c due to spin fluctuations [37]. Under high pressure, lithium reaches one of the highest transition temperatures of elemental superconductors [42, 160, 172]; $^{max}T_c$=14-20 K. Alternatively, by chemical modification, it may be possible to synthesize a lithium-rich compound in which a high superconducting transition temperature is achieved through electronic enhancement. Studying the superconducting phase diagram of lithium-rich compounds can provide insight to finding ways to enhance the superconductivity by chemical modification. None of the alkali earth metals that are miscible with lithium at ambient pressure (Ca, Sr, and Ba) are superconducting at one atmosphere; however, all become superconductors under high pressure [143, 194, 47, 150]. While calcium reaches the highest T_c (29 K at 216 GPa [150]) of any elemental superconductor, barium has a lower critical pressure of superconductivity than either calcium or strontium. Barium has complex pressure-dependent structures [84, 107, 90, 133] and becomes a superconductor above 3.7 GPa with T_c= 60 mK [143, 194, 47, 193]. The transition temperature of barium increases to about 5.3 K at 18 GPa and then smoothly decreases to ≈4.5 K at 43 GPa, which is the highest pressure at which its superconductivity has been studied.

Presence of a minimum in a melting curve, indicative of lattice instabilities and presence of soft phonon modes, in many cases is correlated to an enhancement of superconductivity [56]. The melting curve of barium reaches the lowest melting temperature of all alkali earth metals in all studied pressure ranges ($^{min}T_m$ ≈400 K) [82] and its melting temperature decreases in the pressure range of 1.5 to 8 GPa, which coincides with the onset of pressure-induced superconductivity in the same pressure range. Lithium itself has a very unusual melting curve which also exhibits a drastic decrease in its melting temperature under pressure [155, 98, 15, 110], as well as a sequence of symmetry-breaking structural phase transitions under pressure [70, 75]. The minimum of the melting curve of lithium occurs at the phase boundary of fcc/hR1/cl16. This structural phase boundary at low temperature coincides with maximum temperature of lithium's superconductivity [42, 160, 172]. Lithium forms two binary compounds with barium, and both are rich in lithium: $BaLi_4$ (Figure 8.1) and $Ba_{19}Li_{44}$ [165, 164]. These compounds have large unit cells and complex structures at ambient pressure. In $BaLi_4$, the compound crystallizes in the hexagonal space group, $P6_3/mmc$ (194) with 24 lithium and 6 barium atoms per unit cell (Figure 8.1). Lithium atoms form Li12 icosahedral cages centered on another lithium atom. The cages are connected with additional lithium atoms, each is surrounded by 6 barium atoms, all together forming a hexagonal pattern [164]. The band structure and electronic properties of such a structure are complex and superconductivity can have a nonintuitive pressure dependence. The questions are: a) if the superconducting properties of either of the parent elements are improved in $BaLi_4$, and b) where the Cooper pairs are in such complex materials. In this paper, we have experimentally investigated the superconductivity of $BaLi_4$ from ambient pressure to 53 GPa in a diamond anvil cell apparatus and pursued the possibility of enhancement of lithium's superconducting properties by chemical modification

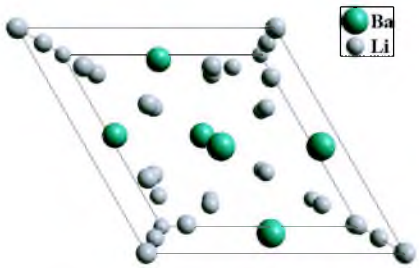

Figure 8.1. Unit cell of BaLi4, $P6_3/mmc$ (194)hexagonal, a = 9:1875 Å, c = 9.1875 Å, $\frac{c}{a}$ = 1:0000, V = 671.62 $Å^3$, Z = 2 [164].

with barium.

8.3 Experiment

$BaLi_4$ has been previously synthesized and its structures have been refined by x-ray studies [164, 183]. We used the synthesis procedure from the latest studies [164], summarized here; Stoichiometric proportions of lithium (99.9 % purity, Alfa Aesar, Na main impurity) and barium (99 % purity, Sigma Aldrich, Sr main impurity) were measured, with better than 1 % precision of the weight ratio of the components, inside a high purity argon glove box and were mixed together. The mixture was placed in a molybdenum crucible and sealed under a low pressure argon atmosphere inside a Pyrex ampoule using an oxy-acetylene torch. The sample then was melted at a temperature of 620 K for ten days followed by slow cooling to room temperature at a rate of 1 $\frac{K}{hr}$ in a Thermolyne 30400 oven. The ampoule was transferred to the argon-filled glove box and the appearance of $BaLi_4$ was consistent with description provided by published data [164]. The resultant compound is a polycrystalline sample which is brittle, and xenomorphic in appearance (macroscopic the appearance is determined from the grains rather that the crystal). This is in stark contrast to pure lithium and barium, both of which are soft, very pliable metals. The sample was ground in a tantalum crucible to fine size particles for several hours and was sealed in a $\approx$1 cm^2 area by 2 μm Mylar film covered glass slide. X-ray powder diffraction studies at ambient pressure were performed in a Philips X-Pert X-Ray Diffractometer with a Cu anode. The diffraction pattern collected in 1.5 hours was consistent with the diffraction pattern of $BaLi_4$ from refined crystal structure of $BaLi_4$ by Smetana et al. [164].

All high pressure data were taken inside a diamond anvil cell (DAC). Superconductivity was determined by the sudden drop in resistivity, measured by means of an AC resistivity technique by either quasi-four probe or exact four probe, built on an insulating gasket (Figure 8.2). A test of bulk superconductivity in the sample was also done at 12 GPa where the maximum T_c was observed in the resistivity experiment. It was assumed that $BaLi_4$ may react with diamonds similar to pure lithium, and the DAC was prepared as outlined in previous high pressure studies on lithium [155]. In order to better compare the superconducting versus pressure curve of $BaLi_4$ from that of barium (see section 8.4), the T_c of barium was measured in the same setup.

All data were taken in five isobaric runs, inside a temperature-controlled liquid ^{4}He cryostat (Janis SVT-200). Pressure was determined from fluorescence of several ruby spheres distributed across the sample chamber, before and after each pressure data. Temperature

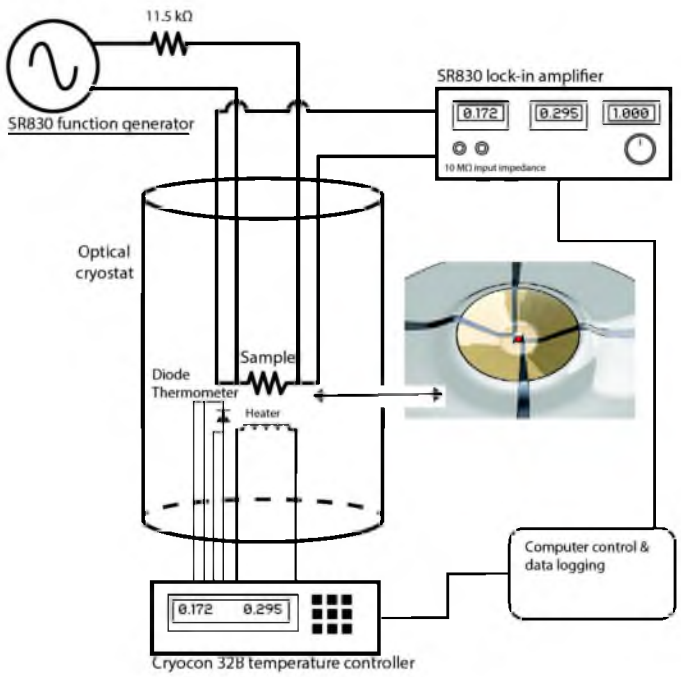

Figure 8.2. AC resistivity measurement setup. Inset shows the arrangement of the leads in quasi-four probe measurement.

was measured using a diode thermometer, thermally anchored to the DAC close to the sample.

8.4 Results

Superconductivity was measured in $BaLi_4$ from ambient pressure to 53 GPa. The resistance as a function of temperature was recorded for both cooling and heating. Due to better temperature control, the onset of T_c is determined from the heating curves in all cases (Figure 8.3). In high pressure experiments, especially nonhydrostatic experiments which are an inherent part of resistivity experiments, large pressure gradients in the sample chamber are unavoidable; thus, a broadening of the superconducting transition is present. In the pressure regions where the T_c is monotonically increasing, the onset of the transition is a good representation of the T_c of the sample at maximum pressure. In the pressure regions of monotonically decreasing T_c, the scenario is just the opposite. We have shown in all data the onset and the end of each transition. In all cases, the accuracy in temperature determination is ± 0.1 K, determined from the sharpness of the onset of the transition. Superconductivity down to lowest temperature accessible in our setup (2 K) was not observed at ambient

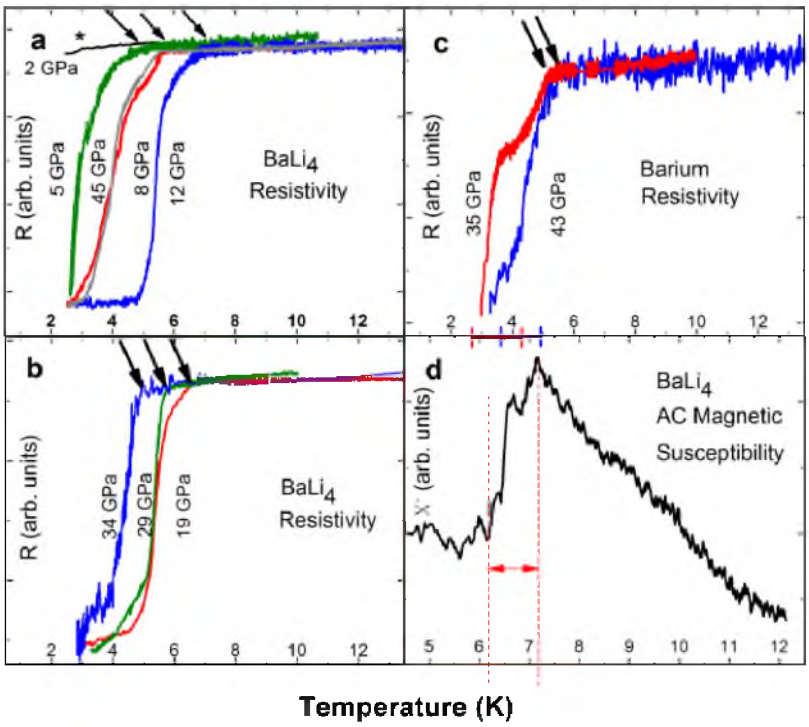

Figure 8.3. Resistivity as a function of temperature for selected data points. The size of the transition in different runs depends on sample size. In the graphs above, all data have been scaled to show the same size transition for comparison. Arrows indicate the onset of T_c. Resistivity curves a), b) are for $BaLi_4$, the asterisk near the 2 GPa curve is a possible onset of a superconducting transition near 2.5 to 2 K. The resistivity curves in c) are for barium at 35 and 43 GPa. Red and blue bars indicate the upper or lower bounds of T_c as defined by [47]. The curve in d) is the data point taken at 12 GPa by the AC magnetic susceptibility method. The ratio of the residual resistivities at ambient pressure is $\frac{R(297K)}{R(5K)} \approx 14$ and samples were showing metallic behavior throughout all pressure runs.

pressure and 2 GPa.

Superconductivity first appears at 5.4 GPa, with a T_c of 4.5 K, then monotonically increases to a maximum at of 7 K at 12 GPa. The onset of the pressure-induced superconductivity, determined by extrapolation, is shifted to lower pressures than barium and the maximum T_c in $BaLi_4$ is higher by ~2 K (there is a weak indication of possible superconductivity in $BaLi_4$ sample at 2 GPa shown by an asterisks in Figure 8.3 part a). After reaching the maximum, the T_c decreases at a shallower slope until 4.7 K at 37.5 GPa. At higher pressures, a second increase in T_c was observed, reaching a second maximum of 5.5 K at 45 GPa, after which the T_c begins to decrease once more up to 49 GPa. A third, very slight increase in T_c under pressure from 49 GPa to 53 GPa was observed;

however, the diamond failed before the pressure could be confirmed after warming up the sample and this data point is not conclusive. The resistivity curve of barium at 35 GPa and the resistivity of $BaLi_4$ at 8 and possibly 29 GPa showed double step like drops in resistivity at T_c (Figure 8.3). This double step transition is sharp and is different from pressure broadening effects and can be due to structural phase transitions occurring in the given pressure ranges. Different coexisting phases near the structural phase transitions can exhibit different superconducting critical temperatures which lead to a double transition.

The phase diagram of $BaLi_4$ varies from that of elemental lithium [42, 160, 172]. $BaLi_4$ does not reach a maximum T_c close to that of lithium, 14 - 20 K; however, it begins to superconduct at a much lower pressure, 5.4 GPa versus 20 GPa; it also reaches a maximum T_c at a lower pressure, 12 GPa versus 30 GPa. The superconducting phase diagram of barium [47, 125] is more similar to that of $BaLi_4$. The overall similarity of the shape of the T_c versus pressure graph of $BaLi_4$ to elemental barium prompted a closer look at the T_c of barium at high pressure. The T_c of $BaLi_4$ and barium differ most distinctly in the lower pressure range, where $BaLi_4$ first becomes a superconductor (Figure 8.4). However, in the pressure range above 32 GPa, the two appear to become more similar; from 32 to 38 GPa, the T_c are within error of each other. To elucidate the comparison between $BaLi_4$ and barium (Figure 8.5), two data points for barium were taken at pressures of 35 and 43 GPa. We found no inconsistencies with previous studies [47]. We slightly extended the known superconducting phase diagram of barium, analyzing in the same manner as Dunn and Bundy [47].

While $BaLi_4$ shows a distinct reemergence of superconductivity in a small pressure range above 40 GPa, any evidence of a reemerging phase in barium is not conclusive. Barium overall shows a rather flat decline in T_c [47] from 5.3 K at 18 GPa to 4.2 K at 38 GPa; at 43 GPa, the T_c increases slightly to 4.4 K. However, due to the differences in the definition of T_c, this evidence is hardly compelling. When defining the upper limit according to Dunn and Bundy [47], the T_c decreases from 5.3 K at 18 GPa to 4.7 K at 35 GPa, then increases again from 4 to 9 K at 38 GPa to 4.6 K at 43 GPa. From 35 to 43 GPa, all these data are within error of each other. The presence of a second superconducting phase is not ruled out, the data are within error bounds, and there is not a strong enough indication to draw a conclusion.

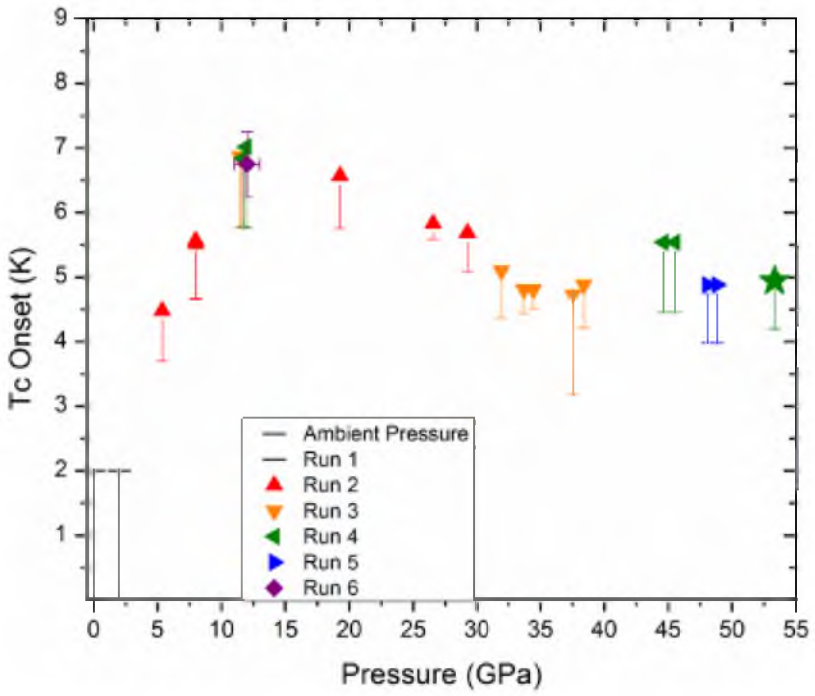

Figure 8.4. Superconducting phase diagram of $BaLi_4$. The data represent the T_c onset, determined by the change in slope of the resistance as a function of temperature. The symbols show the first instant of of the change in slope and the lower error bar marks the end of the change in the slope. The pressures are determined from measuring 3 ruby pressure markers at each pressure. The x-axis error, which are not clearly visible, are determined by the standard diavation of the measured pressure markers. The data point at 53 GPa, marked by a star, remains unconfirmed due to the diamond failing before the pressure was confirmed after heating. The data point in run 6 (12 GPa, 6.9 K) is taken by the AC magnetic susceptibility method.

8.5 Discussion

The similarities in pressure dependence of superconductivity in $BaLi_4$ and pure barium may suggest the possibility of presence of nonreacted barium forming a percolated superconducting path. This possibility is examined and excluded based on the following tests and analysis: The percolation threshold for formation of complete barium superconducting path is ≈25 % [192, 149]. The resistivity of the sample at its superconducting transition drops to less than $\frac{1}{6}$ of the value right before the transition in the worst case; this implies presence of over 20 % of barium in the sample which is only possible at the cost of a similar amount of nonreacted lithium with much higher superconducting T_c, which was not observed here. In addition, to exclude the possibility of the presence of a large amount of barium in a single grain, we have used five different pieces of samples in different runs and confirmed similar

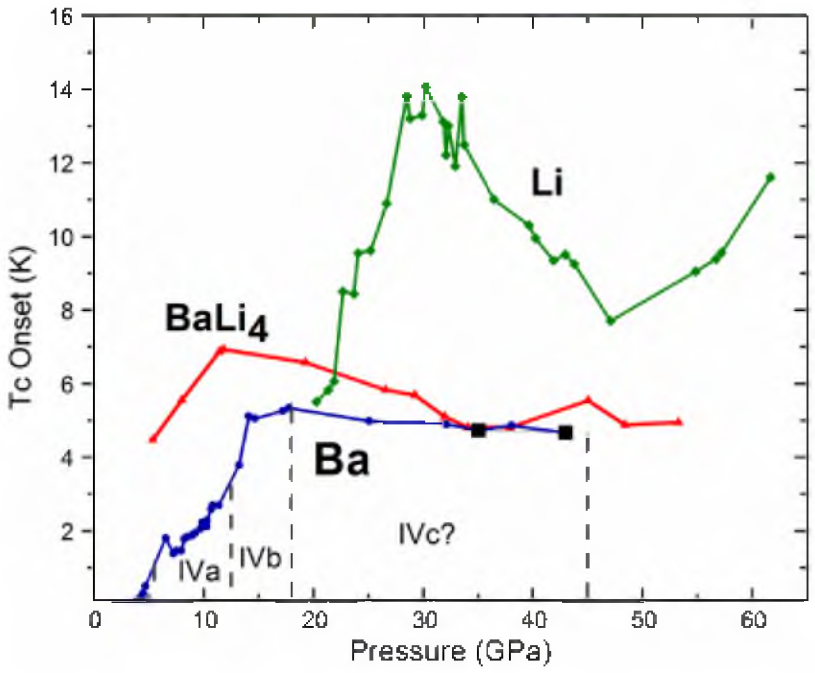

Figure 8.5. Superconducting phase diagram of $BaLi_4$ (this study) in comparison to elemental lithium [42] and barium [47, 125]. The dashed lines mark the structural phase boundaries of barium [133]. Black squares show the superconductivity of barium that was measured in the current study for better comparison of the superconductivity of barium and $BaLi_4$.

superconducting behavior for all of them (Figure 8.4). Finally, we have used the technique of AC magnetic susceptibility to confirm the bulk superconductivity in our sample at 12 GPa, where maximum T_c of 7 K was observed in electrical resistivity measurements, and found consistent results. According to the phase diagram here, it is plausible to argue that a distorted barium sublattice is the major contributor to the superconductivity in $BaLi_4$ up to 37 GPa. At ambient pressure, Ba-Ba distance in $BaLi_4$ is slightly increased compared to pure barium lattice (4.35 Å in barium to ≈4.55 to 4.6 Å in $BaLi_4$ [84, 164]).

Since lithium has higher electron affinity than barium at ambient conditions, the enhancement of T_c in $BaLi_4$ compared to pure barium is likely a lattice effect caused by the presence of lithium rather than an electronic effect. It is notable that at ambient pressure, the bonding energy of barium 3d5/2 peak in $BaLi_4$ is shown to be very close to metallic barium, whereas Li's 1s emission is decreased by 1 eV in $BaLi_4$ compared to pure metallic lithium [103]. This is attributed to the electronic rearrangement of lithium in the $BaLi_4$ lattice, while the electronic properties of barium remain, similar to metallic barium at ambient pressure.

Barium has a rich structural phase diagram from ambient pressure to 90 GPa [84, 107, 90, 133]. Barium undergoes a pressure-induced phase transition from bcc to hcp around 5.5 GPa [90], which is relatively near, yet somewhat above, the onset of its superconducting phase transition. Barium has an hcp structure from 5.9 to 11.4 GPa, phase II, then another hcp phase from 45 to 90 GPa, phase V [90, 133]. The T_c of barium increases monotonically throughout the phase I to the phase III region, until it reaches its maximum of 5.3 K at 18 GPa. This pressure, as well the region in which barium and $BaLi_4$ are the most similar, lies within the boundaries of barium's phase IV, which consists of a series of complex host-guest structures (Ba–IVa, b, c, etc.) and persists over a wide pressure range from 12.6 to 45 GPa [107, 133]. It has been noted in [107, 133] that the host structure appears to be stable over the wide pressure range while the guest changes. The loose analogy to the structure of ambient pressure $BaLi_4$ would be the barium sublattice being the guest, and the lithium sublattice being the host. Compared to barium, the lithium sublattice has a complex structure in $BaLi_4$ and its contribution to superconductivity may also lead to a complex pressure dependence at higher pressures.

The structures of $BaLi_4$ under pressure have not yet been studied and the complex pressure dependence of superconductivity in this material may be associated either with a sequence of structural phase transitions of one or both sublattices, or drastic changes in electronic structures under compression. The absence of superconducting transition temperatures above 7 K, in the superconducting phase diagram of $BaLi_4$; however, excludes the possibility of a pressure-induced phase separation of this compound to elemental barium and lithium in the pressure range of this study.

8.6 Conclusion

In summary, $BaLi_4$ is shown experimentally to exhibit pressure induced superconductivity above 5.4 GPa. The complex pressure dependence of superconductivity in $BaLi_4$ suggests a sequence of changes in the structures, or the electronic properties of this material. Detailed structural analysis at high pressure shed light on the superconductivity in $BaLi_4$. Our experimental results show a close relation between the superconductivity of barium and $BaLi_4$, and could provide insight for finding new superconducting intermetallic materials with higher $T_c's$ at ambient pressure. Extending the present experiments to higher pressures may result in the emergence of new enhanced superconducting phases in which lithium plays a dominant role.

CHAPTER 9

SUMMARY

This work has looked at several features of lithium, from the melting curve of dense lithium to the Fermi surfaces of lithium isotopes at ambient pressure. This is in an effort to confirm whether or not lithium demonstrates quantum solid properties.

9.1 Results and Discussions

In Chapter 3, it was found that whilst there was a maximum and subsequent minimum in the melting curve, the lowest temperatures of the minimum were not low enough to conclude quantum effects are the cause. The alkali metals, including Li, Na, K, and Rb, all exhibit maximums and minimums in there melting curves [65, 70, 100, 110, 155, 130]. However, in the case of the heavier alkali metals, this can be explained by the series of symmetry-breaking phase transitions [132, 75, 65, 130, 4]. All of these alkali metals are in the bcc phase at ambient pressure, then undergo a transformation to fcc with increasing pressure. It is in the fcc phase that the maximum in the melting curve lies. Whilst bcc and fcc are highly symmetric phases, and fcc is a fairly close packed phase, a further increase in pressure leads to slower symmetry and less efficiently packed phases. The melting curve of lithium from Chapter 3 [155] is consistent with the trend of lithium transforming from the closely packed fcc phase to the lower symmetry, less efficiently pack hR1 or cI16 phase. The region from $\approx$10 GPa to $\approx$40 GPa in which the melting temperature T_m is decreasing is consistent with the concept that the liquid phase is more dense than the solid phase. In other words, as the lithium loses symmetry with pressure, the liquid phase becomes more efficiently packed that the solid.

It is possible that lithium does indeed exhibit quantum melting (see section 1.5.1); however, the experiment described in Chapter 3 does not provide a conclusive answer regarding the dominance of quantum mechanical effects, such as zero-point energy over classical effects. In order to answer such question with more certainty, it was decided to look at the isotope effects in dense lithium. Specifically, we looked at low temperature

properties of dense lithium isotopes, an effect that occurs at low temperatures, in which thermal energy ($\propto K_B T$) would not be likely to play a dominate role. The McMillan expression for superconducting T_c (1.14) shows a distinct expected isotope effect for BCS type superconductors, $T_c \propto m^{-\alpha}$ with α typically equal to $\frac{1}{2}$.

However, in order to measure any differences between the isotopes with the necessary precision, it is necessary that the samples with the same thermal history be measured simultaneously under pressure. The expected isotopic shift in the T_c of lithium isotopes would be proportional to roughly $\sqrt{\frac{7}{6}} = 1.08$, with the T_c of the lighter stable isotope of ^{6}Li having a greater value than the heavier isotope ^{7}Li (or even natural Li which is $\approx$ 92 % ^{7}Li). This would mean, if lithium followed the expected isotope effect, then the normal pressure gradient inside the DAC would easily mask the slight shift found. This required development of a method to measure the T_c's of two samples inside the same DAC simultaneously in order to resolve the slight differences.

This method is outlined in Chapter 4, in which an experiment measuring the T_c's of two samples of YBCO with different stoichiometries were measured using a method modified from [162, 153] to measure the electrical resistance of both samples simultaneously. The success of this method allowed for the execution of the comparative measurement of the superconductivity of dense lithium isotopes (Chapter 5).

The results of Chapter 5 show that dense lithium has quite anomalous isotope effects, at least in the range of 16 to 26 GPa as measured in the work [152]. Between pressure 16 to 21 GPa, rather than seeing a small shift of ^{6}Li to a higher T_c, ^{6}Li shows a significantly higher T_c, 5.4. However, at pressures above 22 GPa, the isotope effect reverses, showing instead an inverse isotope effect. The fact that the trend of T_c changed within the pressure range studied implies that there is a significant difference between the isotopes under pressure. Whilst this study cannot conclude what the cause of the anomalous superconducting isotope effect can be, it does imply that lithium is indeed not following the classical model. There is the open question of whether the lithium isotopes both undergo the same phase transitions as a function of pressure, whether the phase diagrams of both isotopes are the same, shifted, or are there perhaps phases of one isotope which are not present in the other. Another possibility is that there are different electronic structures of the different isotopes. Whilst these are two obvious possibilities to account for the anomalous superconducting isotope effect, either one of these possibilities is not congruent with classical models.

A highly detailed investigation of the low, or at least relatively low temperature, phases of lithium appears to be necessary after the results of Chapter 5. Besides the startling

isotope effect, another expected result was a lower pressure of the onset of measurable (>2 K) superconductivity. Whilst the literature values of superconductivity of lithium under pressure [42, 160, 172] all agree that the onset of T_c >4 K is near 20 GPa, the work in Chapter 5 showed a slightly lower T_c ($\approx$ 3 K) from 16 to 20 GPa, then a sharp increase in T_c with increasing pressure. It was at this point reasonable, in the absence of any structural data below 77 K, to extrapolate the boundary of the martensitic phase of lithium to 20 GPa as seen in the phase diagram proposed by [70]. It has been assumed the martensitic phase of lithium (hR3) may suppress superconductivity and account for the anomalously low ambient pressure T_c of lithium [14, 185, 177, 7, 8]. Given that this temperature of ambient pressure superconductivity in lithium is far below what a standard table-top experiment can achieve (requiring sub-millikelvin temperatures), experiments to map the superconducting T_c of lithium from ambient pressure to 16 or 20 GPa are not feasible at this time. This led to extrapolations that the sudden increase in T_c near 20 GPa may be related to a phase transition near that pressure; taking the results of Chapter 5 into account, perhaps a phase transition occurs closer to 16 GPa or lower.

Whilst the phase diagram of Guillaume et al. [70], mapped using XRD, beautifully maps several isotherms of lithium from ambient pressure to >120 GPa, there is a paucity of data near the extrapolated triple point, and no data set published therein was identified at hR3. In order to more accurately map the boundaries of the hR3 phase, the experiment described in Chapter 6 was performed mostly using a relatively large volume of sample in a Paris-Edinburgh press and neutron diffraction. As the scattering potential of a material for neutron diffraction experiments is not proportional to the number of electrons in the sample, even low Z materials are possible to study with great precision. Isotopically pure ^{7}Li was used, since ^{6}Li has a very large absorption; even though it does not have a particularly large cross section, the use of a null scattering gasket and rather long exposure times allowed us to obtain very detailed, high quality structural data of ^{7}Li from $\approx$300 K to $\approx$80 K and ambient pressure to $\approx$ 6 GPa. These data allowed us to not only see the phase transitions in ^{7}Li (the martensitic phase transition from bcc to hR3, and the diffusive phase transition from bcc to fcc), but to also see the mixtures of two or even three phases. The detail of this work, in addition to some complementary XRD data at much lower temperature ($\approx$10 K at 7 GPa), allowed us to conclude that the boundary of the hR3 phase exists at much lower pressures than previously thought. Our evidence also suggests that the fcc phase of lithium at the pressures and temperatures studied is very stable, and a transformation from the fcc to the hR3 is not supported. This conclusion implies that while a phase transition

may be responsible for the sharp increase in T_c near 20 GPa, or possibly the onset of superconductivity >2 K at 16 GPa, this phase transition is *not* hR3 to fcc.

Since neutron diffraction is not possible with ^{6}Li, this experiment was simply unable to make any sort of conclusion regarding the isotope effect. It did, however, challenge previous extrapolations regarding structures of lithium at high pressures and low temperatures. Of course, the boundaries of the martensitic phase were not the only assumptions regarding lithium. Another place to search for isotope effects in lithium is the electronic properties. The two isotopes, having the same electronic configuration and electronic density of state, ought to have nearly identical Fermi surfaces (the slight differences in the sizes of the unit cells, ^{6}Li being slightly larger, was expected to make a proportionally sized difference in the Fermi surface). The mass of the core nuclei is not expected to play a large role in the shaping of the Fermi surface.

As an alkali metal, with only one conduction electron (and very low electronic density of states), lithium is thought to have a nearly spherical Fermi surface far from the boundaries of the first Brillouin Zone. Li has been calculated to have a somewhat more distorted Fermi surface than the other, heavier alkali metals, Na and K; this was attributed to very small core of Li ions ($1s^2$) and the conduction electron being generally closer to the core (this would effectively make the wave function more distorted from a free-electron wave function) [36]. However, previous measurements of the Fermi surface of lithium were limited to the bcc phase [144, 145, 44, 134]; these studies were either conducted at higher temperatures, using positron annihilation, or using dispersions of lithium powder sealed in wax to suppress the low temperature phase. Whilst this does provide much useful information regarding the electronic structure of bcc lithium, in order to better understand the low temperature effects of lithium, a natural conclusion is to study the low temperature phase.

An experiment was conducted to investigate the low temperature quantum oscillations of lithium isotopes at ambient pressure in order conclude if any significant differences between the isotopes exists (even without the application of pressure). What we found was that were indeed some very interesting differences between the isotopes, including the Fermi surface of the ^{6}Li being slightly large and more distorted than natural lithium, or the isotopically pure ^{7}Li. Since the lattice of ^{6}Li is slightly larger than that of the other two isotopes, this results was somewhat surprising since we would have expected the Fermi surface to proportionally smaller. This result confirmed that the boundaries of the first Brillouin Zone of ^{6}Li are mostly likely closer, if not touching, the Fermi surface. If the boundaries of the first Brillouin Zone do touch touch the Fermi surface of ^{6}Li at ambient pressure,

since the Fermi surface is large, it may touch the boundaries at lower pressures that other isotopes (possibly related to a lower onset of superconductivity >2 K). A greater amount of distortion in the measured Fermi surface of a lithium isotope could always be due not only to a truly more distorted surface, but also could be an effect of the single crystal possibly twinning or otherwise turning polycrystalline as an effect of the martensitic transform. The natural lithium sample also showed some distortion, which could also be due to effects of the martensitic transformation. However, the isotopically pure sample exhibited very little distortion from a sphere. Measurements of the Dingle temperatures of all three samples confirmed high quality crystals, even though low temperature XRD confirmation was not possible. The measurements of the Dingle temperature also confirmed that the isotopically pure ^{7}Li crystal was the highest quality. This could imply that it may not be only the isotopic composition itself that affects the behavior of the sample, but also the isotopic purity (since the ^{6}Li sample still contains 5 % ^{7}Li, and the natural lithium is only 92 % ^{7}Li). This is further supported by the measurements of the effective mass of the isotopes, with the ^{6}Li and natural lithium sample having effective masses of the electron nearly equal to each other and the effective mass of the electron for the ^{7}Li sample being different enough to lay outside the calculated error.

Whilst the maximal distortion measured in this experiment is not objectively large, it is more surprising that the overall size of Fermi surface is very close to what was measured for bcc lithium (despite the lack of four-fold rotational symmetry indicating that no sample remained in a cubic phase). The size of the Fermi surface would not be close to the boundaries in the bcc phase; however, the hR3 phase has a significantly different BZ, including a much shorter c* axis. This makes it very possible that the Fermi surface may actually touch the first BZ boundary, especially at the short axis. This would imply that perhaps the hR3 does not suppress T_c as much as previous thought, and the T_c could increase steadily with pressure until it is measurable at >2 K at 16 GPa. Also, the larger Fermi surface of the lighter isotope ^{6}Li implies that it may have a T_c even at ambient pressure, and perhaps a steeper onset of pressure-induced increasing T_c.

Chapters 3 through 7 are primarily concerned with addressing the question of whether or not lithium is consist with a quantum solid model. The melting curve offered no conclusive evidence; however, through the superconducting isotope effect, some anomalous effects that would be incompatible with a classical model were found. Chapter 6 found that the boundaries of the martensitic phase must be shifted to a lower pressure and temperature. Also, the fcc phase appears at low temperatures in ^{7}Li appears at much lower pressures than

previous thought, meaning the emergence of the fcc phase is not related to the emergence of superconductivity >4 K near 20 K. Chapter 7 has found some interesting differences in the Fermi surfaces of different isotopic compositions of lithium. The results therein indicate that Fermi surface of the lightest isotope of lithium is the largest and possibly crosses the boundaries of the first Brillouin Zone. Also, this isotope has more in common with natural lithium than it has with the isotopically purified heaviest isotope of lithium, indicating that perhaps the amount of isotopic purity plays a role in the isotope effect along with isotopic composition.

Chapter 8; however, has a slightly different goal. In this chapter, the focus was not so much to show the dominance of quantum mechanical behaviour over classical behaviour, but instead was an attempt to increase the T_c of lithium through chemical means. Whilst low mass materials should have a high T_c according to the McMillan equation, 1.14 ($T_c = 1.14(\frac{\hbar\omega_D}{k_B})e^{\frac{-1}{N(E_F)V_{eff}}}$), a more dominant term in this expression is the electronic density of states at the Fermi level($N(E_F)$). Lithium was combined with barium, a material with an even lower electro-negativity than lithium in an effort to combine lithium with a material that would donate electrons to the lithium. The resultant material, $BaLi_4$, is still lithium-rich, to remain relatively light and was hoped to have a high electronic density of states.

It was found in this work [154] that the superconducting phase more closely resembled an enhanced version of barium rather than lithium. By comparing the structure of $BaLi_4$ at ambient pressure to the structures of barium under pressure, many similarities are apparent. This could perhaps account for $BaLi_4$ having a lower onset of T_c >2 K than pure barium and a slightly higher maximum temperature. In this case, it appeared as though compounding barium with the lighter lithium atoms allowed for a lighter overall mass of the compound and perhaps less stiffening in the lattice, enhancing phonon-coupling and in turn the T_c.

9.2 Conclusion

This dissertation represents experimental work, the primary purpose of which is to present evidence in the form of results from controlled laboratory conditions. The goal is to present the results in the proper experimental context. In an experimental work, demonstrating the process of investigation requires detailing the experimental procedures used. These procedures not only must be explained in order to interpret the results, but also in order to allow other experimentalists to recreate the experimental conditions and possibly confirm (or refute) the results. The highest quality scientific results are only capable of demonstrating the behaviour of a particular sample under a particular set of experimental

procedures. These results are only interpretable with a thorough understanding of the experimental techniques and the methods used to produce them.

A detailed description of experimental techniques and methods are arguably the most important and relevant pieces of any experimental work. Any results achieved in a work are directly contingent upon the experimental plan, techniques, and methods. Perhaps the greatest strength of the scientific method is that it is a method, not an ideology. Many results reported in the literature are later shown to be false [81]. And yet, the scientific method is arguably the most successful human invention despite most results being 'wrong'. It is incongruous to force scientific results into a false dichotomy as either 'right' or 'wrong'.

An historical example is that of (Lord Kelvin) William Thomson's calculation of the age of sun and earth [89]. Thomson undertook the task in order to demonstrate that earth could not be as old as claimed by geologists and biologists since they did not understand thermodynamics [176]. One hundred fifty years later and after the discovery of heat from radioactive decay, we know the age of the earth to be billions of years older than Thomson predicted (much closer to the estimates based on geologic evidence alone). The importance of the example is not that Thomson was 'wrong' regarding the age of the earth, but rather than he chose not to consider evidence presented by entire fields of study. This is an example of the scientific process failing. Even if Thomson had calculated the age of the earth to be billions of years, this work still would have contributed anything more than a cautionary tale to the scientific literature. The process of scientific investigation is the most relevant feature of any scientific work, not the result.

My goal is to present my experimental works with the process clearly defined so that these experiments can hopefully be recreated and improved upon. Overall, whilst this work has no definite conclusion as to quantum solid properties of lithium, it is hoped that this study will stimulate further investigation in this field.

APPENDIX

COLLECTED NEUTRON SPECTRA

This appendix shows all of the collected neutron data that was discussed in Chapter 6. The figures are presented in the same order in which the data were collected.

A.1 Neutron Spectra

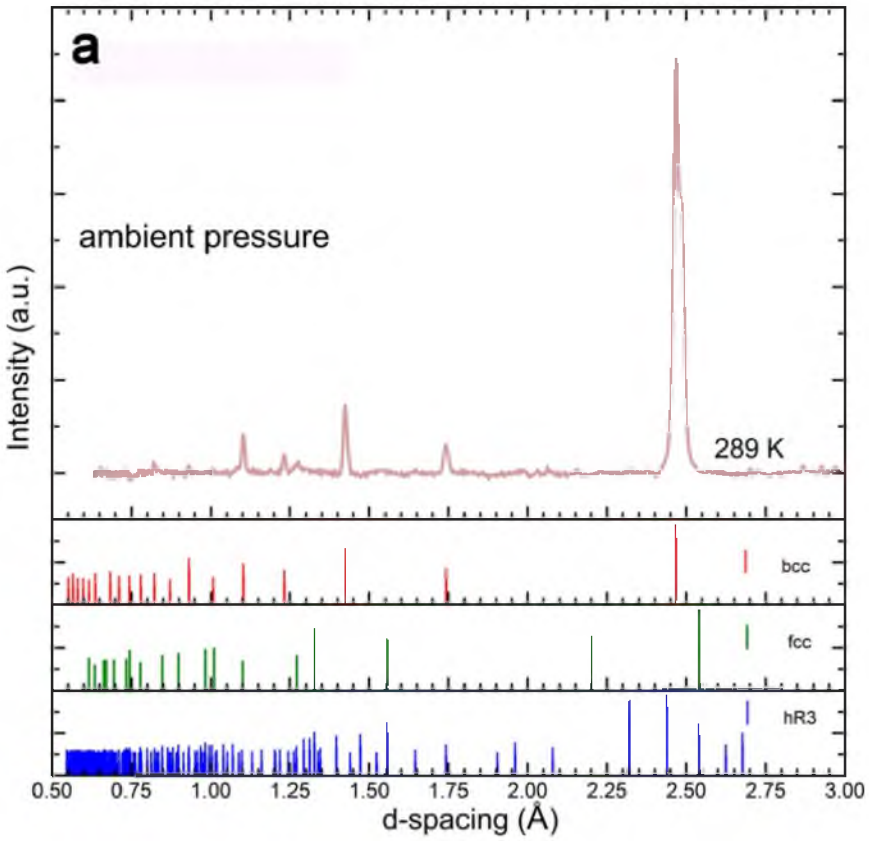

Figure A.1. The ambient pressure measurement of ^{7}Li with neutron diffraction. Clearly in the bcc phase.

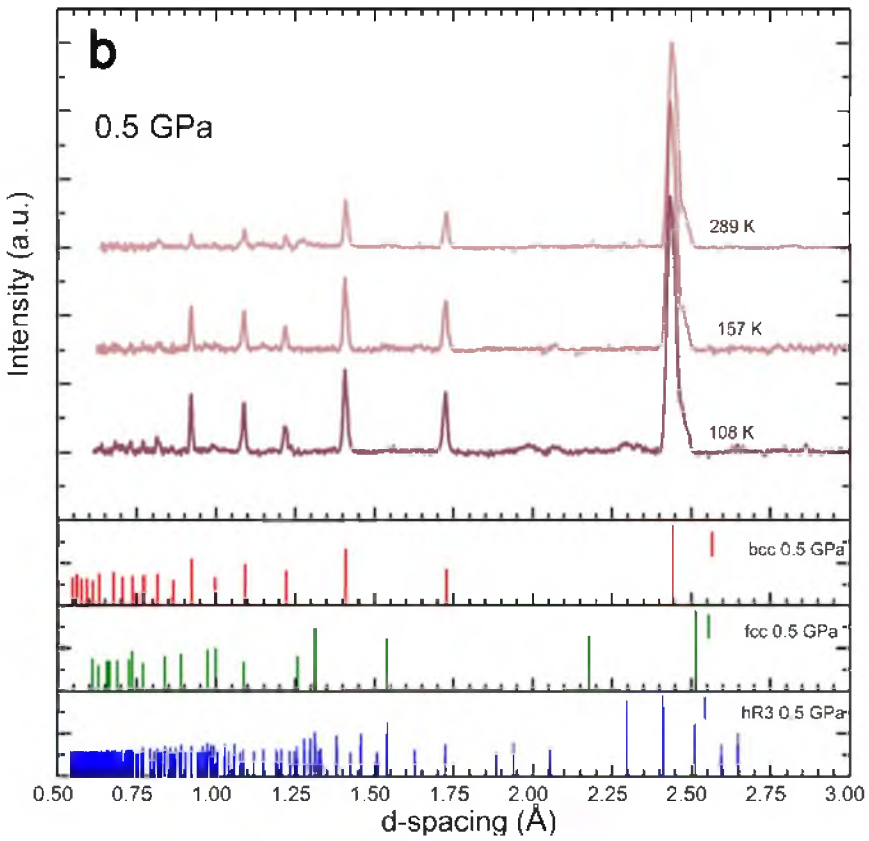

Figure A.2. ^{7}Li at $\sim$0.5 GPa. The same was not cooled sufficiently to see the transition to the hR3 phase.

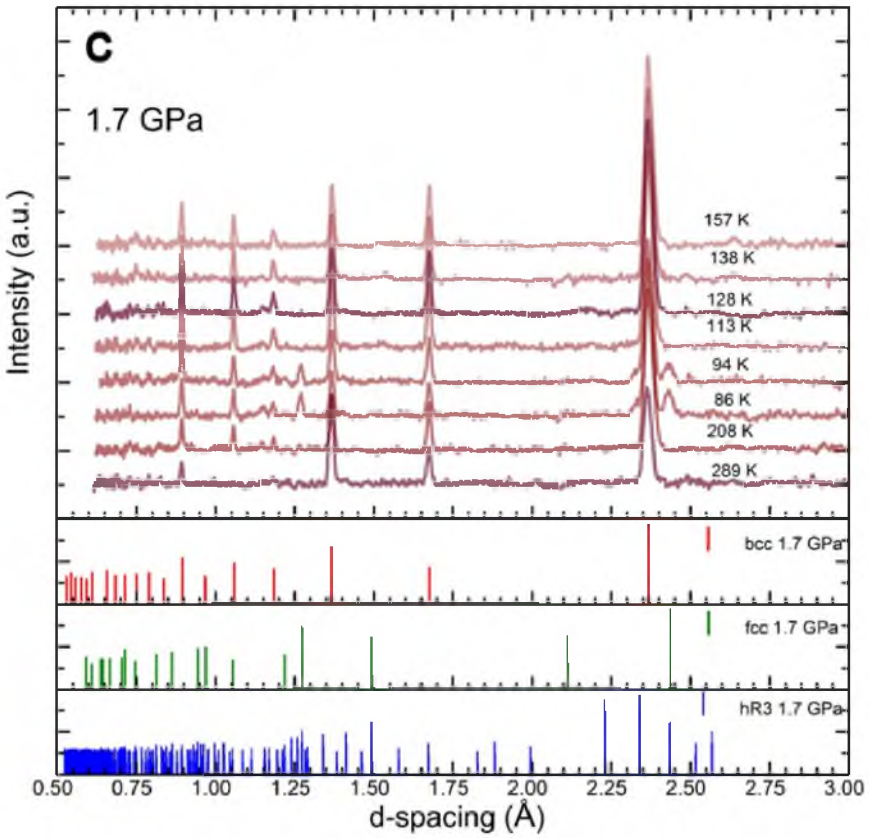

Figure A.3. ^{7}Li at $\sim$1.7 GPa. Clearly in bcc phase at high temperature and the emergence of a new phase in the measurement at $\sim$94 K can be seen. This low temperature is consistent with peaks from the hR3 phase (though that phase does have several peaks in common with the fcc phase).

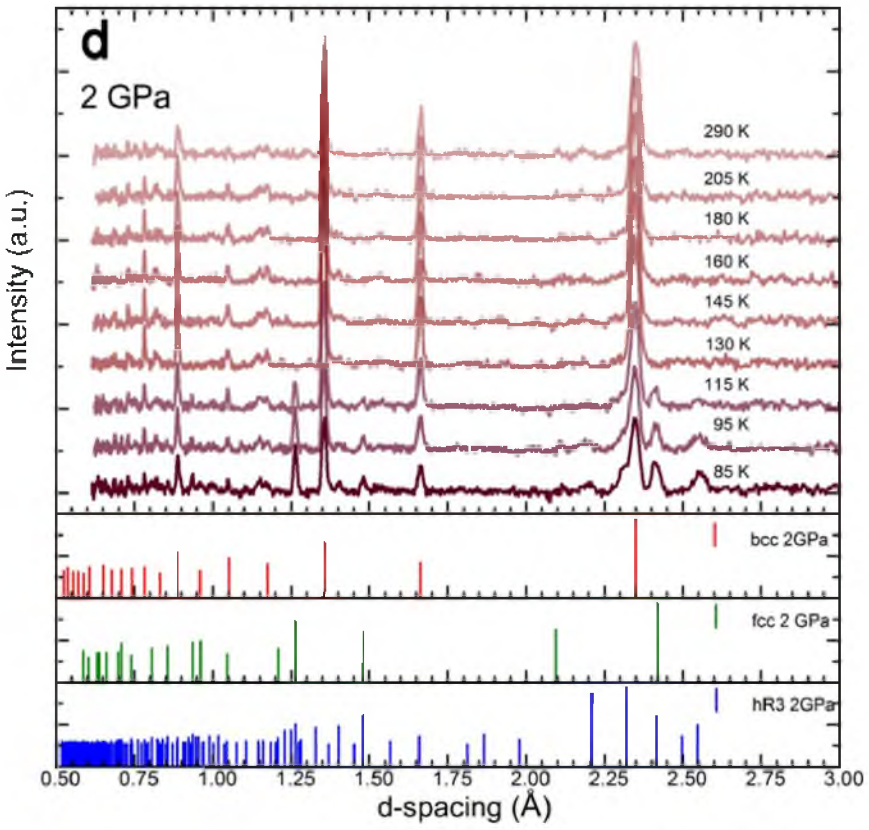

Figure A.4. ^{7}Li at $\sim$2 GPa. The evidence of the hR3 phase over the the fcc phase is much more clear at this pressure.

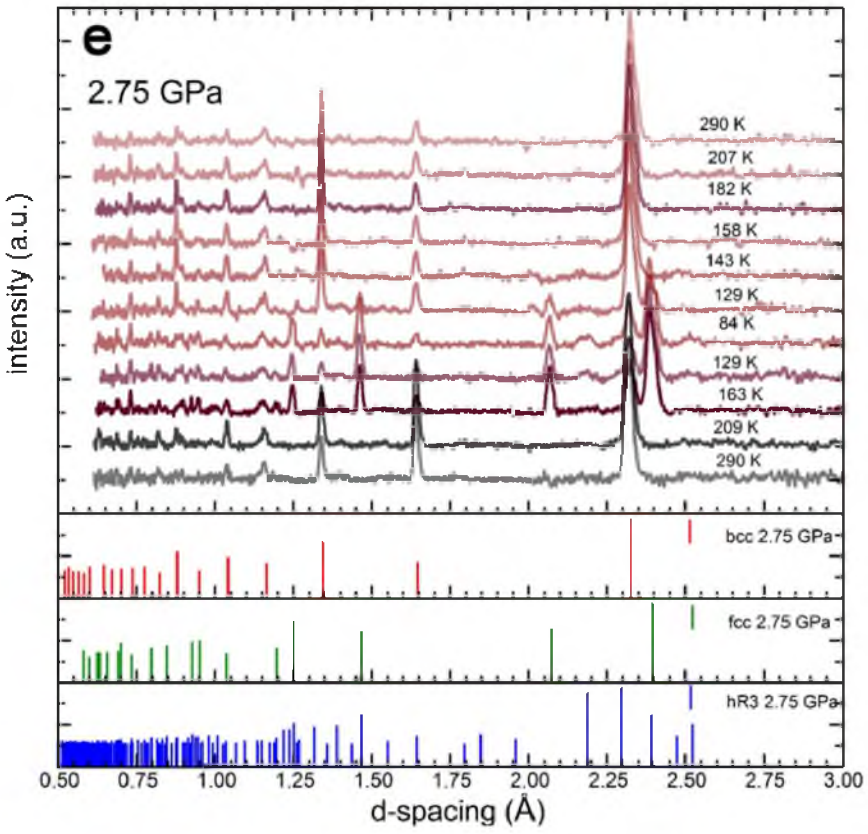

Figure A.5. ^{7}Li at $\sim$2.75 GPa. At this pressure, the hR3 phase is present at the lowest temperatures; however, upon heating, we see the loss the hR3 peaks and the strengthening of the fcc peaks up to $\sim$ 163 K, then a return to the bcc phase above 200 K.

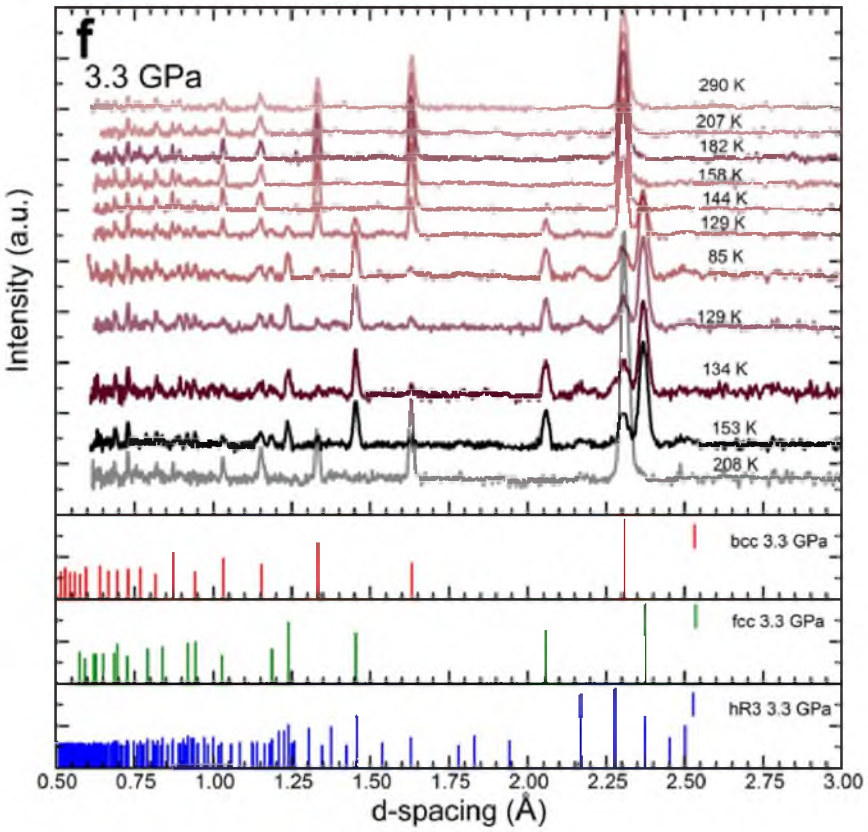

Figure A.6. ^{7}Li at $\sim$3.3 GPa. At this pressure, the hR3 phase has very little evidence. Though it is still possible, the only peaks that would be exclusively hR3 are very broad and weak, whilst the other peaks, which are shared with the fcc phase, are strong and distinct. Again, we see the strengthening of the fcc upon warming to the sample to $\sim$ 153 K but then a return to the bcc phase above 200 K.

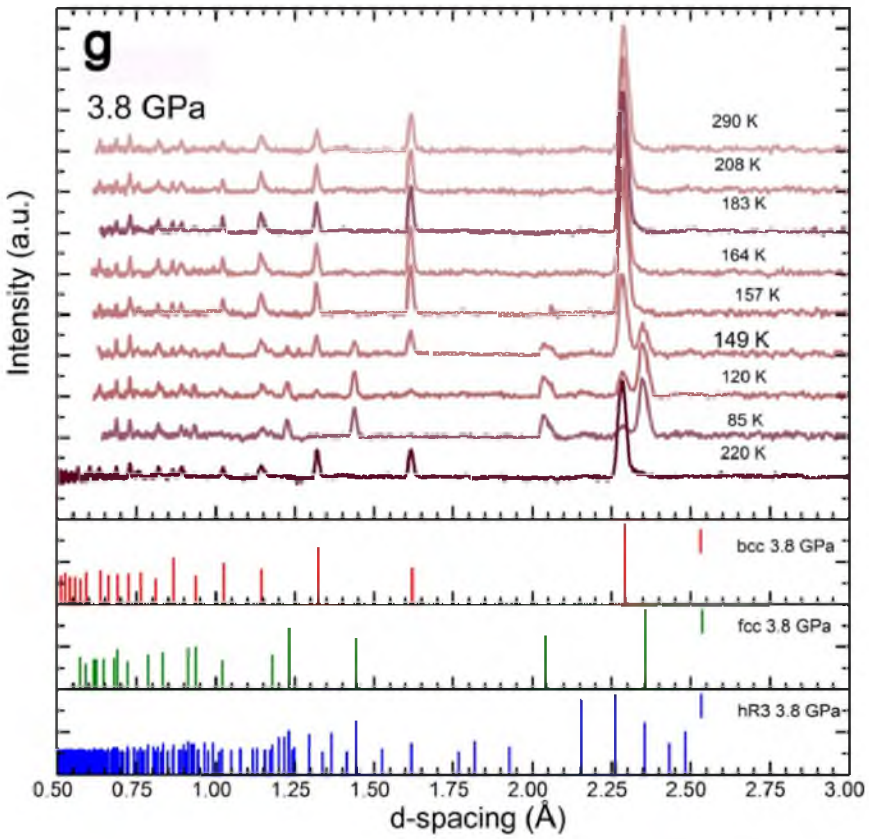

Figure A.7. ^{7}Li at $\sim$3.8 GPa. There does not appear to be any evidence for the hR3 phase at the low temperature in this pressure. At the base temperature, not only do we only see the hR3 peaks that overlap with fcc peaks, but we also see a distinct lessening of the bcc 110 peak (which would be shared with the hR3 phase). This appears to indicate that the sample is transforming into fcc phase. However, the fcc 200 peak appears somewhat broad, unlike the other peaks of the phase.

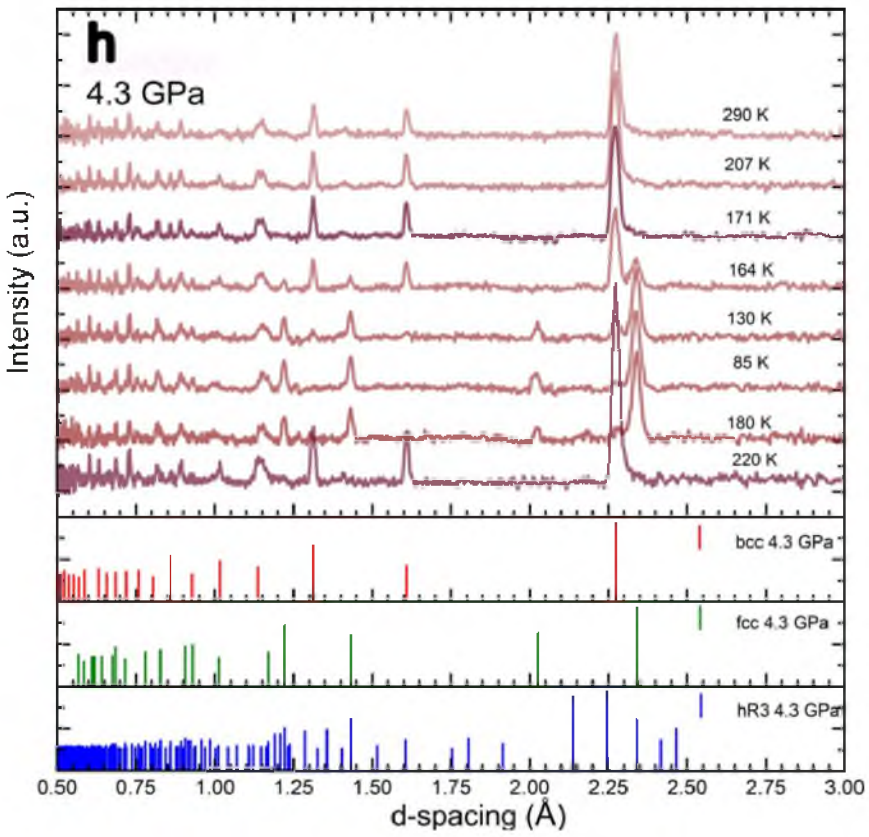

Figure A.8. ^{7}Li at $\sim$4.3 GPa. This pressure very closely resembles 3.8 GPa, including the broad fcc 200 peak. The main difference is that the fcc phase clearly comes at a higher temperature.

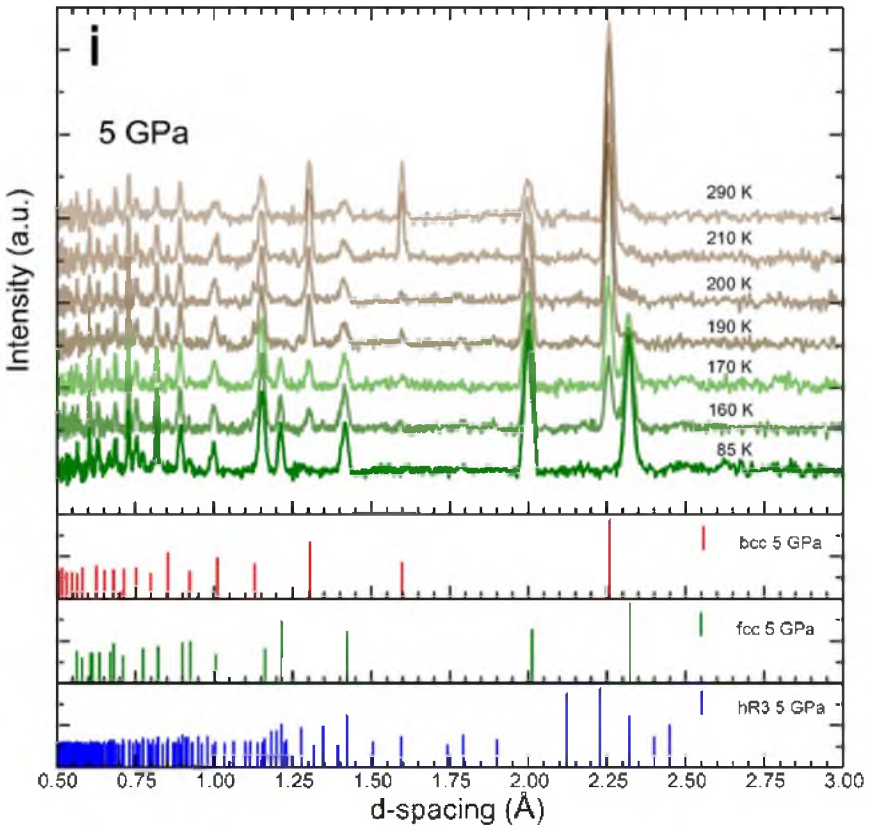

Figure A.9. ^{7}Li at $\sim$5 GPa. This pressure show some mixed fcc and bcc phase even at room temperature. Upon cooling, the fcc 200 peak becomes quite strong and distinct, becoming more prominent than the fcc 111 peak, showing that there is some texturing of the sample.

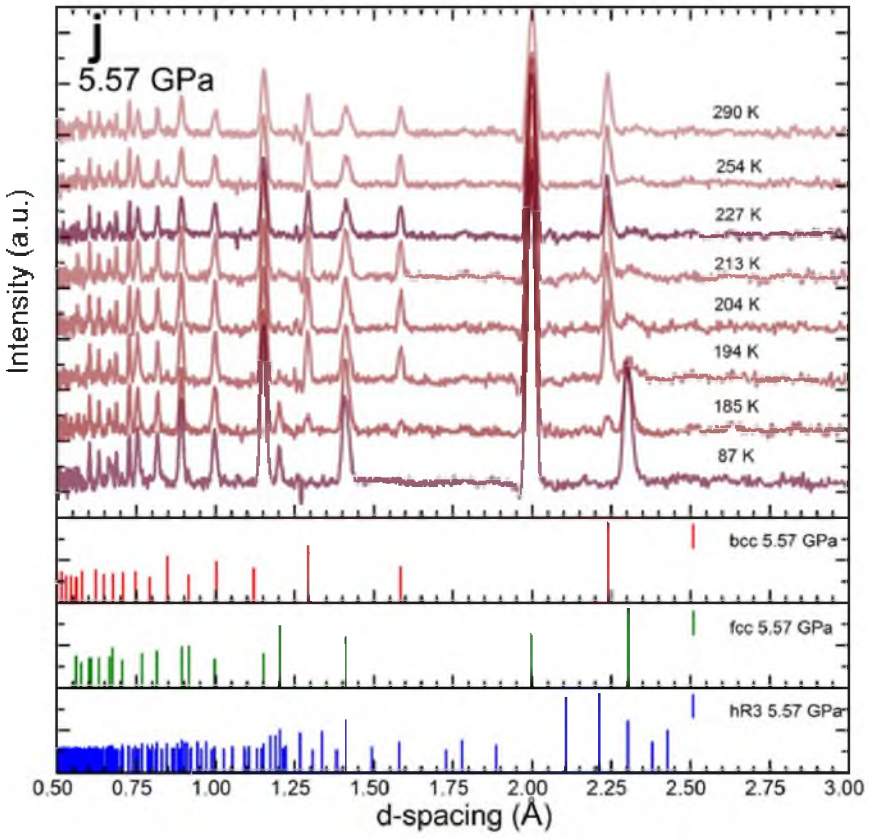

Figure A.10. ^{7}Li at $\sim 5.6\,GPa$. This pressure shows the fcc phase becoming more dominant at room temperature. The fcc 200 peak appears alongside the bcc peaks; only at low temperature ($\sim 85K$) does the fcc 111 peak begin to appear.

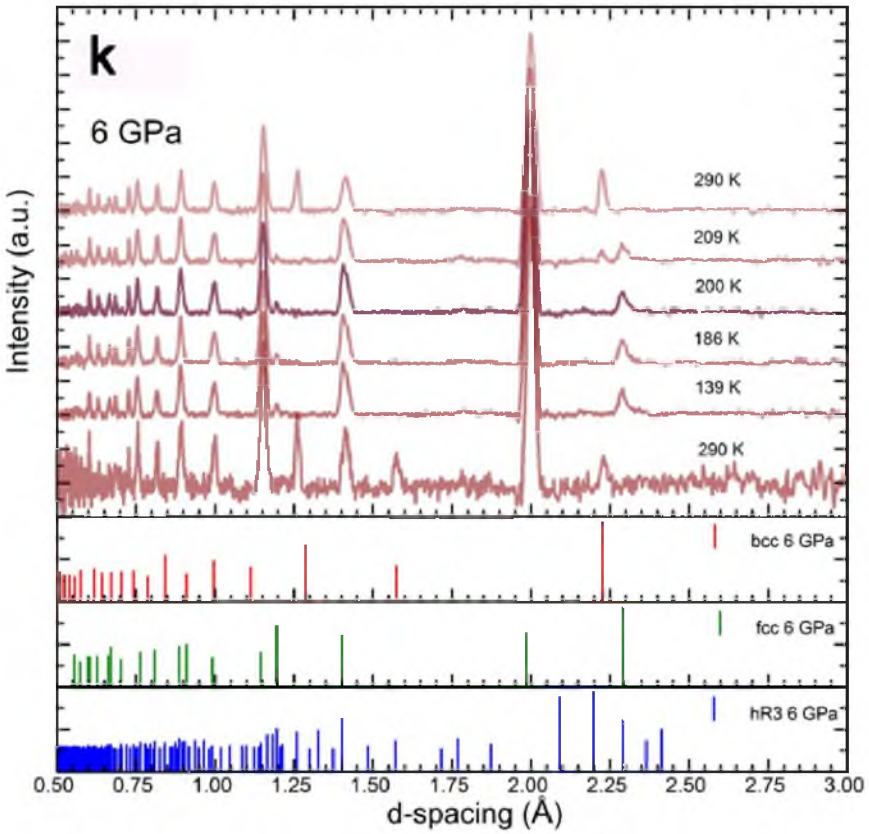

Figure A.11. ^{7}Li at $\sim 6\ GPa$. The fcc phase is dominant at room temperature; however, there are still peaks from the bcc phase, and the fcc 111 peak is conspicuously absent until the sample is cooled to $\sim 210\ K$. It appears that this peak grows only at the expense of the bcc 110 peak.

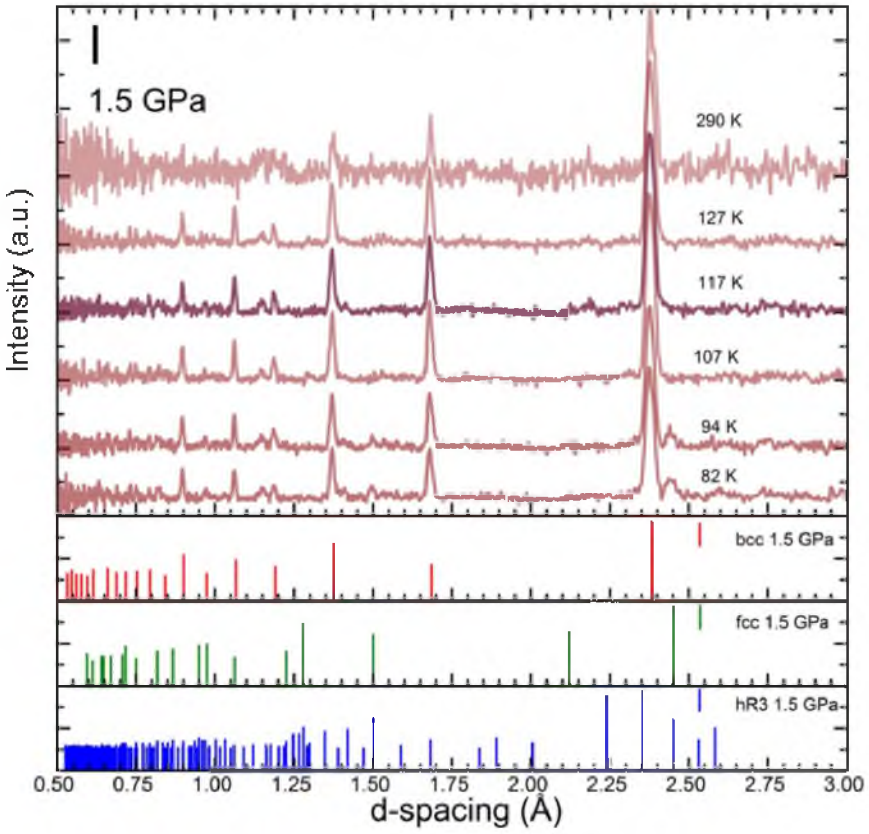

Figure A.12. ^{7}Li at 1,5 GPa. The pressure of the sample was released to look for evidence of whether the hR3 phase at lower pressure could be obtained again. We do indeed see some evidence for the hR3 below 100 K, though the exclusive hR3 are very weak.

REFERENCES

[1] Ross J Angel. Equations of state. *Reviews in Mineralogy and Geochemistry*, 41(1):35–59, 2000.

[2] Ross J Angel, Matteo Alvaro, and Javier Gonzalez-Platas. Eosfit7c and a fortran module (library) for equation of state calculations. *Zeitschrift für Kristallographie-Crystalline Materials*, 229(5):405–419, 2014.

[3] Ross J Angel, Maciej Bujak, Jing Zhao, G Diego Gatta, and Steven D Jacobsen. Effective hydrostatic limits of pressure media for high-pressure crystallographic studies. *Journal of Applied Crystallography*, 40(1):26–32, 2007.

[4] GGN Angilella, F Siringo, and R Pucci. Symmetry breaking and restoring under high pressure: the amazing behaviour of the simple alkali metals. *The European Physical Journal B-Condensed Matter and Complex Systems*, 32(3):323–327, 2003.

[5] Neil W Ashcroft. Metallic hydrogen: A high-temperature superconductor? *Physical Review Letters*, 21(26):1748, 1968.

[6] Neil W Ashcroft and N David Mermin. Solid state phys. *Saunders, Philadelphia*, page 293, 1976.

[7] NW Ashcroft. Quantum-solid behavior and the electronic structure of the light alkali metals. *Physical Review B*, 39(15):10552, 1989.

[8] NW Ashcroft. Superconductivity: Putting the squeeze on lithium. *Nature*, 419(6907):569–572, 2002.

[9] J. Bardeen, L. N. Cooper, and J. R. Schrieffer. Theory of superconductivity. *Physical Review*, 108:1175–1204, Dec 1957.

[10] Charles S Barrett. A low temperature transformation in lithium. *Physical Review*, 72(3):245, 1947.

[11] CS Barrett. X-ray study of the alkali metals at low temperatures. *Acta Crystallographica*, 9(8):671–677, 1956.

[12] Timur Bazhirov, Jesse Noffsinger, and Marvin L Cohen. Electron-phonon coupling in bcc lithium. *Physical Review B*, 84(12):125122, 2011.

[13] R Berliner, O Fajen, HG Smith, and RL Hitterman. Neutron powder-diffraction studies of lithium, sodium, and potassium metal. *Physical Review B*, 40(18):12086, 1989.

[14] R Berliner and SA Werner. Effect of stacking faults on diffraction: the structure of lithium metal. *Physical Review B*, 34(6):3586, 1986.

[15] R Boehler. Melting temperature, adiabats, and grüneisen parameter of lithium, sodium and potassium versus pressure. *Physical Review B*, 27(11):6754, 1983.

[16] R Boehler. Temperatures in the earth's core from melting-point measurements of iron at high static pressures. *Nature*, 363(6429):534–536, 1993.

[17] Reinhard Boehler and Koen De Hantsetters. New anvil designs in diamond-cells. *High Pressure Research*, 24(3):391–396, 2004.

[18] Stanimir A Bonev, Eric Schwegler, Tadashi Ogitsu, and Giulia Galli. A quantum fluid of metallic hydrogen suggested by first-principles calculations. *Nature*, 431(7009):669–672, 2004.

[19] PW Bridgman. The five alkali metals under high pressure. *Physical Review*, 27(1):68, 1926.

[20] Keith E Brister, Yogesh K Vohra, and Arthur L Ruoff. Pressure profiles at multi-megabar pressures in a diamond anvil cell using x-ray diffraction. *Review of scientific instruments*, 59(2):318–321, 1988.

[21] William D Callister and David G Rethwisch. *Fundamentals of materials science and engineering: an integrated approach*. John Wiley & Sons, 2012.

[22] Flake C Campbell. *Elements of metallurgy and engineering alloys*. ASM International, 2008.

[23] Mu Chai and J Michael Brown. Effects of static non-hydrostatic stress on the r lines of ruby single crystals. *Geophysical Research Letters*, 23(24):3539–3542, 1996.

[24] Tapan Chatterji. *Neutron scattering from magnetic materials*. Gulf Professional Publishing, 2005.

[25] B Chen, D Penwell, LR Benedetti, R Jeanloz, and MB Kruger. Particle-size effect on the compressibility of nanocrystalline alumina. *Physical Review B*, 66(14):144101, 2002.

[26] Xiao-Jia Chen, Viktor V Struzhkin, Yang Song, Alexander F Goncharov, Muhtar Ahart, Zhenxian Liu, Ho-kwang Mao, and Russell J Hemley. Pressure-induced metallization of silane. *Proceedings of the National Academy of Sciences*, 105(1):20–23, 2008.

[27] TC Chi. Electrical resistivity of alkali elements. *Journal of Physical and Chemical Reference Data*, 8(2):339–438, 1979.

[28] Akobuije D Chijioke, WJ Nellis, Alexander Soldatov, and Isaac F Silvera. The ruby pressure standard to 150gpa. *Journal of Applied Physics*, 98(11):114905, 2005.

[29] NE Christensen and DL Novikov. Predicted superconductive properties of lithium under pressure. *Physical Review Letters*, 86(9):1861, 2001.

[30] NE Christensen and DL Novikov. Calculated superconductive properties of li and na under pressure. *Physical Review B*, 73(22):224508, 2006.

[31] AF Clark, VA Deason, and RL Powell. Characterization of high purity metals by the eddy current decay method. *Cryogenics*, 12(1):35–39, 1972.

[32] R. Clausius. Ueber die bewegende kraft der wrme und die gesetze, welche sich daraus fr die wrmelehre selbst ableiten lassen. *Annalen der Physik*, 155(4):500–524, 1850.

[33] Ronald E Cohen, Oguz Gülseren, and Russell J Hemley. Accuracy of equation-of-state formulations. *American Mineralogist*, 85(2-3):338–344, 2000.

[34] Leon N Cooper. Bound electron pairs in a degenerate fermi gas. *Physical Review*, 104(4):1189, 1956.

[35] EJ Covington and DJ Montgomery. Lattice constants of separated lithium isotopes. *The Journal of Chemical Physics*, 27(5):1030–1032, 1957.

[36] Arthur P Cracknell. *The Fermi surfaces of metals*. Taylor & Francis, 1971.

[37] JM Daams, B Mitrović, and JP Carbotte. Simulation of the effects of paramagnons on a superconductor by a simple rescaling. *Physical Review Letters*, 46(1):65, 1981.

[38] WJ De Haas and PM van Alphen. The dependence of the susceptibility of diamagnetic metals upon the field. In *Proc. Netherlands Roy. Acad. Sci*, volume 33, page 170, 1930.

[39] M Debessai, T Matsuoka, JJ Hamlin, AK Gangopadhyay, JS Schilling, K Shimizu, and Y Ohishi. Superconductivity under high pressure in the binary compound cali 2. *Physical Review B*, 78(21):214517, 2008.

[40] Daniel L Decker. Equation of state of nacl and its use as a pressure gauge in high-pressure research. *Journal of Applied Physics*, 36(1):157–161, 1965.

[41] S Deemyad, E Sterer, C Barthel, S Rekhi, J Tempere, and Isaac F Silvera. Pulsed laser heating and temperature determination in a diamond anvil cell. *Review of Scientific Instruments*, 76(12):125104, 2005.

[42] Shanti Deemyad and James S Schilling. Superconducting phase diagram of li metal in nearly hydrostatic pressures up to 67 gpa. *Physical Review Letters*, 91(16):167001, 2003.

[43] Sean W Derrickson and Eric R Bittner. A self-consistent field quantum hydrodynamic approach for molecular clusters. *The Journal of Physical Chemistry A*, 110(16):5333–5341, 2006.

[44] JJ Donaghy and AT Stewart. Fermi surface of lithium by positron annihilation. *Physical Review*, 164(2):391, 1967.

[45] PI Dorogokupets and AR Oganov. Equations of state of cu and ag and revised ruby pressure scale. In *Doklady earth sciences c/c of doklady-akademiia nauk doklady*, volume 391, pages 854–857. Interperiodica Publishing, 2003.

[46] JS Dugdale, D Gugan, and K Okumura. The electrical resistivity of lithium-6. In *Proceedings of the Royal Society of London A: Mathematical, Physical and Engineering Sciences*, volume 263, pages 407–419. The Royal Society, 1961.

[47] KJ Dunn and FP Bundy. Pressure-induced superconductivity in strontium and barium. *Physical Review B*, 25(1):194, 1982.

[48] M Elliott and WR Datars. De haas-van alphen effect in sodium under pressure. *Journal of Physics F: Metal Physics*, 12(3):465, 1982.

[49] MI Eremets and IA Troyan. Conductive dense hydrogen. *Nature Materials*, 10(12):927–931, 2011.

[50] Daniel Errandonea. The melting curve of ten metals up to 12 gpa and 1600 k. *Journal of Applied Physics*, 108(3):033517, 2010.

[51] Ion Errea, Matteo Calandra, and Francesco Mauri. First-principles theory of anharmonicity and the inverse isotope effect in superconducting palladium-hydride compounds. *Physical Review Letters*, 111(17):177002, 2013.

[52] JD Fan and YM Malozovsky. Negative isotope effect in superconductivity from non-retarded repulsive interaction. *International Journal of Modern Physics B*, 17(18n20):3458–3464, 2003.

[53] Ji Feng, Richard G Hennig, NW Ashcroft, and Roald Hoffmann. Emergent reduction of electronic state dimensionality in dense ordered li-be alloys. *Nature*, 451(7177):445–448, 2008.

[54] Yejun Feng, R Jaramillo, Jiyang Wang, Yang Ren, and TF Rosenbaum. Invited article: High-pressure techniques for condensed matter physics at low temperature. *Review of Scientific Instruments*, 81(4):041301, 2010.

[55] Claudia Filippi and David M Ceperley. Path-integral monte carlo calculation of the kinetic energy of condensed lithium. *Physical Review B*, 57(1):252, 1998.

[56] Paul A Fleury. The effects of soft modes on the structure and properties of materials. *Annual Review of Materials Science*, 6(1):157–180, 1976.

[57] RD Fowler, JDG Lindsay, RW White, HH Hill, and BT Matthias. Positive isotope effect on the superconducting transition temperature of α-uranium. *Physical Review Letters*, 19(16):892, 1967.

[58] Carlos Friedli and NW Ashcroft. Aluminum under high pressure. i. equation of state. *Physical Review B*, 12(12):5552, 1975.

[59] W Friedrich, P Knipping, and MV Laue. Interference phenomena with roentgen rays. *Sitzber. Math-phys. Kl. bayer. Akad. Wiss. Manche*, 22:303, 1912.

[60] MR Gallas and GJ Piermarini. Bulk modulus and young's modulus of nanocrystalline [gamma]-alumina. *Journal of the American Ceramic Society;(United States)*, 77(11), 1994.

[61] Martin Eden Glicksman. *Principles of solidification: an introduction to modern casting and crystal growth concepts*. Springer Science & Business Media, 2010.

[62] Alexander F Goncharov, Viktor V Struzhkin, Ho-kwang Mao, and Russell J Hemley. Spectroscopic evidence for broken-symmetry transitions in dense lithium up to megabar pressures. *Physical Review B*, 71(18):184114, 2005.

[63] FA Gorelli, SF Elatresh, CL Guillaume, M Marqués, GJ Ackland, M Santoro, SA Bonev, and E Gregoryanz. Lattice dynamics of dense lithium. *Physical Review Letters*, 108(5):055501, 2012.

[64] David E Graf. *Magnetic Field-Dependent Electronic Structures of Low-Dimensional Organic Materials*. PhD thesis, 2005.

[65] Eugene Gregoryanz, Olga Degtyareva, Maddury Somayazulu, Russell J Hemley, and Ho-kwang Mao. Melting of dense sodium. *Physical Review Letters*, 94(18):185502, 2005.

[66] David Jeffrey Griffiths and Reed College. *Introduction to electrodynamics*, volume 3. prentice Hall Upper Saddle River, NJ, 1999.

[67] EL Gromnitskaya, OV Stalgorova, and SM Stishov. Equation of state and elastic properties of lithium: Isotope effects. *Journal of Experimental and Theoretical Physics Letters*, 69(1):38–43, 1999.

[68] E Grüneisen. Die abhängigkeit des elektrischen widerstandes reiner metalle von der temperatur. *Annalen der Physik*, 408(5):530–540, 1933.

[69] KA Gschneider. Solid state physics, ed. by h. *Ehrenreich, F. Seitz, D. Turnbull*, 16:275, 1964.

[70] Christophe L Guillaume, Eugene Gregoryanz, Olga Degtyareva, Malcolm I McMahon, Michael Hanfland, Shaun Evans, Malcolm Guthrie, Stanislav V Sinogeikin, and HK Mao. Cold melting and solid structures of dense lithium. *Nature Physics*, 7(3):211–214, 2011.

[71] M Guthrie, R Boehler, JJ Molaison, AM dos Santos, and CA Tulk. Powder neutron diffraction with diamond anvil cells. In *Neutron and Synchrotron Sources: Role in Crystallography - Small Angle Scattering, Supramolecular Assemblies, Emerging Characterization Facilities and Tools, and Chemical Crystallography*, 2013.

[72] Frank S Ham. Energy bands of alkali metals. ii. fermi surface. *Physical Review*, 128(6):2524, 1962.

[73] James JH Hamlin. *Superconductivity studies at extreme pressure.* PhD thesis, Washington University, 2007.

[74] M Hanfland, I Loa, K Syassen, U Schwarz, and K Takemura. Equation of state of lithium to 21gpa. *Solid State Communications*, 112(3):123–127, 1999.

[75] M Hanfland, K Syassen, NE Christensen, and DL Novikov. New high-pressure phases of lithium. *Nature*, 408(6809):174–178, 2000.

[76] Pan Hao, Yuan Fang, Jianwei Sun, Gábor I Csonka, Pier HT Philipsen, and John P Perdew. Lattice constants from semilocal density functionals with zero-point phonon correction. *Physical Review B*, 85(1):014111, 2012.

[77] RJ Hemley, CS Zha, AP Jephcoat, HK Mao, LW Finger, and DE Cox. X-ray diffraction and equation of state of solid neon to 110 gpa. *Physical Review B*, 39(16):11820, 1989.

[78] H Hemmes, A Driessen, R Griessen, and M Gupta. Isotope effects and pressure dependence of the t c of superconducting stoichiometric pdh and pdd synthesized and measured in a diamond anvil cell. *Physical Review B*, 39(7):4110, 1989.

[79] DG Hinks, H Claus, and JD Jorgensen. The complex nature of superconductivity in mgb2 as revealed by the reduced total isotope effect. *Nature*, 411(6836):457–460, 2001.

[80] James Hooper and Eva Zurek. Rubidium polyhydrides under pressure: Emergence of the linear h3- species. *Chemistry-A European Journal*, 18(16):5013–5021, 2012.

[81] John PA Ioannidis. Why most published research findings are false. *PLoS Med*, 2(8):e124, 2005.

[82] A Jayaraman, W Klement Jr, and GC Kennedy. Melting and polymorphism of barium at high pressures. *Physical Review Letters*, 10(9):387, 1963.

[83] AP Jephcoat, RJ Hemley, and HK Mao. X-ray diffraction of ruby (al 2 o 3: Cr 3+) to 175 gpa. *Physica B+ C*, 150(1):115–121, 1988.

[84] F Jona and PM Marcus. Structure of barium in three phases under pressure. *EPL (Europhysics Letters)*, 74(1):83, 2006.

[85] KI Juntunen and JT Tuoriniemi. Nuclear ordering in lithium and an upper limit on its ambient pressure superconducting transition temperature. *Physical Review Letters*, 93(15):157201, 2004.

[86] AE Karakozov and EG Maksimov. Influence of anharmonicity on superconductivity. *Zh. Eksp. Teor. Fiz*, 74:681–696, 1978.

[87] Deepa Kasinathan, J Kuneš, A Lazicki, H Rosner, CS Yoo, RT Scalettar, and WE Pickett. Superconductivity and lattice instability in compressed lithium from fermi surface hot spots. *Physical Review Letters*, 96(4):047004, 2006.

[88] MJ Kelly. Energetics of the martensitic phase transition in sodium. *Journal of Physics F: Metal Physics*, 9(10):1921, 1979.

[89] William Thomson Lord Kelvin. On the age of the sun's heat. *Macmillan's Magazine*, 5:388–393, 1862.

[90] Takemura Kenichi. High-pressure structural study of barium to 90 gpa. *Physical Review B*, 50(22):16238, 1994.

[91] Charles Kittel. *Introduction to solid state physics*. Wiley, 2005.

[92] S Klotz, JC Chervin, P Munsch, and G Le Marchand. Hydrostatic limits of 11 pressure transmitting media. *Journal of Physics D: Applied Physics*, 42(7):075413, 2009.

[93] VS Kogan. Isotope effects in the structural properties of solids. *Physics-Uspekhi*, 5(6):951–975, 1963.

[94] J Konys and HU Borgstedt. The product of the reaction of alumina with lithium metal. *Journal of Nuclear Materials*, 131(2):158–161, 1985.

[95] Vladimir Z Kresin, Andreas Bill, Stuart A Wolf, and Yu N Ovchinnikov. Unconventional isotope effects in superconductors. *Physical Review B*, 56(1):107, 1997.

[96] Maciej Krystian and Wolfgang Pichl. Metallography of alkali metal single crystals. *Materials Characterization*, 46(1):1–9, 2001.

[97] Lev Davidovich Landau and VL Ginzburg. On the theory of superconductivity. *Zh. Eksp. Teor. Fiz.*, 20:1064, 1950.

[98] A Lazicki, Russell J Hemley, WE Pickett, and Choong-Shik Yoo. Structural study of lib to 70 gpa. *Physical Review B*, 82(18):180102, 2010.

[99] A Lazicki, C-S Yoo, H Cynn, WJ Evans, WE Pickett, J Olamit, Kai Liu, and Y Ohishi. Search for superconductivity in libc at high pressure: Diamond anvil cell experiments and first-principles calculations. *Physical Review B*, 75(5):054507, 2007.

[100] Amy Lazicki, Yingwei Fei, and Russell J Hemley. High-pressure differential thermal analysis measurements of the melting curve of lithium. *Solid State Communications*, 150(13):625–627, 2010.

[101] Martin JG Lee. The de haas-van alphen effect and the fermi surface of sodium. In *Proceedings of the Royal Society of London A: Mathematical, Physical and Engineering Sciences*, volume 295, pages 440–457. The Royal Society, 1966.

[102] Martin JG Lee. Electron-ion interaction and the fermi surfaces of the alkali metals. *Physical Review*, 178(3):953, 1969.

[103] ME Levinshtein, BI Shklovskii, MS Shur, and AL Efros. The relation between the critical exponents of percolation theory. *Soviet Journal of Experimental and Theoretical Physics*, 42:197, 1976.

[104] Yinwei Li, Guoying Gao, Yu Xie, Yanming Ma, Tian Cui, and Guangtian Zou. Superconductivity at 100 k in dense sih4 (h2) 2 predicted by first principles. *Proceedings of the National Academy of Sciences*, 107(36):15708–15711, 2010.

[105] TH Lin and KJ Dunn. High-pressure and low-temperature study of electrical resistance of lithium. *Physical Review B*, 33(2):807, 1986.

[106] Frederick A Lindemann. Ueber die berechnung molekularer eigenfrequenzen. *Phys. Z*, 11:609–612, 1910.

[107] Ingo Loa, RJ Nelmes, LF Lundegaard, and MI McMahon. Extraordinarily complex crystal structure with mesoscopic patterning in barium at high pressure. *Nature Materials*, 11(7):627–632, 2012.

[108] Fritz London and Heinz London. The electromagnetic equations of the supraconductor. In *Proceedings of the Royal Society of London A: Mathematical, Physical and Engineering Sciences*, volume 149, pages 71–88. The Royal Society, 1935.

[109] Paul Loubeyre, Florent Occelli, and René LeToullec. Optical studies of solid hydrogen to 320 gpa and evidence for black hydrogen. *Nature*, 416(6881):613–617, 2002.

[110] HD Luedemann and GC Kennedy. Melting curves of lithium, sodium, potassium, and rubidium to 80 kilobars. *Journal of Geophysical Research*, 73(8):2795–2805, 1968.

[111] Yanming Ma, Mikhail Eremets, Artem R Oganov, Yu Xie, Ivan Trojan, Sergey Medvedev, Andriy O Lyakhov, Mario Valle, and Vitali Prakapenka. Transparent dense sodium. *Nature*, 458(7235):182–185, 2009.

[112] Ch Maier, O Blaschko, and W Pichl. Influence of uniaxial deformation on the phase transformation in lithium. *Physical Review B*, 52(13):9283, 1995.

[113] HK Mao, RJ Hemley, Y Wu, AP Jephcoat, LW Finger, CS Zha, and WA Bassett. High-pressure phase diagram and equation of state of solid helium from single-crystal x-ray diffraction to 23.3 gpa. *Physical Review Letters*, 60(25):2649, 1988.

[114] HK Mao, J Xu, and PM Bell. Calibration of the ruby pressure gauge to 800 kbar under quasi-hydrostatic conditions. *J. Geophys. Res*, 91(B5):4673–4676, 1986.

[115] Ho-kwang Mao and Russell J Hemley. Ultrahigh-pressure transitions in solid hydrogen. *Reviews of Modern Physics*, 66(2):671, 1994.

[116] Ho-Kwong Mao and Peter M Bell. High-pressure physics: the 1-megabar mark on the ruby r1 static pressure scale. *Science*, 191(4229):851–852, 1976.

[117] M Marqués, MI McMahon, E Gregoryanz, M Hanfland, CL Guillaume, CJ Pickard, GJ Ackland, and RJ Nelmes. Crystal structures of dense lithium: a metal-semiconductor-metal transition. *Physical Review Letters*, 106(9):095502, 2011.

[118] T Matsuoka, M Sakata, Y Nakamoto, K Takahama, K Ichimaru, K Mukai, K Ohta, N Hirao, Y Ohishi, and K Shimizu. Pressure-induced reentrant metallic phase in lithium. *Physical Review B*, 89(14):144103, 2014.

[119] Takahiro Matsuoka and Katsuya Shimizu. Direct observation of a pressure-induced metal-to-semiconductor transition in lithium. *Nature*, 458(7235):186–189, 2009.

[120] Augustus Matthiessen and C Vogt. Ueber den einfluss der temperatur auf die elektrische leitungsfähigkeit der legirungen. *Annalen der Physik*, 198(5):19–78, 1864.

[121] WL McMillan. Transition temperature of strong-coupled superconductors. *Physical Review*, 167(2):331, 1968.

[122] Andrew W McReynolds. Effects of stress and deformation on the martensite transformation. *Journal of Applied Physics*, 20(10):896–907, 1949.

[123] Charles Meade and Raymond Jeanloz. Yield strength of al 2 o 3 at high pressures. *Physical Review B*, 42(4):2532, 1990.

[124] Walther Meissner and Robert Ochsenfeld. Ein neuer effekt bei eintritt der supraleitfähigkeit. *Naturwissenschaften*, 21(44):787–788, 1933.

[125] AR Moodenbaugh and J Wittig. Superconductivity in the high-pressure phases of barium. *Journal of Low Temperature Physics*, 10(1-2):203–206, 1973.

[126] NF Mott. The resistance of liquid metals. *Proceedings of the Royal Society of London. Series A, Containing Papers of a Mathematical and Physical Character*, pages 465–472, 1934.

[127] Jun Nagamatsu, Norimasa Nakagawa, Takahiro Muranaka, Yuji Zenitani, and Jun Akimitsu. Superconductivity at 39 k in magnesium diboride. *Nature*, 410(6824):63–64, 2001.

[128] Akira Nagasawa. Martensitic transition and related properties in agcd alloy. *Journal of the Physical Society of Japan*, 35(2):489–494, 1973.

[129] Chandrabhas Narayana, Huan Luo, Jon Orloff, and Arthur L Ruoff. Solid hydrogen at 342 gpa: no evidence for an alkali metal. *Nature*, 393(6680):46–49, 1998.

[130] O Narygina, EE McBride, GW Stinton, and MI McMahon. Melting curve of potassium to 22 gpa. *Physical Review B*, 84(5):054111, 2011.

[131] Harry C Nash and Charles S Smith. Single-crystal elastic constants of lithium. *Journal of Physics and Chemistry of Solids*, 9(2):113–118, 1959.

[132] JB Neaton and NW Ashcroft. Pairing in dense lithium. *Nature*, 400(6740):141–144, 1999.

[133] RJ Nelmes, DR Allan, MI McMahon, and SA Belmonte. Self-hosting incommensurate structure of barium iv. *Physical Review Letters*, 83(20):4081, 1999.

[134] L Oberli, AA Manuel, R Sachot, P Descouts, and M Peter. Fermi surface of lithium studied by positron annihilation. *Physical Review B*, 31(9):6104, 1985.

[135] Bart Olinger and JW Shaner. Lithium, compression and high-pressure structure. *Science*, 219(4588):1071–1072, 1983.

[136] H Kamerlingh Onnes. The superconductivity of mercury. *Comm. Phys. Lab. Univ. Leiden*, 122:124, 1911.

[137] AW Overhauser. Crystal structure of lithium at 4.2 k. *Physical Review Letters*, 53(1):64, 1984.

[138] Satya Pal. Transport properties of noble metals. *Journal of Physics F: Metal Physics*, 3(7):1296, 1973.

[139] Vitalij K Pecharsky and Peter Y Zavalij. *Fundamentals of powder diffraction and structural characterization of materials*, volume 69. Springer, 2009.

[140] W Pichl and M Krystian. Martensitic transformation and mechanical deformation of high-purity lithium. *Materials Science and Engineering: A*, 273:208–212, 1999.

[141] GJ Piermarini, S Block, and JD Barnett. Hydrostatic limits in liquids and solids to 100 kbar. *Journal of Applied Physics*, 44(12):5377–5382, 1973.

[142] RW Powell, RP Tye, and Margaret J Woodman. Thermal conductivities and electrical resistivities of the platinum metals. *Platinum Metals Review*, 6(4):138–143, 1962.

[143] C Probst and J Wittig. Superconductivity: metals, alloys and compounds. *Handbook on the Physics and Chemistry of Rare Earths*, 1:749–795, 1978.

[144] DL Randles and M Springford. Observation of de haas-van alphen oscillations in a lithium dispersion. *Journal of Physics F: Metal Physics*, 3(10):L185, 1973.

[145] DL Randles and M Springford. De haas-van alphen effect in alkali metal dispersions and the fermi surface of lithium. *Journal of Physics F: Metal Physics*, 6(10):1827, 1976.

[146] Jean-Yves Raty, Eric Schwegler, and Stanimir A Bonev. Electronic and structural transitions in dense liquid sodium. *Nature*, 449(7161):448–451, 2007.

[147] CF Richardson and NW Ashcroft. Effective electron-electron interactions and the theory of superconductivity. *Physical Review B*, 55(22):15130, 1997.

[148] AM Rosenfeld and MJ Stott. Change in resistivity of simple metals on melting. *Physical Review B*, 42(6):3406, 1990.

[149] Muhammad Sahimi. Finite-size scaling calculation of conductivity of three-dimensional conductor-superconductor networks at percolation threshold. *Journal of Physics C: Solid State Physics*, 17(13):L355, 1984.

[150] Masafumi Sakata, Yuki Nakamoto, Katsuya Shimizu, Takahiro Matsuoka, and Yasuo Ohishi. Superconducting state of ca-vii below a critical temperature of 29 k at a pressure of 216 gpa. *Physical Review B*, 83(22):220512, 2011.

[151] Anne Marie Schaeffer, Weizhao Cai, Ella Olejnik, Jamie J Molaison, Stanislav Sinogeikin, Antonio M dos Santos, and Shanti Deemyad. Boundaries for martensitic transition of 7li under pressure. *Nature Communications*, 6, 2015.

[152] Anne Marie Schaeffer, Scott R Temple, Jasmine K Bishop, and Shanti Deemyad. High-pressure superconducting phase diagram of 6li: Isotope effects in dense lithium. *Proceedings of the National Academy of Sciences*, 112(1):60–64, 2015.

[153] Anne Marie J Schaeffer and Shanti Deemyad. Twin sample chamber for simultaneous comparative transport measurements in a diamond anvil cell. *Review of Scientific Instruments*, 84(9):095108, 2013.

[154] Anne Marie J Schaeffer, Matthew C DeLong, Zachary W Anderson, William B Talmadge, Sivaraman Guruswamy, and Shanti Deemyad. Superconductivity of bali4 under pressure. *Journal of Physics: Condensed Matter*, 25(37):375701, 2013.

[155] Anne Marie J. Schaeffer, William B. Talmadge, Scott R. Temple, and Shanti Deemyad. High pressure melting of lithium. *Physical Review Letters*, 109:185702, Nov 2012.

[156] T Schenk, D Holland-Moritz, V Simonet, R Bellissent, and DM Herlach. Icosahedral short-range order in deeply undercooled metallic melts. *Physical Review Letters*, 89(7):075507, 2002.

[157] Vadim Vasil'evich Schmidt, Paul Müller, and Alexey V Ustinov. *The Physics of Superconductors: Introduction to Fundamentals and Applications*. Springer Science & Business Media, 1997.

[158] W Schwarz and O Blaschko. Polytype structures of lithium at low temperatures. *Physical Review Letters*, 65(25):3144, 1990.

[159] Dieter Schwarzenbach. *Crystallography*. Wiley, 1996.

[160] Katsuya Shimizu, Hiroto Ishikawa, Daigoroh Takao, Takehiko Yagi, and Kiichi Amaya. Superconductivity in compressed lithium at 20 k. *Nature*, 419(6907):597–599, 2002.

[161] David Shoenberg. *Magnetic oscillations in metals*. Cambridge University Press, 1984.

[162] Balmukund Shukla, NV Chandra Shekar, NR Sanjay Kumar, TR Ravindran, P Sahoo, S Dhara, and P Ch Sahu. Twin chamber sample assembly in dac and hpht studies on gan nano-particles. In *Journal of Physics: Conference Series*, volume 377, page 012014. IOP Publishing, 2012.

[163] T Skoskiewicz, AW Szafranski, W Bujnowski, and B Baranowski. Isotope effect in the superconducting palladium-hydrogen-deuterium system. *Journal of Physics C: Solid State Physics*, 7(15):2670, 1974.

[164] V Smetana, V Babizhetskyy, C Hoch, and A Simon. Refinement of the crystal structure of barium tetralithium, bali4. *Zeitschrift für Kristallographie-New Crystal Structures*, 221(1-4):434–434, 2006.

[165] Volodymyr Smetana, Volodymyr Babizhetskyy, Grigori V Vajenine, Constantin Hoch, and Arndt Simon. Double-icosahedral li clusters in a new binary compound ba19li44: A reinvestigation of the ba-li phase diagram. *Inorganic Chemistry*, 46(13):5425–5428, 2007.

[166] HG Smith. Martensitic phase transformation of single-crystal lithium from bcc to a 9r-related structure. *Physical Review Letters*, 58(12):1228, 1987.

[167] HG Smith, R Berliner, JD Jorgensen, M Nielsen, and J Trivisonno. Pressure effects on the martensitic transformation in metallic lithium. *Physical Review B*, 41(2):1231, 1990.

[168] FD Stacey and RD Irvine. Theory of melting: thermodynamic basis of lindemann's law. *Australian Journal of Physics*, 30(6):631–640, 1977.

[169] Sergei Mikhailovich Stishov. Melting at high pressures. *Physics-Uspekhi*, 11(6):816–830, 1969.

[170] Sergei Mikhailovich Stishov. Quantum effects in condensed matter at high pressure. *Physics-Uspekhi*, 44(3):285–290, 2001.

[171] D Stroud and NW Ashcroft. Theory of the melting of simple metals: Application to na. *Physical Review B*, 5(2):371, 1972.

[172] Viktor V Struzhkin, Mikhail I Eremets, Wei Gan, Ho-kwang Mao, and Russell J Hemley. Superconductivity in dense lithium. *Science*, 298(5596):1213–1215, 2002.

[173] Isaac Tamblyn, Jean-Yves Raty, and Stanimir A Bonev. Tetrahedral clustering in molten lithium under pressure. *Physical Review Letters*, 101(7):075703, 2008.

[174] SH Taole, HR Glyde, and Roger Taylor. Anharmonic properties of li. *Physical Review B*, 18(6):2643, 1978.

[175] EE Tareyeva and TI Trapezina. Isotope effect in superconductors under pressure. *Physics Letters A*, 37(1):83–84, 1971.

[176] William Thomson. Xv.on the secular cooling of the earth. *Transactions of the Royal Society of Edinburgh*, 23(01):157–169, 1862.

[177] Juha Tuoriniemi, Kirsi Juntunen-Nurmilaukas, Johanna Uusvuori, Elias Pentti, Anssi Salmela, and Alexander Sebedash. Superconductivity in lithium below 0.4 millikelvin at ambient pressure. *Nature*, 447(7141):187–189, 2007.

[178] D Turnbull. Formation of crystal nuclei in liquid metals. *Journal of Applied Physics*, 21(10):1022–1028, 1950.

[179] AR Ubbelohde. Zero point energy in the determination of the structure of solids. *Transactions of the Faraday Society*, 32:525–529, 1936.

[180] VG Vaks, MI Katsnelson, VG Koreshkov, AI Likhtenstein, OE Parfenov, VF Skok, VA Sukhoparov, AV Trefilov, and AA Chernyshov. An experimental and theoretical study of martensitic phase transitions in li and na under pressure. *Journal of Physics: Condensed Matter*, 1(32):5319, 1989.

[181] Pascal Vinet, James H Rose, John Ferrante, and John R Smith. Universal features of the equation of state of solids. *Journal of Physics: Condensed Matter*, 1(11):1941, 1989.

[182] Yogesh K Vohra, Steven J Duclos, and Arthur L Ruoff. High-pressure x-ray diffraction studies on rhenium up to 216 gpa (2.16 mbar). *Physical Review B*, 36(18):9790, 1987.

[183] FREDERICK E Wang, FA Kanda, CF Miskell, and AJ King. The crystal structures of sr6mg23, srmg4, ba6mg23 and bali4. *Acta Crystallographica*, 18(1):24–31, 1965.

[184] Hui Wang, S Tse John, Kaori Tanaka, Toshiaki Iitaka, and Yanming Ma. Superconductive sodalite-like clathrate calcium hydride at high pressures. *Proceedings of the National Academy of Sciences*, 109(17):6463–6466, 2012.

[185] YR Wang and AW Overhauser. Lattice dynamics of lithium at low temperature. *Physical Review B*, 34(12):8401, 1986.

[186] Bertram Eugene Warren. *X-ray Diffraction*. Courier Corporation, 1969.

[187] ST Weir, DD Jackson, S Falabella, G Samudrala, and YK Vohra. An electrical microheater technique for high-pressure and high-temperature diamond anvil cell experiments. *Review of Scientific Instruments*, 80(1):013905, 2009.

[188] ST Weir, MJ Lipp, S Falabella, G Samudrala, and YK Vohra. High pressure melting curve of tin measured using an internal resistive heating technique to 45 gpa. *Journal of Applied Physics*, 111(12):123529, 2012.

[189] ST Weir, AC Mitchell, and WJ Nellis. Metallization of fluid molecular hydrogen at 140 gpa (1.4 mbar). *Physical Review Letters*, 76(11):1860, 1996.

[190] E Wigner and H áB Huntington. On the possibility of a metallic modification of hydrogen. *The Journal of Chemical Physics*, 3(12):764–770, 1935.

[191] Rinke J Wijngaarden, D Tristan Jover, and R Griessen. Intrinsic and carrier density effects on the pressure dependence of t c of high-temperature superconductors. *Physica B: Condensed Matter*, 265(1):128–135, 1999.

[192] S Wilke. Bond percolation threshold in the simple cubic lattice. *Physics Letters A*, 96(7):344–346, 1983.

[193] J Wittig and BT Matthias. Superconductivity of barium under pressure. *Physical Review Letters*, 22(13):634, 1969.

[194] JA Woollam and CW Chu. *High-pressure and Low-temperature Physics*. Springer Science & Business Media, 2012.

[195] Hitoshi Yamaoka, Yumiko Zekko, Ignace Jarrige, Jung-Fu Lin, Nozomu Hiraoka, Hirofumi Ishii, Ku-Ding Tsuei, and Jun'ichiro Mizuki. Ruby pressure scale in a low-temperature diamond anvil cell. *Journal of Applied Physics*, 112(12):124503, 2012.

[196] Yansun Yao, JS Tse, K Tanaka, F Marsiglio, and Y Ma. Superconductivity in lithium under high pressure investigated with density functional and eliashberg theory. *Physical Review B*, 79(5):054524, 2009.

[197] David A Young, AK McMahan, and Marvin Ross. Equation of state and melting curve of helium to very high pressure. *Physical Review B*, 24(9):5119, 1981.

[198] Eva Zurek, Roald Hoffmann, NW Ashcroft, Artem R Oganov, and Andriy O Lyakhov. A little bit of lithium does a lot for hydrogen. *Proceedings of the National Academy of Sciences*, 106(42):17640–17643, 2009.